5-2021

The Controlled Synthesis of Hydrogen Electrocatalysts for Alkaline Exchange Membrane Fuel Cell and Electrolysis Applications via Chemical Vapor Deposition

Stefan Thurston Dubard Williams
swill178@vols.utk.edu

To the Graduate Council:

I am submitting herewith a dissertation written by Stefan Thurston Dubard Williams entitled "The Controlled Synthesis of Hydrogen Electrocatalysts for Alkaline Exchange Membrane Fuel Cell and Electrolysis Applications via Chemical Vapor Deposition." I have examined the final electronic copy of this dissertation for form and content and recommend that it be accepted in partial fulfillment of the requirements for the degree of Doctor of Philosophy, with a major in Chemical Engineering.

Thomas Zawodzinski, Major Professor

We have read this dissertation and recommend its acceptance:

Bamin Khomami, Gila Stein, Gerd Duscher

Accepted for the Council:

Dixie L. Thompson

Vice Provost and Dean of the Graduate School

(Original signatures are on file with official student records.)

The Controlled Synthesis of Hydrogen Electrocatalysts for Alkaline Exchange Membrane Fuel Cell and Electrolysis Applications via Chemical Vapor Deposition

A Dissertation Presented for the
Doctor of Philosophy
Degree
The University of Tennessee, Knoxville

Stefan Thurston DuBard Williams
May 2021

DEDICATION

I dedicate my work to my grandparents, Grandma, Papa, Big Mama, and Big Daddy, who have always been with me in spirit, although they are no longer with me in the flesh.

ACKNOWLEDGEMENTS

I would be remiss if I did not start by thanking Dr. Thomas Zawodzinski for the fantastic opportunity to work under his advisement and his flexibility regarding my unique matriculation. I want to thank my mentor at Los Alamos National Laboratory (LANL), Mr. Tommy Rockward, and Senior Researchers at UT-Knoxville, Dr. Gabriel Goenaga and Dr. Ramez Elgammal, for their constant motivation, support, and genuine friendship. The standard these men have set for themselves and me has developed me into the young researcher I am today. I want to thank my committee members, Dr. Bamin Khomami, Dr. Gila Stein, and Dr. Gerd Duscher, for their feedback and guidance regarding ways to enhance my research perspective. A special thank you goes to the staff and friends I have interacted with at LANL, namely, Dr. Andre Spears and Dr. Ulises Martinez, who have been rocks for me to lean on regarding both life and research. Thank you also to Dr. Mahlon Wilson, the principal motivator for me to pursue an advanced degree. A special shoutout goes to the soldiers and leaders of the 278th Armored Cavalry Regiment, Knoxville, TN, who have been entirely supportive and flexible with me over the last four years. Most of all, I would like to thank my mother and father, Francine and Maurice Williams; my sister, Lora'el, and my lovely girlfriend Janine Ray, who have been my cheerleaders from the onset of my decision to pursue an advanced degree.

I thank the Los Alamos National Laboratory's African American Partnership Program (AAPP), supported by the National Nuclear Security Agencies (NNSA)

Minority Serving Institute Partnership Program (MSIPP), for its financial support. This work was performed, in part, at the Center for Integrated Nanotechnologies, an Office of Science User Facility operated for the U.S. Department of Energy (DOE) Office of Science. Los Alamos National Laboratory, an affirmative action equal opportunity employer, is managed by Triad National Security, LLC for the U.S. Department of Energy's NNSA, under contract 89233218CNA000001. I thank Dr. Angelica Benavidez for microscopy done at The University of New Mexico's Center for Micro-Engineered Materials (CMEM). Additionally, I thank Dr. Troy Semelsberger for his assistance in collecting materials characterization data.

ABSTRACT

The development of catalysts for the electrochemical processes of hydrogen systems (e.g., fuel cells and electrolyzer systems) continues to be an attractive area of research for renewable energy technologies. One significant challenge has been developing hydrogen catalysts suitable for alkaline environments, mainly due to the sluggish kinetics of hydrogen reactions. In alkaline environments, the kinetics are decreased by two orders of magnitude when compared to acidic environments. Chemical vapor deposition (CVD) is a conventional method used to synthesize these types of catalysts. This effort discusses extending work being done using a modified CVD process known as “Poor Man’s” CVD (PMCVD) to tailor catalyst properties and inherently further its impact in electrochemical catalyst application. PMCVD utilizes an inexpensive vacuum oven to sublime commercially available and easily synthesized metal-organic salt precursors, lowering synthesis cost while providing better control of the catalyst properties such as particle size and distribution.

Herein, we describe the various efforts conducted to characterize electrocatalysts produced via the PMCVD process to further elucidate this modified CVD methods versatility and control. Additionally, we utilize a myriad of electrochemical characterization techniques to measure the electrocatalytic activates of catalyst prepared using this modified CVD method for the hydrogen oxidation reaction (HOR) and hydrogen evolution reaction (HER) in alkaline media through half-cell reactions. The study begins with the development of rate laws

and deposition mechanism for the PMCVD process facilitated by measuring particle growth as a function of metal loading. We investigate the impact varying reaction conditions have on the crystal structure of the deposited nanoparticles. We determine the PMCVD's efficiency in alloying identical and mixed crystal structured metals through the development of bifunctional catalysts for the HOR/HER. We studied the impact varying properties of carbon supports has on the deposition method as well as how these properties impact the hydrogen kinetics. We close this work by investigating the deposition of transition metals and begin the necessary steps to elucidating the impact the addition of water has on the deposition mechanism. These results provide a clear description regarding the tuning of both physical and catalytic properties of nanoparticles produced through this deposition method.

TABLE OF CONTENTS

LIST OF TABLES

LIST OF FIGURES

CHAPTER I
INTRODUCTION

Proton Exchange Fuel Cells

There is a growing need for alternative energy storage and conversion devices as nonrenewable resources continue to be depleted. Currently, the United States receives much of its energy from fossil fuels, with a slight increase in the use of renewable energy sources in the last few decades[1]. One central system in the renewable energy field is the fuel cell. Fuel cells have proven to be a viable option for power conversion due to their high efficiencies, power densities, and scalability[2]. A fuel cell is an electrochemical device that converts chemical energy into electrical energy via a galvanic process. In general, fuel cells are named by the electrolyte that acts as a separator between the anode and cathode.

The most common fuel cell device researched are Polymer Electrolyte Membrane Fuel Cells (PEMFCs). These devices are primarily used for automotive and stationary/ backup power sources[3-8]. PEMFCs operate at low temperatures, approximately 60-80^{o}C. In a PEMFC, the separator or membrane allows water and protons to cross while separating the reactants from one another. Moreover, the electrons that are produced through the electrochemical reactions are passed through an external circuit creating a current able to do work.

When operated in reverse, a fuel cell becomes an electrolyzer. A primary use for electrolyzers is in hydrogen production via water splitting, e.g., electrolysis[9-12]. The electrolyzer reaction products are pure H_2 and O_2. Therefor if powered by renewable electricity, these devices can be an eco-friendly alternative to other hydrogen reforming processes that generate greenhouse gasses such as methane and hydrocarbon reforming[11,13].

On the anode of PEMFCs, H_2 is oxidized, producing protons and electrons through the Hydrogen Oxidation Reaction (HOR), equation 1.

$$H_2 \longrightarrow 2H^+ + 2e^- \qquad (1)$$

The resulting protons pass through the polymer electrolyte membrane, and the electrons are sent through an external circuit. The protons and electrons are then used as reactants for the Oxygen Reduction Reaction (ORR) on the cathode described through equation 2. Equation 3 is the overall cell reaction for a PEMFC.

$$\frac{1}{2}O_2 + 2H^+ + 2e^- \longrightarrow H_2O \qquad (2)$$

$$H_2 + \frac{1}{2}O_2 \longrightarrow H_2O \qquad (3)$$

Cost, performance, and durability are the leading limitations to FC devices' commercialization [14,15]. The hydrogen reaction is facile in these devices when catalyzed by precious group metals (PGM). However, even under optimal conditions, the oxygen reaction is sluggish, leading to Equation 2 governing most of the FC's performance making it the rate-determining step (rds) for the overall reaction, Equation 3[16,17]. Significant efforts have been made to improve the ORR to improve performance.

Anion Exchange Fuel Cells

Similar to the PEMFC is the anion exchange membrane fuel cell (AEMFC). In the AEMFC, OH^- ions are transported across the membrane instead of H^+ ions. The electrode

reactions are slightly different in the case of AEMFC: hydrogen fuel delivered to the anode is oxidized with OH^- to produce water displayed in equation 4.

$$H_2 + 2OH^- \longrightarrow 2H_2O + 2e^- \qquad (4)$$

On the cathode, oxygen is reduced to water via equation 5. Equation 3 still describes the overall cell reaction for an AEMFC even though the transported ion is different.

$$\frac{1}{2}O_2 + 2H_2O + 2e^- \longrightarrow 2OH^- \qquad (5)$$

As for the PEMFC, the anodic and cathodic reactions are known as the hydrogen oxidation reaction (HOR) and oxygen reduction reaction (ORR), respectively. Likewise, the membrane of the AEMFC provides separation of the fuel and oxidant, eliminating internal short circuits while providing a pathway for anionic transfer.

In an alkaline electrolyzer system, water is supplied to the cathode, where it is reduced to produce hydrogen gas and hydroxide ions via an applied potential shown by equation 4R. This reaction is known as the hydrogen evolution reaction (HER).

$$2H_2O + 2e^- \longrightarrow H_2 + 2OH^- \qquad (4R)$$

On the anode, hydroxide ions are oxidized to produce oxygen gas and H_2O, shown by equation 5R. This reaction is known as the oxygen evolution reaction (OER). Eq. 3R describes the overall electrolyzer reaction for both PEMFC and AEMFC.

$$2OH^- \longrightarrow \frac{1}{2}O_2 + H_2O + 2e^- \qquad (5R)$$

$$H_2O \longrightarrow \frac{1}{2}O_2 + 2H_2 \qquad (3R)$$

AEM devices were developed in the early 2000s as inexpensive and earth-abundant metals, or precious group metal (PGM)-free metals, were found to be useful as electrocatalysts for the O_2 reactions in alkaline mediums[18-21]. PGM-Free metals' use ultimately reduces cost while maintaining O_2 reaction rates, sparking interest in AEM research in the FC community, as costly PGMs are the primary catalysts for both anodic and cathodic reactions for PEM devices[22]. In each of these systems, a catalyst is used to lower the activation energies and increase the rate of their respective reactions.

Unlike PEM systems, in AEM systems, efficiency is lost due to sluggish kinetics of both the HOR/HER, and the ORR/OER[23-26]. The development of highly active hydrogen catalysts for AEMFCs has become of important due to the possibility of lowering system cost by moving towards AEMFC[27].

Rationales for the Sluggish Kinetics of Hydrogen Electrocatalysts In Alkaline Media

It is widely accepted that the HOR /HER precede through the elementary reactions known as Tafel, Heyrovsky, and Volmer mechanisms. The Tafel step being purely

adsorption driven, and the Heyrovsky and Volmer steps being adsorption and electron transfer driven. Additionally, the hydrogen reactions typically proceed through a variation of either a Tafel-Volmer or Heyrovsky-Volmer process. It is widely accepted that the Volmer step is the rate-determining step[23,28].

$$\text{Tafel: } \boldsymbol{H_2 + 2M \leftrightarrow 2H_{ad}} \qquad (6)$$

$$\text{Heyrovsky: } \boldsymbol{H_2 + OH^- + M \leftrightarrow H_{ad} + H_2O + e^-} \qquad (7)$$

$$\text{Volmer: } \boldsymbol{H_{ad} + OH^- \leftrightarrow M + H_2O + e^-} \qquad (\mathbf{8})$$

In equations 6-8, $\boldsymbol{H_{ad}}$ denotes hydrogen adsorbed on an active catalytic site for HOR/HER.

Pt was chosen due to its optimal balance in H_2 adsorption strength and reactivity in acid when initially seeking a hydrogen catalyst for alkaline environments[23-28]. However, this relationship changes as a function of pH. The exchange current density, i_o, is a measure of the rate of the reaction where a larger i_o implies a more facile reaction[29]. As the pH is increased,0 so does the hydrogen binding energy (HBE), resulting in a decrease in i_o[30]. This relationship is known as the Hydrogen Binding Energy Theory[23,24,30-32]. This theory ties the decrease in kinetics, i_o, to the increase in H_2 binding energy. The HBE is calculated by taking the peak potential, E_{peak}, in the H_{upd} region and multiplying it by Faraday's constant, F to give the Gibbs free energy, ΔG_{HBE}, of hydrogen binding to the metal shown by Eq. 9[30].

$$\boldsymbol{\Delta G_{HBE} = E_{peak} * F} \qquad (\mathbf{9})$$

Furthermore, density functional theory calculations of the HBE marry closely with calculations using Eq. 9. Tafel analysis via fitting or linear current region extrapolation is typically utilized to calculate i_o [24,28,33]. Desorption of hydrogen from the catalytic site remains key to enhancing the kinetics of the HOR as the Volmer step is the rate-limiting step. This implies that by manipulating the effective surface energy of Pt one can decrease its HBE, increasing catalytic performance.

Several studies have found that bimetallic catalysts can impact the relative surface energy of Pt by lowering its HBE, resulting in increased activity. This increase in activity has been attributed to the Bifunctional Mechanism[34-37]. The Bifunctional Mechanism suggests that the alloying of an oxyphilic metal to Pt promotes water dissociation, easing the generation of H_{ad} as the reactant of the H_2 recombination on adjacent Pt sites for the HER. For the HOR, the adsorbed hydroxide anion on the catalytic site (OH_{ad}) hosted on these oxyphilic sites facilitates the removal of H_{ad} on adjacent Pt sites[23, 34-37]. Thus, the use of bifunctional catalysts lowers the Volmer step's energy barrier via the bifunctional mechanism.

Aside from the two theories mentioned above centered on electrocatalytic characteristics, two other accepted theories attribute the sluggish hydrogen kinetics to the alkaline electrolytes' characteristic, namely the HBE theory and bifunctional mechanism. The Potential of Zero Free Charge Theory (PZFC) states that increasing the pH causes the PZFC to shift more positively [38-40]. Therefore, the HOR/HER potential is more negative to the PZFC. The shift in PZFC relative to the H_2 reaction potential increases transport limitations for OH^- and H^+ in solution because of increased disorder of water

molecules in the double layer, which further increases the energy barrier for the Volmer step[38].

This positive shift in the PZFC is also a direct function of the alkaline metal cation (AM^+) present in the alkaline solution[38-39]. The higher the atomic number of the AM^+, the more positive the PZFC shifts, adding to the decrease in overall kinetics. The concentration of the alkaline electrolyte also affects the kinetics of hydrogen reactions in alkaline mediums. Higher concentrations of AM^+ allow for the development of OH_{ad}-$(H_2O)_x$-AM^+ adducts that aid in the HER as per the hard-soft acid-base (HSAB) theory,but these adducts impede the HOR by destabilizing the OH_{ad} per the bifunctional mechanism.

This theory is known as the 2B theory, which takes into account the trend of changing the AM^+ species per the HSAB theory[41,42]. The Volmer step becomes equations 10 and 11 with the addition of the OH_{ad}-$(H_2O)_x$-AM^+ adduct into the reaction[42].

$$\boldsymbol{H_2O + (H_2O)_x - AM^+ \leftrightarrow H_{ad} + OH_{ad} - (H_2O)_x - AM^+} \qquad \boldsymbol{(10)}$$

$$\boldsymbol{OH_{ad} - (H_2O)_x - AM^+ + e^- \leftrightarrow OH^- - (H_2O)_x - AM^+} \qquad \boldsymbol{(11)}$$

These AM+ adducts improve the Volmer step for HER by driving OH_{ad} into the bulk electrolyte forming OH^-, but ultimately hinder the HOR on Pt catalysts[23, 42]. These four principal theories; The HBE Theory, The Bifunctional Mechanism, The PZFC Theory, and the 2B Theory, have been the focus of study in order to increase hydrogen catalytic activity for AEM devices.

Electrocatalysis For Electrochemical Devices

Electrocatalysts are an essential component of any electrochemical device. The catalysts' function is to lower the activation energy of the redox reactions that occur in the devices. These catalysts are conventionally metallic nanoparticles dispersed on conductive supporting material, such as carbon[43-45]. This design lowers the catalyst's overall cost by lowering the total metal content required while increasing electrochemical surface area and providing conductive pathways via the conductive support. State-of-the-art hydrogen catalysts for AEMFC are primarily precious group metal (PGM) based[24-26, 28, 46, 47]. Studies of catalytic performance are generally compared to high surface area carbon-supported nanoparticles of platinum (Pt/HSC or Pt/C), a staple in the FC catalysis field [43-45, 48]. Other expensive PGMs, such as Ir, Ru, and Pd, have been investigated as catalysts for HOR/HER; however, these catalysts have shown reduced activity in rotating disk electrode (RDE) systems when used alone[24-26]. Inherently, Pt alloys made with these noble metals have been utilized to lower the Pt content in the catalyst layer (CL) and increase performance. PtRu/C bifunctional catalysts have exhibited increased kinetic performance for the HOR/HER in alkaline electrolytes due to the bifunctional mechanism[49].

Although PGM catalysts have proven to be sufficiently active for HOR/HER in alkaline environments, their cost and still inadequate performance prevent alkaline devices' general commercialization. Therefore, less expensive alternatives offering similar performance to Pt have been sought. Various transition metals have been studied for their performance as hydrogen and oxygen catalysts in both alkaline and acidic media. These catalysts, classified as PGM-free catalysts, have become the great focus of current

research. These PGM-Free metals can be used alone or alloyed together or with PGMs to improve activity. Nickel-based HOR/HER catalyst supported on carbon have become the premier PGM-free catalysts, potentially allowing for a PGM-free AEM device[25, 26, 31, 46]. The state-of-the-art PGM-free catalyst is trimetallic CoNiMo, which exhibits a fraction of PGM-based catalyst performance[25, 50].

In basic conditions, the durability of Pt/C catalysts is significantly lower than in acidic. Basic conditions tend to be harsher, promoting carbon corrosion and contributing to Pt dissolution/redisposition and agglomeration, decreasing the ECSA of the catalyst[51]. Studies have been conducted to increase the durability of electrocatalysts for FC systems. In HSC supported catalysts, the carbon can oxidize at operating potentials resulting in Pt agglomeration, decreased conductivity of the catalyst layer (CL) [44, 52-54]. Typical support alternatives have been metal-doped titanium oxides, which are more resistant to oxidation [55-59]. However, these oxide supports exhibit lower performance compared to Pt/HSC due to their relatively lower electronic conductivities. Because AEMFC research is in its infancy, the durability of catalysts has been secondary to performance in research emphasis.

Electrocatalysis Synthesis Methods: Atomic Layer Deposition

Atomic Layer Deposition (ALD), formerly known as Atomic Layer Epitaxy (ALE) was initially developed to produce thin-film electroluminescent (TEFL) flat panels[60]. In characterizing these panels, it was found the method deposited thin layers of material with high uniformity on large area substrates. This method has been adapted to develop other thin films and eventually nanoparticle material for use in various applications. There are two classes of ALD reactors that are employed: inert gas flow and high-vacuum

reactors. The choice of the reactor is dependent on the volatility of the utilized precursor. The most common ALD reactors are inert gas flow reactors ranging in price starting at $100,000.

ALD is a cyclic process of exposure and purges. The substrate that may itself be functionalized is exposed to an initial precursor that deposits the desired metal on the substrate through substitution reactions. A purge is then used to remove residual ligands from the initial precursor and the reaction chamber is evacuated. A second precursor is used to functionalize the newly formed surface of the deposited species. The cycle is completed with a final purge to remove any residual secondary precursor. Once the first layer is deposited and functionalized, the cycle repeats until the desired morphology is met[60,61].

ALD is a self-limiting process; after the surface functionality is depleted, the deposition stops, making it advantageous as a highly controlled synthesis process. Additionally, ALD supports a wide temperature window, capable of utilizing various materials as substrates and precursors[60]. A significant feature of ALD is that it does not require constant homogenous flux of vaporized precursors to achieve high uniformity or reproducibility as the reaction is purely surface driven[61].

The substrate surface must possess some initial functionality before deposition to facilitate the initial exposure step of the ALD process[61]. Typical substrates are metal oxides, where the oxygen functionality is exploited to deposit transition metals. In electrochemical devices, carbon is an excellent support of choice, mainly due to its high conductivity and low cost. However, these carbon supports are typically unfunctionalized, leading to additional steps to prepare the support for deposition. The metal surface

interaction (MSI) also increases using ALD compared to other deposition methods, as the Pt molecules are chemically adsorbed onto the surface of the support, whereas the Pt is physically adsorbed in other methods[61]. This increase in MSI leads to less agglomeration in operating conditions, increasing the durability of the catalyst.

For electrochemical applications, ALD has been used to deposit PGM and PGM-free metals on various surfaces as mono and polymetallic nanoparticles[62-69]. Because of the high control, these nanoparticles range from 1-13 nm in diameter with minimal particle size distribution. Particles of this size lead to lower cost of catalysts due to the increased surface area with a smaller mass deposited[61]. Additionally, highly active bimetallic Pt-M electrocatalysts have been developed through ALD such as PtRu, PtCo, and PtNi, in various configurations of the deposits, such as core-shell nanoparticles and alternating metal staked nanoparticles[61, 63]. Core-shelling places an oxyphilic metal inside a Pt shell, which lowers the outer shell's hydrogen binding energy, thereby enhancing performance. In alternated metal stacked nanoparticles, the ALD cycle adds a third metallic precursor, and the deposited metal is alternated to form alloys.

ALD has proven to be a highly controlled facile way to produced electrocatalysts for electrochemical devices making it a useful technique in research. However, the high cost of the reactors and precursors leads to an increase in the final product's cost. Although conventional ALD can produce a film of 100-300 $nm*h^{-1}$, the scalability of ALD is completely dependent on the reactor size, limiting the yield of catalyst prepared [60]. These limitations make ALD less attractive for commercial catalyst producers.

Electrocatalysis Synthesis Methods: Solution-Based Methods

Solution or chemical reduction-based synthesis processes are fundamental in the development of catalysts for a myriad of applications. For this reason, this method has become the standard technique in synthesizing commercially available catalysts for low-temperature FCs[70-73]. Because of this method's versatility, efforts have been made to systematically increase the activities of the hydrogen and oxygen reactions in these devices by controlling the size and distribution of the deposited nanoparticles and controlling their shape to promote higher reaction rates[74-78].

The most common reduction synthesis process for platinum electrocatalysts involves a precipitation method, where the catalyst support is suspended in deionized water and mixed vigorously. The pH of the water is raised via the addition of a base such as NaOH. The addition of chloroplatinic acid ($H_2PtCl_6 \cdot 6H_2O$) and a reducing agent (e.g., hydrogen, formic acid, or formaldehyde) results in an acid-base elimination reaction, reducing the Pt precursor to its constituents. The precipitated Pt is then deposited onto the support's surface. The slurry is then rinsed, filtered, and dried, resulting in bulk catalyst synthesis[70]. Finally, a heat-treatment is applied to the bulk catalyst to reduce the metal nanoparticles fully. This method has been popularized due to its low cost and high output of reactive PGM catalysts.

In solution-based methods, the growth of these nanoparticles is influenced by the reactant concentration, reaction temperature, pH, and time[76]. Varying these parameters, as well as adjusting the reactant ratios, has led to several improvements in catalytic activity as well as novel conformations of nanoparticles[74-77]. Particle size is a leading factor in improving the catalytic activity as smaller particles increase the effective

surface area. Additionally, the exposed predominate crystal facet on the surface of the nanoparticles causes variation in performance due to the variations in surface energies[74,75].

Solution-based methods have been used to produce a variety of catalyst for electrochemical applications. A common product developed using this reduction process is Pt nanoparticles supported on carbon[75,78]. The particle sizes obtained using this method range from 1-4 nm. The selection of the solvent or base used in these reactions is the main factor in the particle size variances[78]. Additionally, Pt-M electrocatalysts are prepared using this method; these catalysts can be metal alloy particles, core shells, clusters-in-cluster, or shaped-controlled alloyed nanoparticles. For metals with FCC atomic coordination, the {111} plane family has the lower surface free energy, making it the most stable facet for these reactions to take place. Although less stable than the {111}, the {100} and {110} families are assumed to be more reactive. As such, the design of the nanoparticles synthesized through reduction methods is centered on obtaining high {111} surface area and reducing the concentration of other orientations on the exterior[74,75]. To achieve this, shapes such as nanoplates, tetrahedra, cubes, cuboctahedra, and octahedrons, are commonly developed, improving either stability through increased {111} concentrations (Tetrahedra and octahedron), reactivity through fixed structures with {100} & {110} families only (cube, rhombic dodecahedron), or both by combining these planes in an ordered fashion such as a truncated octahedron[]. Due to the amount of material needed (i.e. the number of atomic layres in the particle) to produce these unique nanocrystal geometries, the size of the deposited nanoparticles increases to 5-20 nm[74-78].

Although the process can be tuned to achieve the desired shapes and size, the synthesis process is still challenging to control as the substrate is dynamic and promote the homogeneous distribution of the deposited metal. However, a way to control the rate of agglomeration has not been discovered, leading to decreased reactivity of the electrocatalysts in operation[74]. Additionally, the particle sizes required to produce the novel geometries of catalyst that increases performance increases the amount of Pt in the electrocatalyst of PEM/AEM devices. This is counterproductive for the commercialization of these catalysts, although they provide interesting findings for a solution to the balance of cost and performance/durability in the future. Regardless, this method is typically selected as the main means to synthesis commercial-grade electrocatalysts due to the product yield being tied to the volume of the reaction vat and recovery process. Furthermore, the synthesis of the chloroplatinic acid precursor is facile, reducing catalyst synthesis cost per $gram_{pt}$.

Electrocatalysis Synthesis Methods: Conventional CVD

CVD is a broad colloquial term used to describe processes that involves the vaporization of a precursor and subsequent decomposition and deposition of the desired component of that precursor on a substrate. ALD is a form of CVD. CVD methods have been used in several aspects of catalyst synthesis for electrochemical devices[79-89]. The main products of this method are various structured carbons supports such as nanowires, nanotubes, and graphene sheets. Due to the multiplicity of this process, CVD is also employed to deposit metals and metal-organic compounds as films, powers/particles, and fibers.

Conventional CVD methods are described by a 7-step process: 1: a solid or liquid precursor is either sublimed or vaporized respectively and injected with a carrying gas to the reaction chamber, 2: the reactants in the vapor diffuse into an initial boundary layer below the flow stream of the carrying gas, 3: the reactants then come in contact with the substrate where 4; deposition takes place; 5: gaseous byproducts are then diffuse away from the substrate to the boundary layer; 6: the byproducts are then diffuse through the boundary layer and 7: evacuated out with the residual carrying gas and undeposited reactants. The rate of deposition is determined by the slowest rate throughout these sequential steps.

The phase of the precursor used in CVD can vary based on the type of CVD being conducted. The most applicable CVD form for our studies is metal-organic chemical vapor deposition (MOCVD). This process utilizes solid metal organic salt precursors, which can be vaporized at lower temperatures (300-800 ^{o}C) than general thermal CVD, under pressures ranging from 0.13 kPa to atmospheric. In MOCVD, the equipment and precursors used in CVD are commercially available but expensive; therefore it is typically used in applications where high quality is essential[82-85, 90].

As previously mentioned, CVD is primarily used to prepare supports for electrochemical devices. Carbon nanotubes provide high surface areas, enabling smaller particles to be produced through solution-based deposition processes. The combination of CVD and reduction methods is common in literature. The CVD process allows the production of highly ordered carbons with reduced surface functionality, whereas the solution synthesis enables rapid deposition of metals on the support. Conventional CVD produces nanoparticles that are ~2-4 nm in diameter when used to synthesize Pt/C

electrocatalyts[83, 84]. Additionally, CVD is capable of alloying metals in a controlled manner [91, 92].

Like ALD, CVD is not restricted to a “line of sight” deposition allowing the deposition to occur in deep recesses of various supports and sacrificial templates such as inside nanotubes[90]. These voids can be coated or filled based on the concentration of precursor used. The rate of deposition for CVD is high and is a function of the precursor used. The variations in deposition rates are closely tied to the decomposition rates for each precursor. Additionally, a high vacuum is not required for many CVD methods, enabling the deposition of various elements at the same time such that vaporization conditions for the limiting reagent are met[90]. Although these advantages describe CVD to be a holistic solution to many problems in synthesis, there are some disadvantages outside of cost that dismiss it as the absolute method. MOCVD has significantly reduced the necessary temperatures required for conventional CVD (<600 ^{o}C); however, several supports are nonetheless unstable even at the temperature range for MOCVD[90]. Moreover, the decomposition by-products of CVD can be toxic, requiring neutralization of these volatiles, potentially increasing cost as well.

Modified CVD Method

Cost, particle dispersion, and control of particle size must be considered in the development of a commercially viable catalyst synthesis process. Sublimation of metal-organic compounds has proven to be a convenient process at lower synthesis costs. Recently, catalysts have been synthesized employing a modified CVD process at the University of Tennessee, known as the Poor Man’s CVD method[89, 93-98]. This process has produced highly dispersed catalyst on various supports verified by scanning

transmission electron microscopy (STEM). In this process, a low-cost vacuum oven is utilized to allow for lower decomposition temperatures of metal-organic salt CVD precursors. One intriguing product of this process is unsupported Pt nanotubes synthesized by depositing Pt on a sacrificial anodic alumina template, which exhibits higher mass and specific activities than commercially available Pt/C catalysts[96].

Furthermore, the PMCVD process has been used to develop precious metal alloys that exhibit better performance than Pt alone in a solid acid fuel cell, characterized by polarization curves[93]. In addition to the capability of alloying metals with PMCVD, unsupported bimetallic nanotubes have been synthesized, again with higher mass and specific actives in comparison to conventionally synthesized commercial catalysts. The nanotube synthesis process has produced extremely high geometric surface area catalysts verified by the Brunauer Emmett and Teller (BET) surface area analysis method.

The PMCVD process involves mechanically mixing an electronically conductive support with a chosen metal-organic salt precursor followed by sublimation of said precursor at low pressure and elevated temperature. The typical precursors used for this procedure are metal acetylacetonates ($M(acac)_x$) [$M^{+x}(C_5H_7O_4)_x$]. These precursors have been chosen for their low decomposition temperatures and minimal oxidation of the deposited metal at low-temperature ramp rates[66]. The decomposition temperature of the air-stable and commercially available $Pt(acac)_2$ complex is about 237 ^oC, and its vapor pressure is approximately 0.5 kPa at 210 ^oC. The decomposition of the acac ligand results in the deposition of metallic particles on the support on the order of ~2-4 nm confirmed via scanning transmission electron microscopy (STEM)[93-95, 98].

Studies of the decomposition of the metal-organic precursors' mechanism analyzed via gas chromatography-mass spectrometry (GC-MS) show that cationic metal is reduced to metallic metal at the expense of the oxidation of the acac ligand. Oxidation of the cationic metal subsequently occurs when the acac or HFac [$M^{+x}(C_5H_1F_6O_4)_x$] ligand is not entirely oxidized, resulting in metal oxides depositing on the support[81, 82]. The reduction or oxidation of the deposited metal was discovered to be a function of time, temperature, and pressure [99, 100].

CHAPTER II

ON THE DEPOSITION MECHANISM AND MATERIAL CHARACTERIZATION OF MODIFIED CHEMICAL VAPOR DEPOSITION SYNTHESIZED CARBON SUPPORTED PLATINUM NANOPARTICLES

Abstract

Chemical Vapor deposition (CVD) is a common technique utilized to synthesize catalysts for electrochemical devices. Typical CVD processes involve the sublimation of various metal-organic salt precursors in a separate reaction chamber, followed by the vapor being transported through a deposition chamber via a carrying gas and subsequent deposition of the metal on a support. Our modified vapor deposition process eliminates the multistage reactor and simplifies the reaction to a single vat process. In this study, we look at the deposition process's efficiency concerning the amount of recovered metal to demonstrate its high metal recovery and throughput. We discuss the deposition mechanism and rate laws for the modified process determined by varying the metal-organic salt precursor's concentration and analyzing the deposited nanoparticles through various material characterization techniques. Lastly, we do a thorough analysis of the deposited species to confirm that the modified deposition process requires a single step to produce fully reduced Pt nanoparticles, with diameters averaging 3 nm, which can be immediately used as a catalyst for various reactions.

Introduction

Many techniques are used to develop electrocatalysts for electrochemical devices such as fuel cells and electrolyzers. One common practice is chemical vapor deposition (CVD)[85-88]. Conventionally in this technique, a metal-organic salt is sublimed, passed through a reactor tube via a carrying gas. The metal precipitates from the vapor due to thermal gradients in the tube. The metal is then deposited onto a substrate or supporting material, resulting in a final product. The products range from sheet deposition to

nanoparticles[79-88]. The residual vapor, containing some undeposited metal, passes along with the carrying gas as waste. The recovery of these metals can be significant when using precious group metal precursors (e.g., Platinum, Palladium, and Gold) as the production cost increases, resulting in a more expensive final product[83-85, 87,88]. Other synthesis methods offer higher recovery regarding mass conservation efficiency than conventional CVD.

These aforementioned techniques, such as atomic layer deposition (ALD) and sputtering, result in a lower deposited metal loss [60-69, 101-103]. Although these techniques enable higher yields of recovered metal on the substrate, the manufacturing cost and production time outweigh the efficacy increase when scaled for commercial development[60, 61, 65, 66]. A more accepted process is solution-based synthesis, in which the deposition reactions occur in a flask[70-78]. Utilizing a single vat process allows for lower production costs. However, these heterogeneously synthesized electrocatalysts often require post-synthesis treatments to refine the product, which decreases the output efficiency for commercially sustainable products.

In 2012, a nonconventional CVD method was explored by the Zawodzinski Group to synthesis electrocatalysts for various electrochemical reactions and devices. Similar to conventional CVD, they utilized a metal-organic salt precursor[49, 93-98]. By mixing the salt with supporting material, they have produced highly dispersed metallic nanoparticles of uniform size while accounting for a large majority of the metal's initial mass in their final product. This process typically occurs in a single-step, like ALD and sputtering, removing the need for post-treatments necessary in solution-based methods. This streamlined process ultimately reduces the time and cost of synthesis.

Although this method consistently produces uniform and well-distributed metallic nanoparticles, there is still much unknown regarding the CVD variant's deposition mechanism. Many studies have been conducted to understand conventional CVD precursors' decomposition mechanisms. Nesibulin et al. studied Cu(acac)2 extensively, where they determined that the full reduction of the metal is at the expense of oxidation of the acac ligand, leading to fully reduced nanoparticles deposited on a substrate[82]. In addition to this process's unknown deposition mechanism, the impact of the metal-organic salt precursor concentration on the product's nanoparticle size and distribution has not yet been investigated.

In this study, we investigate the impact of varying the concentration of a platinum acetylacetonate [Pt(acac)2] precursor on the modified chemical vapor deposition process. Through this, we propose a stepwise deposition mechanism for the nucleation and growth process during the deposition process and propose rate laws for the associated deposition steps.

Experimental

Nanoparticle Synthesis. All catalysts were synthesized using a modified chemical vapor deposition process using Vulcan Carbon XC-72R (Cabot) supports and a platinum acetylacetonate precursor. The powdered Platinum (II)(2,4)-pentanedionate [$Pt(acac)_2$] (Alfa Aesar) precursor was mechanically mixed with the Vulcan XC-72R carbon support in glass vials to achieve the appropriate final metal loading of 10, 30, and 50 wt% Pt; total mass was 50 mg for each sample. The vials were then placed into a vacuum oven along with a separate vial containing a small amount of deionized water (Milli-Q, Millpore). The oven was then sealed, evacuated with ultra-high purity N_2 to 28.37 kPa, and the

temperature was set to 210 ^{o}C. After 15 hours, the oven was turned off, and the residual volatiles were purged from the oven chamber three times. The oven was then left to cool until the oven temperature was 50 ^{o}C. At this time, the oven was then brought to atmospheric pressures, and the vials were left to cool to room temperature in an ambient environment. Once equilibrated, the products were then measured to determine the deposited metal mass via a mass balance. Table 2.1 provides details of the mass balance and the percentage of Pt recovered.

Materials Characterization: The various Pt/ XC-72 catalysts were analyzed using x-ray diffraction (XRD), transmission electron microscopy (TEM), and x-ray photoelectron spectroscopy (XPS). XRD patterns were obtained using a Siemens D5000 diffractometer using Cu radiation (l=0.154184 nm, 30kV 40mA, 0.05^{o} step, 1.0 ^{o}/min) in a Bragg-Brentano geometry. Aliquots of catalysts suspended in isopropyl alcohol (IPA) were smeared onto a zero-background quartz sample holder. The IPA was evaporated before measurements. Peak width analysis was performed using Igor Pro using a Voigt wave fitting function. TEM micrographs were taken using an FEI Titan ETEM with Image Cs corrector operating at 300 keV, equipped with a Gatan K2-IS direct detection camera and a Gatan single-tilt holder. The electron flux to the sample was limited to 10 e^{-}/px/s to minimize beam damage. XPS measurements were performed on a Kratos Ultra DLD spectrometer using a monochromatic Al K_{α} source operating at 150 W (1486.6 eV). The operating pressure was 5 x 10-9 Torr. High-resolution Pt 4f and C 1s spectra were acquired at a pass energy of 20 eV. The XPS data was processed using Casa XPS software.

Table 2.1: Mass Balance/ Platinum Recovery

Sample Name	Initial mass (mg)	Expected mass (mg)	Recovered mass (mg)	Recovery Efficiency (%)
10% Pt/ XC-72	10.1	5.0	4.6	92
30% Pt/ XC-72	30.2	15	15	>100
50% Pt/ XC-72	50.4	25	24.4	97.6

Results and Discussion

Our mass balance displayed in Table 2.1 shows that this nonconventional CVD method is highly efficient in retaining Pt throughout the deposition process. The mass efficacy was calculated by comparing the expected Pt mass, calculated based on the initial measured mass, to the recovered Pt mass post-deposition. The scale used has a reliability of 1.0 mg, thus our efficacies approximate the modified CVDs metal recovery. The average recovered mass efficiency is 96.5%. This method proves to be a viable option for developing products using precious metal-organic salt precursors as an increase in recovery efficacy lowers production cost.

X-ray diffraction was used to determine our sample's phase and crystallite size. Figure 2.1 shows the diffraction patterns for our three samples. The Platinum (111) peak intensities relative to the carbon (002) peak results from varying the concentration of Pt in our samples. The noise to signal ratio observed decreases as we grow larger crystallites in our sample. We measured the crystallite size by analyzing the Pt (111) facets' peak width using the Scherrer equation, Equation 2.1. Where L is the

$$\boldsymbol{L = \frac{\lambda \times 0.94}{\beta_L \times \cos\theta}} \qquad (\mathbf{2.1})$$

crystallite size, b_L is the Full Width at Half Maximum (FWHM), of the Pt (111) peak, l is the wavelength of the incident x-ray beam (1.5406 Å), and q is the Bragg angle of diffraction for the Pt (111).

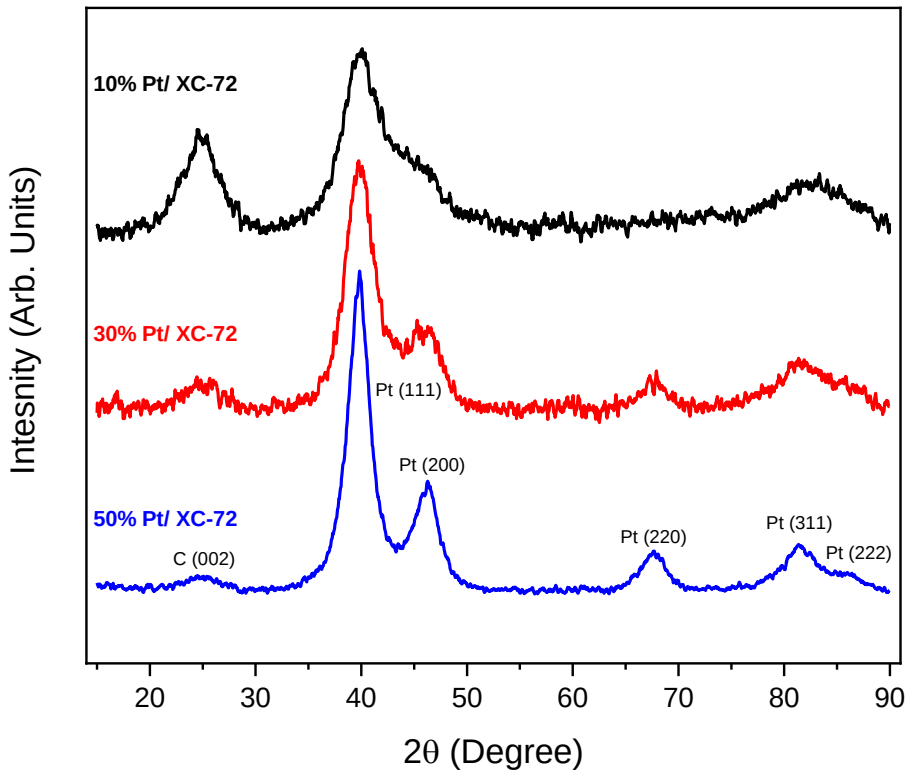

Figure 2.1: Cu K_α X-ray diffraction patterns of varied wt. % of Pt on XC-72. The peak intensities associated with the various planes of diffraction in the Pt nanoparticles increase with an increase in Pt loading.

Because of the small crystallite size, analyzing the crystallite size through Sheerer equation alone, only provides an estimate of the deposit's crystallite size. Other factors such as microstrain and sample surface displacement can impact this calculation. A Rietveld Refinement would allow for lower error in the determination of the crystallite sizes. However, for comparison purposes, the utilization of Equation 2.1 is sufficient. This rational is relevant though the document.

Table 2.2 provides the calculations of each sample's lattice parameters using the peak location of the Pt (111) facet. To determine each sample's lattice parameter, we calculated the interplanar spacing, d, using Braggs Law, Equation 2.2, using the same variables defined in Equation 1. We then calculated the lattice constant, a, using Equation 2.3, where h, k, and l are the miller indices associated with the diffracted plane analyzed in Equation 2.2.

$$\boldsymbol{\lambda = 2d \sin \theta} \qquad (\mathbf{2.2})$$

$$\boldsymbol{d_{hkl} = \frac{a}{\sqrt{h^2 + k^2 + l^2}}} \qquad (\mathbf{2.3})$$

Figure A2.1 further illustrates our findings by plotting crystallite size vs. loading. Using a linear fit, we show that by varying the metal-organic salt precursor's concentration, we can tailor the crystallite size observed in our samples with a high correlation factor of R^2= 0.96. The slope depicts the crystallite size growth as we increase the metal loading.

Table 2.2: Crystallite size and lattice parameter of 10, 30, and 50 wt. % Pt/XC-72. Standard deviation is included for the average measured particle size in parentheses. Lattice parameters were calculated using Braggs Law. Crystallite size, L, was calculated using the Scherer Equation. Particle sizes were determined by manually measuring the diameter of 100 nanoparticles using ImageJ software.

Sample Name	**a (Å)**	**Peak Position (2θ)**	**FWHM (º)**	**L (nm)**	**Particle Size (nm)**
10% Pt/ XC-72	3.91851	39.813	4.256	1.99	2.48 (.65)
30% Pt/ XC-72	3.91511	39.849	3.403	2.48	2.88 (.58)
50% Pt/ XC-72	3.92217	39.774	2.557	3.30	3.42 (.91)

From the diffraction pattern analysis, we further assess that regardless of metal loading, the deposition process provides consistency in the phase deposited at the given reaction temperature and pressure. The indicated phase of the deposited nanoparticles is metallic Pt (FCC). Moreover, we do not see any evidence of residual acac ligand or its derivatives from the decomposition of the precursor in the diffraction pattern. Thus, we can assume that the reaction conditions are sufficient for the metal-organic salt precursor to fully decompose, producing reduced Pt nanoparticles as the deposited species on the XC-72 carbon support.

To understand how varying the concentration of the metal-organic salt precursor affects the deposition products, we analyzed the samples using TEM. Figure 2.2 depicts micrographs of the varied concentration samples at two different magnifications. In the upper line of micrographs, we show a large field-of-view, with a scale bar of 50 nm, clearly displaying the Pt nanoparticles deposited on the XC-72 carbon support. In these micrographs, we see that as we increase the Pt precursor concentration, we see a direct correlation to the amount of agglomeration observed. The agglomeration appears to be more predominant where the carbon support nanoparticles meet. We also see smaller, less dense particles on the carbon particles' surface. The density of atoms found in the nanoparticles can be assessed through the variations in contrast. The higher density particles appear darker in bright-field scanning transmission electron microscopy (BF-TEM). We see this phenomenon more in Figure 2.2f, where the concentration of Pt is highest, as the particles on the carbon support surface are smaller in size than those where the carbon particles meet.

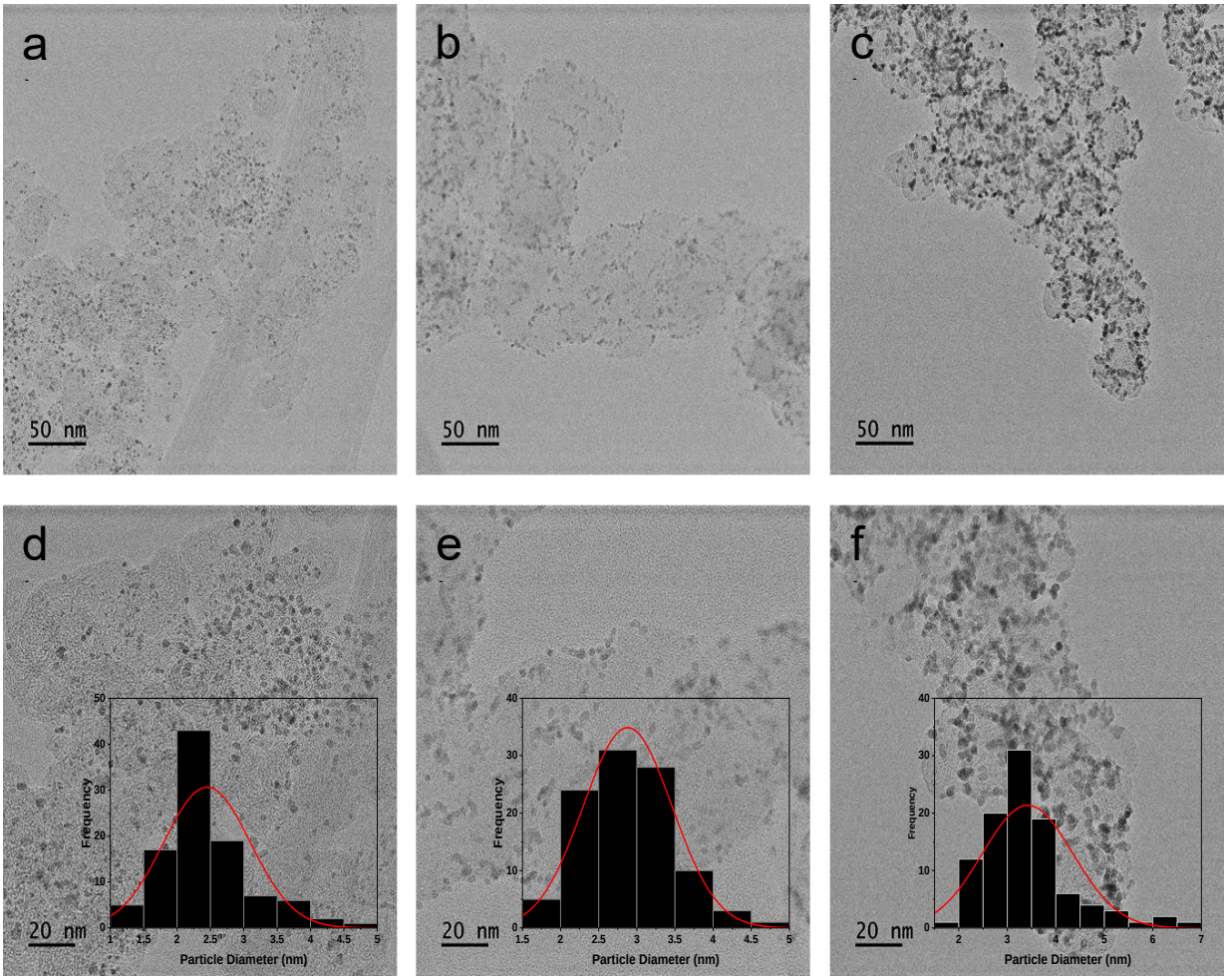

Figure 2.2: TEM Micrographs of (a &d) 10% Pt/ XC-72, (b&e) 30% Pt/ XC-72, and (c & f) 50% Pt/ XC-72. Insets of histograms of measured particle size included in higher magnification images for the respective Pt loadings. Results show the increase in particle size as Pt loading increases.

We measured the average particle size for each of our samples using the higher magnification micrographs. These measurements were accomplished by measuring the diameters of 100 particles manually with ImageJ software. The average particle sizes are included in Table 2.2, with standard deviation included. We found that as we increased the concentration of the metal-organic salt precursor, the average particle size increased accordingly. We also observed an increase in particle size distribution, shown through variations in the x-axis of the histograms in Figure 2.2, leading us to infer that the size distribution induced by the deposition process is a function of the support's physical properties. This finding concludes that the deposition process is a multi-step progression beginning with the nucleation and propagation of Pt seeds that migrate along the carbon surface to lower energy states on the carbon surface.

XPS was conducted to probe the surface of the electrocatalysts to verify the XRD results of the deposited species, being metallic Pt nanoparticles. These results are shown in Figure 2.3. Each sample was executed three times, and the results were averaged. The symmetry in the Pt $4f_{5/2,7/2}$ peaks shows that the deposited nanoparticles are indeed metallic Platinum. We can also compare the measured intensities to the theoretical envelope for metallic Platinum and asses them to be virtually the same. These findings are evidenced in each sample, implying that the precursor concentration has no bearing on the full decomposition of the acac ligand leading to the reduction of the Pt. These results corroborate the XRD analysis proving that the modified CVD process successfully produces metallic Pt nanoparticles of roughly 2-3 nm in diameter in a single-step, single-vat process.

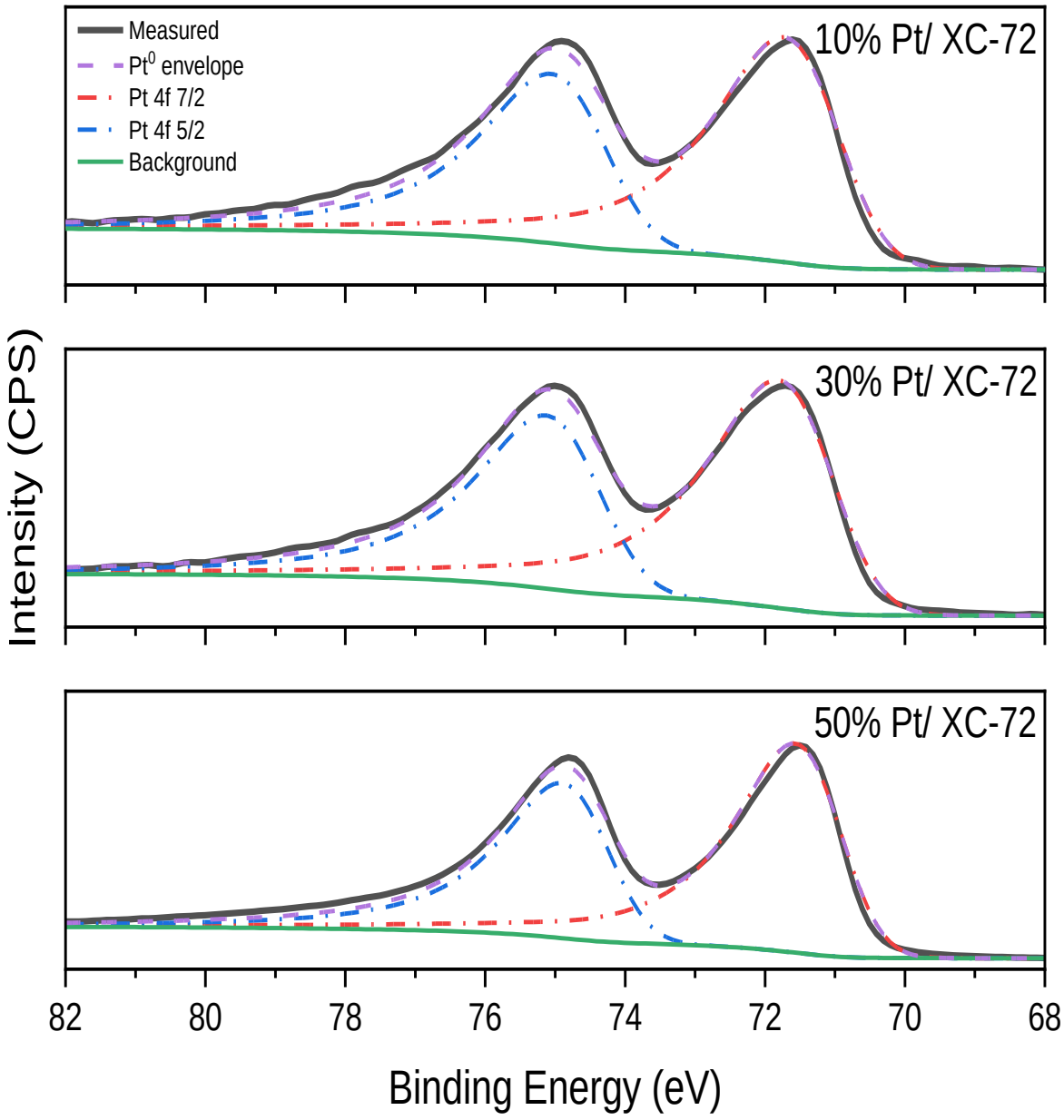

Figure 2.3: XPS results from each electrocatalyst depicting the theoretical phase for metallic Pt in dashed lavender. The black curve shows the average fit of the measured data. The results indicate that each sample contains purely metallic Pt.

Our characterization shows that our modified method is similar in form to conventional CVD deposition process[81,82 85-88]. Figure 2.4 illustrates the proposed deposition mechanism for the PMCVD process. In this figure, we only depict the relevant molecules for each step. The process is initiated by the thermal decomposing of the $Pt(acac)_2$ precursor, breaking down the acetylacetonate ligand into its various gaseous subcomponents previously uncovered via in situ gas chromatography, mass spectroscopy experiments by Nesibulin[81,82]. These subcomponents remain in the gas phase until purged out later in the deposition process.

Because the reaction takes occurs at temperatures and pressures above the vaporization conditions for Platinum, we assume complete vaporization of the metal-organic salt precursor[105-108]. Through the addition of H_2O in the reaction chamber, we drive the full reduction of the Pt by increasing the concentration of O_2 in the reaction chamber. This aids in reducing the amount of available free radicals produced through the decomposition of the acac ligand with the metal surface, promoting the formation of Pt dimer intermediates[107]. These fully reduced Pt dimers subsequently deposit on the carbon surface as Pt seeds. The Pt seeds can then migrate across on the surface to lower energy states, where they coalesce to form nanoparticles[109,110]. These lower energy sites appear to be at the unions of the carbon nanoparticles, as previously described in our TEM analysis. With higher concentrations of Pt, the nanoparticles then continue to coalesce to form agglomerates.

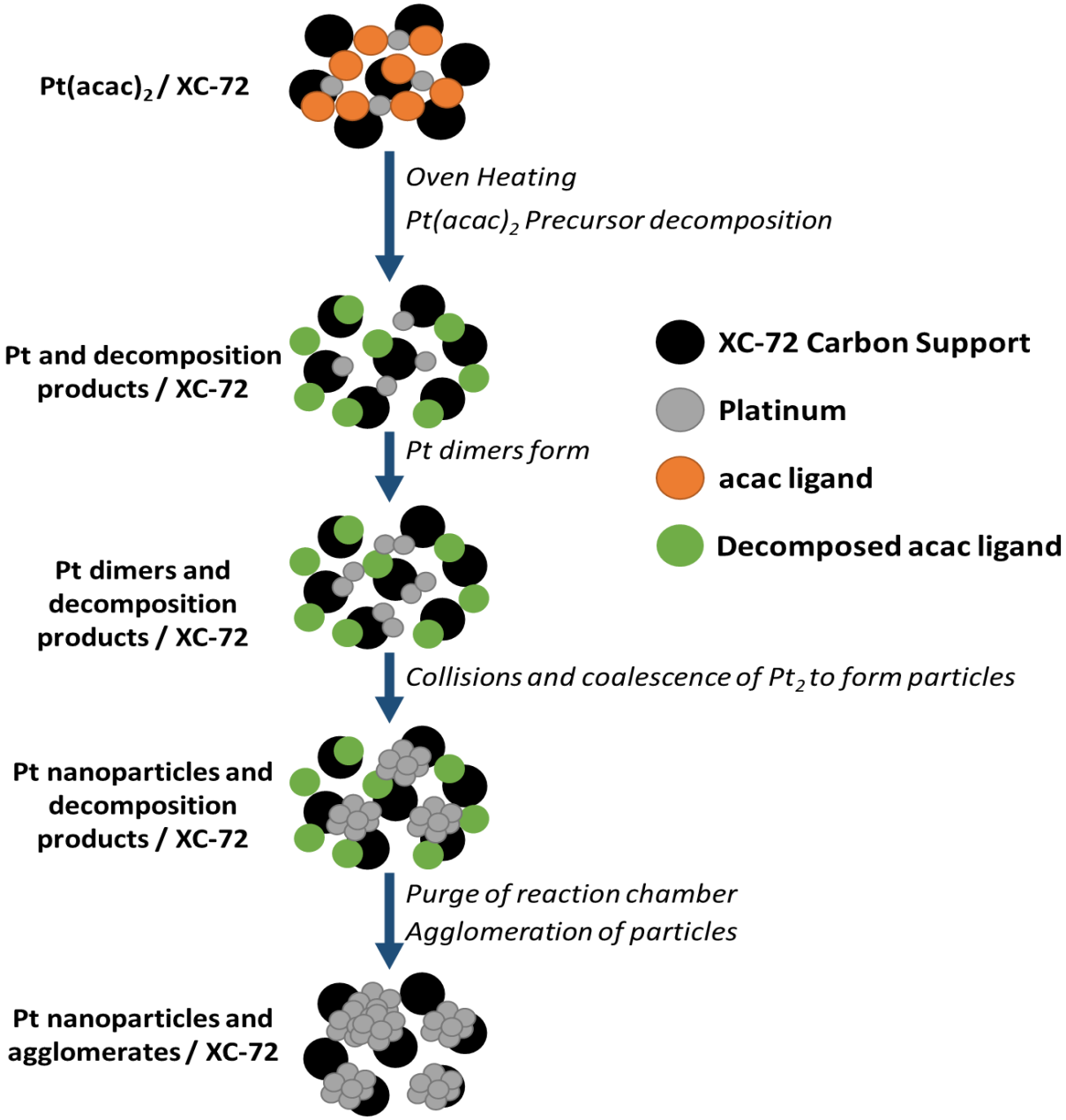

Figure 2.4: Proposed deposition mechanism for the modified CVD process using a $Pt(acac)_2$ precursor. Materials and their subcomponents are labeled in the legend.

We use rate laws to express the deposition as variables that lead to nanoparticle growth and agglomeration development. We describe the deposition as a simple interaction between the Pt molecules and the nucleation sites available on the carbon support; this is shown in equation 2.4, where the * symbol denotes a nucleation site.

$$\boldsymbol{Pt} + * \leftrightarrow \boldsymbol{Pt} - * \qquad (\mathbf{2.4})$$

The rate of this reaction is assumed to be bimodal in nature, where we assume a rate law for nucleation and a separate one for growth. The rate for nucleation is assumed to be second ordered given by equation 2.5:

$$\boldsymbol{Rate_{Nucleation_1}} = \boldsymbol{k_1^o}[\boldsymbol{Pt}][\boldsymbol{N_S}] \qquad (\mathbf{2.5})$$

In this equation, N_S denotes the available nucleation sites for the support, S. Once all sites are filled, e.g. $[N_s]=0$, the deposition rate changes, and the reaction continues until the concentration of Pt, produced from the decomposition of the metal-organic salt precursor, is zero. Thus, we propose a rate law to express nanoparticle growth, coalesces, and agglomeration. Equation 2.6 describes the growth rate as a first-order reaction, which is a function of the reduced Pt concentration.

$$\boldsymbol{Rate_{Growth_2}} = \boldsymbol{k_2^o}[\boldsymbol{Pt}] \qquad (\mathbf{2.6})$$

More energy is needed to initiate the decomposition of the metal-organic salt precursor, leading to the nucleation necessary for particle growth; therefore, $k_{nucleation,1} << k_{growth,2}$. These rate laws are supported by our microscopy analysis, where higher concentrations of Pt lead to larger particles and subsequently more agglomeration. Additionally, it is assumed that the concentration of nucleation sites is constant in each sample to validate the variables in our proposed rate laws.

Conclusion

The modified CVD method utilized in this investigation provides a way to synthesize reduced round Pt nanoparticles supported on XC-72 carbon. Additionally, this modified method achieves these results in a single-vat, single-step process. This study provides evidence of the high metal recovery efficacy achieved through this process, yielding an average metal recovery rate of ~97%. Furthermore, we show through both XRD and XPS that the deposited metal is fully reduced. Through Scherrer analysis, we calculated the crystallite size to vary from 2 -3.3 nm agreeing within error with our TEM analysis were measured our nanoparticles to be an average of 2.9 nm. These measurements varied linearly with the concertation of Pt used, agreeing with our proposed rate law for growth. Through our materials characterization, we proposed a deposition mechanism for our modified process that closely resembles previously proposed mechanisms for conventional CVD. An important variation in comparing mechanisms is our reactants and supports are present together in the initial step. The findings in this study imply the tuning ability of this modified CVD process to achieve desired particle size by varying the concentration of Pt within 10-50 wt. % on an amorphous carbon support. The methods used to characterize the $Pt(acac)_2$ precursor

can be implemented with other metal-organic salt precursors to understand better their impacts on the studied modified chemical vapor deposition process.

CHAPTER III

A PARAMETRIC STUDY OF CHEMICAL VAPOR DEPOSITION SYNTHESIZED HYDROGEN ELECTROCATALYSTS FOR ALKALINE MEDIA DEVICES.

Abstract

The sluggish kinetics of hydrogen reactions in alkaline have precluded the commercialization of alkaline-based electrochemical devices over the last decades. Studies on improving the activities of the electrocatalyst used to overcome the energy barriers for the hydrogen reactions in these devices are common. As such, a close investigation into the microstructure of these electrocatalysts remains significant. The study herein utilizes a modified chemical vapor deposition (CVD) method to tune the microstructure of Pt-based electrocatalyst to enhance their activities for the Hydrogen Oxidation and Evolution Reactions in alkaline media. We observe an increase in activity of these electrocatalysts when the microstrain found in the crystallites of the deposited Pt nanoparticles is minimal, and crystallite size is slightly increased relative to those analyzed in this study. Furthermore, we gain insight into the parametric impact that temperature and pressure have on the utilized deposition process, enabling us to better understand the mechanism of the synthesis process.

Introduction

The development of catalysts for the electrochemical reactions found in hydrogen systems (e.g., fuel cells and electrolyzer systems) continues to be a significant area of research for renewable energy technologies. Currently, proton exchange membrane fuel cells (PEMFCs) are being used commercially as stationary, automotive, and backup power sources and electrolyzers are utilized to produce the required hydrogen to operate these devices[2, 7, 9, 16]. The high cost of these devices is partly attributed to the value of the precious group metal (PGM) catalysts[2, 14]. Within the last few decades, anion

exchange membrane devices have been developed to operate in alkaline conditions enabling the utilization of nonprecious metals to catalyze the oxygen reactions at a much lower cost and thus streamlining commercialization[19-22]. The kinetics of the hydrogen reactions, namely the hydrogen oxidation and evolution reactions (HOR/ HER), decreases by two orders of magnitude in alkaline environments compared to acidic[23, 28]. Consequently, significant challenges in the development of hydrogen catalysts for alkaline systems become more pronounced.

For alkaline media, the hydrogen reactions are depicted by equation 3.1, where the forward reaction describes the HOR, and the reverse reaction depicts the HER. The elementary steps associated with these reactions are the Tafel-Heyrovsky-Volmer mechanism, Equations 3.2-4. Here the * symbol represents an active catalytic site. The Volmer step, Equation 3.4, is widely accepted as the rate-determining step for both HOR and HER[23, 28, 30].

HOR/ HER: $\boldsymbol{H_2 + 2OH^- \leftrightarrow 2H_2O + 2e^-}$ (3.1)

Tafel: $\boldsymbol{H_2 + 2 * \leftrightarrow 2H - *}$ (3.2)

Heyrovsky: $\boldsymbol{H_2 + OH^- + * \leftrightarrow H - * + H_2O + e^-}$ (3.3)

Volmer: $\boldsymbol{H - * + OH^- \leftrightarrow * + H_2O + e^-}$ (3.4)

One supposition behind the sluggish kinetics of hydrogen reactions in alkaline can be described by the Hydrogen Binding Energy (HBE) Theory, popularized by Sheng et al.[28, 32] The binding energy of hydrogen increases with pH. This increase is apparent when comparing the E_{peak} of the hydrogen underpotential deposition (H_{UPD}) region in

cyclic voltammograms in acid and base environments[30, 32,]. The E_{peak} shifts to higher potentials indicating the increased binding energy. This increased binding energy raises the energy barrier necessary to move through the Volmer step of desorbing H^+ in the HOR and adsorbing H_2O in the HER[23]. The HER is also impacted in high pH through an increase in hydrophobicity of Pt in the catalyst layer at low potentials, leading to a 0.13 eV increase in HBE[111].

Intrinsically, the Volmer step is limited by the utilization of active catalytic sites. Thus, the tunability of a catalyst's physical properties (e.g. crystallite and particle size, microstrain, and particle distribution) become links to enhancing HOR/HER kinetics. Electrocatalysts were previously synthesized, employing a variant CVD process that results in a highly dispersed catalyst on various supports[49, 93-98]. In this process, a low-cost temperature-controlled vacuum oven is utilized to allow for lower decomposition temperatures of metal-organic salt CVD precursors. The process involves mechanically mixing an electronically conductive support with a chosen metal acetylacetoacetates ($M(acac)_x$) $[M^{+x}(C_5H_7O_4)_x]$ salt precursor. These precursors were selected because of their low decomposition temperatures and minimal oxidation of the metal at low-temperature ramp rates. The precursor is partially sublimed at low pressure and elevated temperature, and the metal is deposited on the support.

In this contribution, we investigate the HOR/HER activities on platinum-based electrocatalyst, synthesized using the aforementioned modified CVD process, as a function of varying the reaction temperature and pressure. Furthermore, we explain the impact that these parameters have on the deposition process to better understand its tuning capabilities. Studies on the effect of particle size and its impact on electrocatalysts'

activity have been conducted extensively in acidic environments[112-114]. To our knowledge, this is the first time a study of this sort has been conducted for Pt-based electrocatalysts in alkaline media.

Experimental

Nanoparticle Synthesis. All catalysts were synthesized using a single-step chemical vapor deposition process using Vulcan Carbon XC-72R supports (~70 wt%) and an acetylacetonate precursor in a similar manner previously published. A powder of Platinum (II)(2,4)-pentanedionate [$Pt(acac)_2$] (Alfa Aesar) precursor was mixed with the Vulcan XC-72R (Cabot) carbon support in a glass vial to achieve the appropriate final metal loading of 30 wt% Pt. The vials were then placed into a vacuum oven along with a separate vial of deionized water (Milli-Q, Millpore). The oven was then purged with ultra-high purity (UHP) N_2. The oven was then placed at various parametric combinations of the temperatures (T) and pressures (P) shown in Table 3.1. During the deposition process, the liquid water is vaporized, the metal-organic salt is partially sublimed, and the metal is deposited onto the support, resulting in highly dispersed metallic nanoparticles decorated on the carbon support. After 15 hours, the vacuum oven was evacuated, purged again with UHP N_2, and cooled to room temperature. A mass balance was used to determine the metal content of each catalyst post-deposition.

Spectroscopy/ Microscopy. The various 30% Pt/ XC-72 catalysts were analyzed using x-ray diffraction (XRD) and scanning electron microscopy (SEM). XRD patterns were obtained using a Siemens D5000 diffractometer using Cu radiation (λ=0.154184 nm, 30 kV, 40 mA, 0.05^o step, 1.0 ^{o}*min^{-1}) in a Bragg-Brentano geometry. Aliquots of

catalysts suspended in isopropyl alcohol (IPA) were applied to a zero-background quartz sample holder. The IPA was evaporated before measurements under air and ambient temperatures. Peak width analysis was performed using Igor Pro using a Voigt wave fitting function. SEM micrographs were obtained using a Hitachi FE-SEM S-5200 SEM with an accelerating voltage of 10.0 kV. Images were taken of Low, Mid, and High T and P samples. Small aliquots of these catalysts were suspended in acetone and deposited on an aluminum sample holder.

Electrochemical Characterization. High, mid, and low T and P electrocatalysts were characterized at room temperature in a Teflon three-electrode electrochemical cell (Pine) with a reversible hydrogen reference electrode (eDAQ), Platinum mesh counter electrode. Electrodes were made by depositing 8 µl of well-dispersed catalysts inks comprising 5 mg of catalysts, four drops of DI water, and 1.0 g of IPA onto rotating glassy carbon electrodes (Pine, A=0.1963 cm^2) until dry. Electrode Loadings were measured using XRF (Thermo Scientific ARL Quant' x EDXRF Analyzer) referenced against a ≤5% error standard. An SP-50 potentiostat (BioLogic) was used throughout the electrochemical characterization process. Electrodes were stabilized using cyclic voltammetry (CV) from 0.01- 1.0 V versus RHE in a 1.0 M solution of potassium hydroxide. Polarization curves were then measured from -0.25- 0.25 V versus RHE at 900 RPM in the positive direction. Potential electrochemical impedance spectroscopy (PEIS) spectra were collected from 1 kHz to 1 Hz at -0.1, 0.0, and 0.1 V, with a 10 mV sinusoidal amplitude modulation. The intercept of the spectrum along the real axis at high frequencies was taken as the ohmic resistance of the electrolyte to produce iR-free plots.

Table 3.1: Synthesis parameters for each sample synthesized at low, mid, and high T and P, the sample parameters are indicated below.

Parameters		Temperature (°C)				
		185	200	210	220	235
Pressure (kPa)	38.50	--	--	--	--	High T and P
	28.37	--	--	Mid T and P	--	--
	18.24	Low T and P	--	--	--	--

Electrochemical active surface area (ECSA) measurements were taken from the H_{UPD} region in a 0.1 M solution of perchloric acid at a rotation of 900 RPM and a scan rate of 100 $mV*s^{-1}$.

Results and Discussion

The SEM images were taken of the samples at the highlighted temperatures and pressures mentioned in Table 3.1. The micrographs in Figure 3.1 indicate that the Pt nanoparticles are well dispersed on the carbon support. As the temperature and pressure were increased, we observe an increase in agglomerates. In Figure 3.1A, we see distinct nanoparticles, even when they are near each other. This indicates that the nanoparticles have not begun to coalesce to form agglomerates. As we increase our temperature and pressures in our mid T and P sample, the particles are still well dispersed with slight agglomeration. However, in our high T and P sample, we can identify multiple agglomerates ranging from 15-30 nm in diameter in high concentrations. This increase in agglomeration may be due to 2D Oswald ripening and/or coalescence facilitated by the elevated temperatures and pressures[109]. Due to increased energetics of the nanoparticles at higher temperatures, their ability to migrate on the carbon support surface due to the weak Van Der Walls interaction between the carbon and the Pt increases. This phenomenon also implies a secondary rate law for the PMCVD process associated with the growth of these nanoparticles, further adding to our understating of the PMCVD mechanism proposed in the previous Chapter. Additionally, these agglomerates will, in turn, affect the overall active electrochemical surface area.

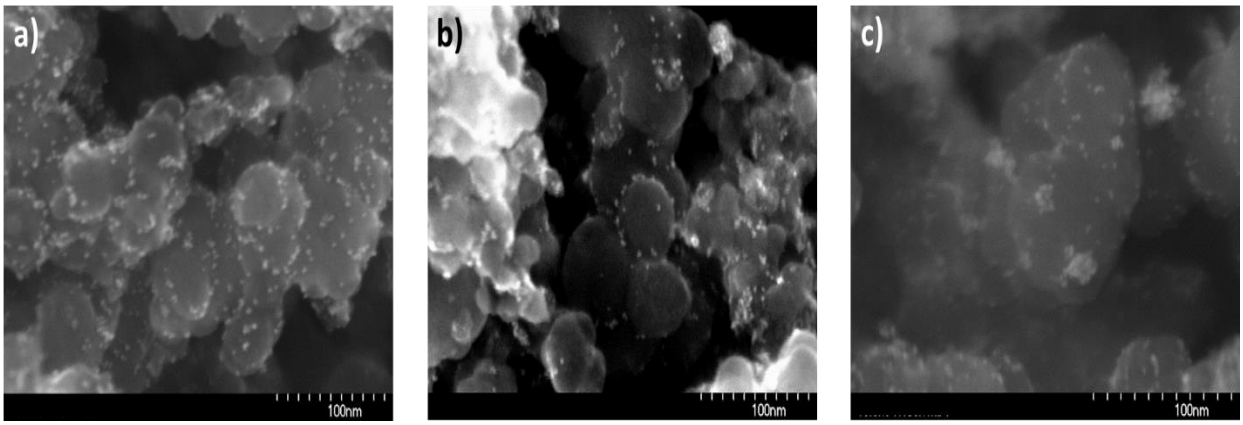

Figure 3.1: SEM micrographs of as-synthesized samples at temperatures and pressures of (a) 185 ^{o}C and 18.24 kPa (low T and P), (b) 210 ^{o}C and 28.37 kPa (mid T and P), and (c) 235 ^{o}C and 38.50 kPa (high T and P). The particle agglomeration increases with temperature and pressure.

In Figure 3.2, we observe the diffraction profiles for each sample, where the phase is identified to be metallic Pt supported on the carbon support, verified through XRD analysis. The prominent peak is from the interaction of X-ray with the Pt (111) facet. Based on our results from previous studies, we can assume that the $Pt(acac)_2$ precursor is fully decomposed, resulting in the reduction of the metal and subsequently the deposition of the Pt nanoparticles.

The utilization of Williamson-Hall (W-H) plots allows us to further analyze our diffraction results to understand better each of our samples' physical properties, e.g., crystallite size and microstrain. Peak broadening is induced when the crystallites in a sample are smaller than 120 nm or when these crystallites are strained[115-116]. Mathematically we can associate the broadening effect of crystallite size (β_L) and strain (β_ε) through Equation 3.5 and 3.6, respectively.

$$\boldsymbol{\beta_L = \frac{0.9 * \lambda}{L * \cos\theta}} \qquad (3.5)$$

$$\boldsymbol{\beta_\varepsilon = 4\varepsilon \tan\theta} \qquad (3.6)$$

Equation 3.5 is known as the Scherrer equation; λ is the characteristic wavelength of the diffractometer source, L is the crystallite size, and q is the Bragg-angle of diffraction. In Equation 3.6 ε is the crystallite microstrain. The sum of our β values represents the full width at half maximum (FWHM) of the diffraction profile peaks. Therefore, β_L and β_ε both contribute to the total breadth of the resultant diffraction peaks.

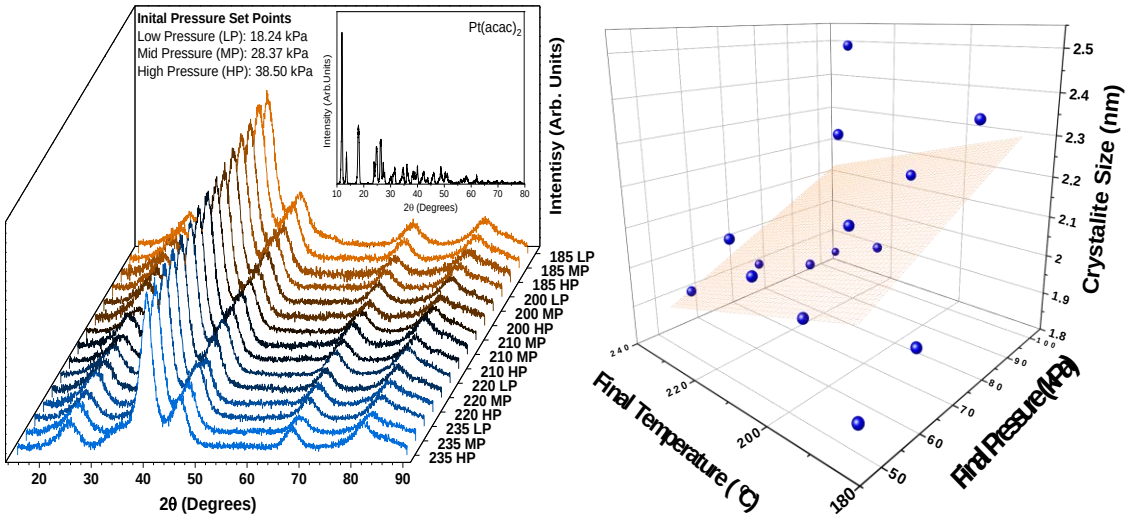

Figure 3.2: (Left) Cu K_α X-ray diffraction patterns of Pt/ XC-72R synthesized catalysts via CVD as well as $Pt(acac)_2$ (inset). Patterns are labeled: Temp. XP, where the final temperature is reported, and the initial pressures (XP) are denoted by an LP, MP, and HP for low mid and high pressure. (Right) Crystallite size distribution as a function of final oven pressure and temperature.

Furthermore, we can combine these equations to form the Williamson-Hall equation shown in Equation 3.8.

$$\boldsymbol{\beta \cos(\theta)_{hkl} = 4\,\varepsilon \sin(\theta) + \frac{0.9 * \lambda}{L}} \qquad (3.8)$$

Because this equation is in y-intercept form, we can calculate the microstrain directly from the slope, where a negative slope implies relative compression of the crystallites and a positive slope the converse. In addition, we can also measure the crystallite size by extrapolating the y-intercept from a linear correlation fit to a βcos(θ) vs. 4sin(θ) scatter plot, otherwise known as a Williamson-Hall plot. Therefore, we can quantify the effects varying the temperature and pressure have on the crystallite size and microstrain in our samples by comparing respective W-H plots.

In figures 3a-e, we show W-H plots at the specific reaction temperatures, noted in the top right corner of the subfigures, as a function of pressures. Similarly, in figures f-h, we compare the samples synthesized at a particular pressure at various temperatures. Finally, in figure I, we compare the W-H plots of the three samples synthesized at low, mid, and high temperatures and pressures.

In looking at our first-mentioned data set, Figure 3a-e, we find that the averaged value of the slopes decreases with an increase in the temperature, indicating the compression of the crystallites in our samples is tied to the reaction temperature. More specifically, we see that at low pressures, the crystallites are always compressed regardless of the temperature. However, at mid and high pressures, there are variations in the microstrain.

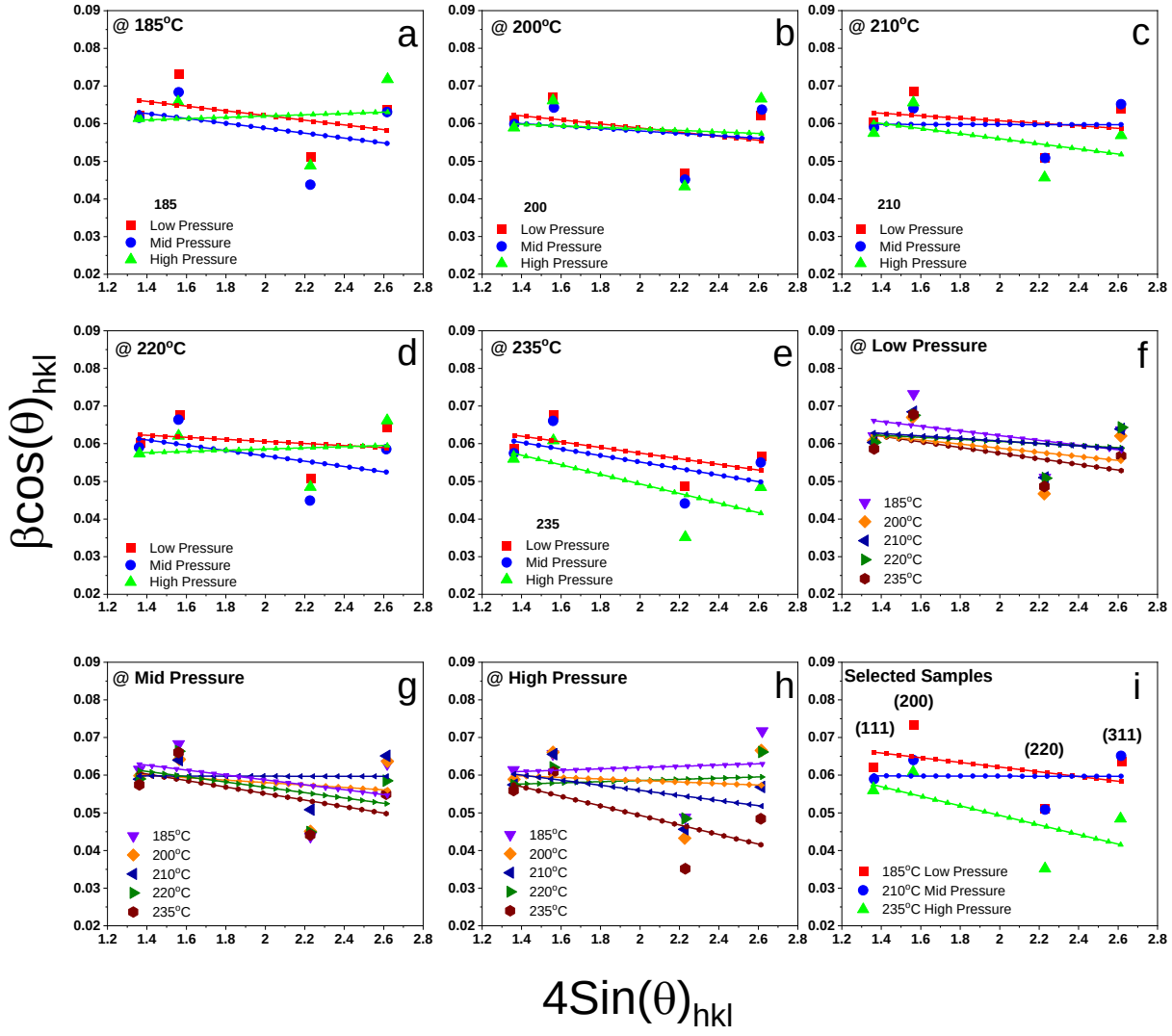

Figure 3.3: Williamson-Hall Plots developed from Cu K_α X-ray diffraction patterns. (a-e) Initial pressure dependence at constant temperatures (displayed in the top left). (f-h) Temperature dependence at constant initial pressures. (i) W-H comparison of low T and P, mid T and P, and high T and P samples. In each plot, the slope represents the microstrain, and the y-intercept is the crystallite size for each sample.

This finding is readily observed in Figure 3.3f-h. Here we identify that the deposited nanoparticles crystallite size and microstrain are sensitive to the reaction pressure. The microstrain we determine is relative with respect to the variances measured in the sample set. The apparent slopes only provide a way for us to compare the impacts of T and P on the crystallite size of each sample when compared to each other. We can see this trend more readily in Figure 3.2 (right), comparing the final temperature and pressures to our crystallite size. Here, the surface fit slope is more affected by changes in pressure and less so with temperature variations. The measured temperature dependence on crystallite size, although not shown graphically, has a parabolic behavior with respect to crystallite size. This is shown in Table A3.1, where the calculated microstructures for all samples in this study are tabulated. The largest average crystallites are found at moderate temperatures and smaller crystallites at our extreme temperatures (185 and 230 ^{o}C). In Figure 3.3i, we compare samples synthesized at low, mid, and high temperatures and pressures. As noted, we observe smaller crystallite sizes at the low and high temperatures and pressures than at the mid parameters. Moreover, the compressive microstrain on these particles at high and low T and P is more significant than the mid T and P sample. The microstrain measured for the Mid T and P sample is negligible when compared to the Low and High T and P samples while its crystallite size is roughly 80% larger.

This indicates the possibility of a critical crystallite size that is temperature-dependent. At higher temperatures, the decomposition of the metal-organic salt precursor occurs more rapidly, leading to a faster increase in Pt concentrations, allowing faster growth of the crystallites. Once this critical size is reached, factors leading to

agglomeration are introduced, thus resulting in the increased agglomeration seen in the high T and P sample. Conversely, at lower temperatures, the precursor decomposes slower, allowing more time for the crystals to grow until they reach their critical size. In the low T and P sample, the rate constants for nucleation and growth are assumed to be smaller than at higher T and P, thus the minimal impacts of coalescence and the result of small nanoparticles. A combination of these two postulates would lead to an increase in crystallite size at moderate temperatures and pressures, aligning with our findings.

The electrochemical characterization of the three samples synthesized at low, mid, and high temperatures and pressures provides information on how the variation in physical properties of the nanoparticles deposited via the modified CVD process affects their catalytic activity for the hydrogen reactions in alkaline media. As mentioned previously, one of the primary descriptors for the sluggish kinetics of the hydrogen reactions in alkaline was that the hydrogen binding energy increases with an increase in pH. A relatively easy way to look at the HBE is by measuring the peak position of the underpotential deposition region of hydrogen (H_{upd}), where a lower peak position indicates a lower HBE. Utilizing this method, we assess the low T and P sample to have the lowest HBE, whereas our Mid and High samples are slightly increased; this is indicated by the vertical bars found at the top of Figure 3.4a. Additionally, we noticed a change in electrochemical surface area (ECSA) in these three samples as a function of T and P.

The ECSAs were calculated for the three extensively studies samples by integrating the H_{upd} region produced through cyclic voltammetry conducted in 0.1 M $HClO_4$. The values calculated through Equation 3.9 are shown in the inset of Figure 3.4b.

$$\boldsymbol{ECSA_{Pt}(m^2 g_{Pt}^{-1}) = \frac{Q_{H_{upd}}(C)}{210 \mu C cm_{Pt}^{-2} L_{Pt}(mg_{Pt} cm^{-2}) A_{disk}(cm^2)}} \qquad (\mathbf{3.9})$$

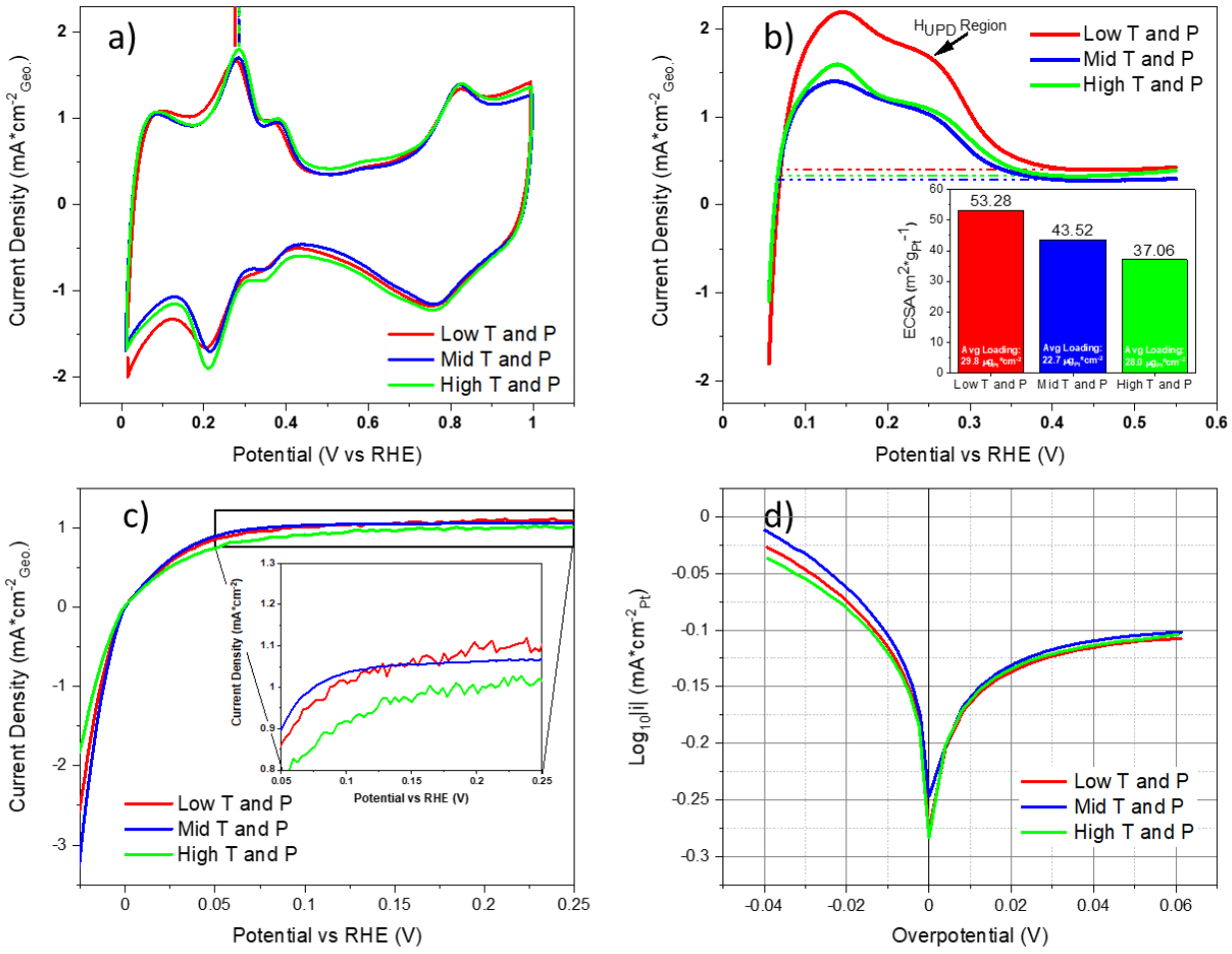

Figure 3.4: Electrochemical characterization of the low T and P (Red), mid T and P (Blue), and high T and P (Green) samples. (a) Cyclic voltammograms (CVs)of each sample in 0.1 M NaOH at a scan rate of 100 $mV*s^{-1}$. (b) CVs conducted in 0.1 M $HClO_4$ at 100 $mV*s^{-1}$, ECSAs were calculated by integrating the area above the dotted lines and are displayed as a bar graph. (c) iR-corrected polarization plots were taken at 2 $mV*s^{-1}$ in 0.1 M NaOH. (d) Tafel plots of each sample.

In this equation, we assume that a monolayer of hydrogen is absorbed onto the Pt nanoparticles. By calculating the charge produced through the reduction of this monolayer, integrating the H_{upd} region, the ECSA is resolved. In Equation 3.9, Q_H is calculated by dividing the integral of the H_{upd} by the scan rate,100 $mV*s^{-1}$; 210 $mC*cm^{-2}$ is the amount of charge needed to reduce a monolayer of protons on a platinum surface, A_{disk} is the geometric area of the electrode, L_{Pt} is the platinum loading on the electrode.

As we increase temperature and pressure, the ECSA decreases from 53.28 (low T and P) to 37.08 (high T and P) m^2*g_{pt}. The lower ECSA found in the high T and P sample is due to the increased agglomeration. As the agglomerates are formed, less Pt is accessible, reducing available sites for the hydrogen reactions[109]. The mid T and P sample exhibited the highest activities for both the HER and HOR, in comparison to the samples synthesized at the extreme conditions by comparing the reaction activities through polarization plots found in Figure 3.4c. More descriptively, we find that our mid-sample reaches a higher limiting current at lower overpotentials for the HOR than the other samples producing 0.026 $mA*cm^{-2}_{Pt}$ at 10 mV vs. RHE and producing a specific current of 0.071 $mA*cm^{-2}_{Pt}$ at -10mV vs. RHE for the HER.

The variations in the measured specific activity for the HOR are small across the electrocatalysts, only varying by 0.001 $mA*cm^{-2}_{Pt}$. However, when we compare the mass activities of these samples, we see the low T and P exhibits the highest HOR activity of 12.67 $A*g_{Pt}^{-1}$. This is partly due to its high ECSA, promoting the procedure of the Volmer step as the concentration of vacant catalytic sites is increased. However, we see a slight decrease in this superior activity for the HOR when comparing activities for the HER. We find that the mid T and P sample has the highest mass activity for the HER producing

30.84 $A*g_{Pt}^{-1}$. The deviation in high activity for the low T and P sample is attributed to both the associated microstrain as well as the associated hydrophobicity of the Pt nanoparticles endured at the necessary low overpotentials for the HER. Additionally, the adsorption of the larger water molecule in H_2O (2.8 Å in diameter) is restricted due to the compressed crystallite[117]. The energetically favorable lattice parameter for Pt which is equal to the average spacing between crystal facets, is 3.92 Å[118]. As such, the unitless microstrain imposed on the low T and P sample of -0.00625 may be sufficient to prohibit water adsorption, lowering its catalytic activity compared to the less strained mid T and P catalyst.

The exchange current densities for each electrocatalysts were extrapolated from the Tafel plots shown in Figure 3.4d. Here the mid T and P sample shows its superiority in HOR/HER kinetics in comparison to the other samples. The measured exchange current density for the mid T and P samples was 0.77 $mA*cm_{Pt}^{-2}$, which is higher than previously published exchange current densities of 0.57- 0.69 $mA*cm_{Pt}^{-2}$ for commercially available carbon-supported Pt electrocatalysts in alkaline media [24, 25, 32]. HOR and HER activities for each sample are shown in Table 3.2. The Tafel plots shown have an asymmetrical behavior; this is primarily due to the inability to reach a steady-state for the hydrogen reactions as the electrode continuously changes with current and time in unbuffered solutions[119]. These changes can include the increased repulsion of water from the surface of the electrode at negative potentials, leading to variations in adsorption of the reactants across the measured potential region[111, 119].

Table 3.2: Hydrogen reaction activities of low, mid, and high T and P samples. Exchange current densities were calculated from extrapolation of the linear Tafel region to 0 V overpotential. Mass and specific activates were measured through linear interpolation of the polarization curves at ±10 mV vs RHE.

SAMPLE	Loading ($mg_{pt}*cm^{-2}$)	Exchange Current	Activities			
		i_o ($mA*cm^{-2}_{Pt}$)	$i_{\eta(10\ mV)}$ ($mA*cm^{-2}_{Pt}$)	$i_{\eta(10\ mV)}$ ($A*g_{Pt}^{-1}$)	$i_{\eta(-10\ mV)}$ ($mA*cm^{-2}_{Pt}$)	$i_{\eta(-10\ mV)}$ ($A*g_{Pt}^{-1}$)
Low T and P	0.022	0.75	0.024	12.67	-0.055	-29.45
Mid T and P	0.025	0.77	0.026	11.4	-0.071	-30.84
High T and P	0.027	0.70	0.025	9.21	-0.048	-17.83

Both HOR and HER are governed by surface coverage, θ, where the associated Tafel slopes will vary as a function of θ, this giving rise to the asymmetric Tafel plots observed throughout the study [120].

From our initial CVs, we expected the Low sample to exhibit the highest activities due to its low HBE. However, in studying the data collectively, we can rationalize the increased kinetics of the mid sample is due to the relaxed microstrain on the crystallite compared to the other samples. We deduce this result from Figure 3.4d where the HER branch, where overpotentials are negative, trends based on our samples' microstrain. The more negative the microstrain, the more compressed the atoms are in the crystallite, inhibiting the necessary H_2O adsorption step for the HER to initialize via a Volmer limited process. The High T and P sample exhibited the most negative microstrain in comparison resulting in its lower activities.

As for the HOR branch, where overpotentials are positive, we are limited by the rate at which we can desorb H^+ from the catalytic surface, assuming a Volmer rate-determining step. In that case, the current is limited by the activity of the catalyst. Larger crystallites and, in turn, nanoparticles tend to exhibit higher specific activities and lower mass activities in both acid and base, although they have lower ECSA[109, 112, 114]. Thus, the activity trend shown for the HOR follows the Williamson-Hall plots with respect to the crystallite size. The smallest crystallites are found in the low T and P sample, which in turn exhibited lower specific catalytic activities, whereas the mid sample, having larger crystallites, increasing its surface energies and, in turn, catalytic currents.

Conclusion

Our findings suggest that both HOR and HER in alkaline media can be tuned by altering the active catalytic material's physical properties of crystallite size and microstrain. The modified chemical vapor deposition method used to synthesize the electrocatalyst studied in this work produces highly dispersed nanoparticles on the carbon support. We observed an increase in agglomeration as we increase our temperature and pressure due to 2D Oswald ripening and coalescence driven by the increased temperature. Furthermore, through W-H analysis, we showed that the CVD method provides a way to tune the crystallites' microstructure characteristics. Although we did not observe a broad distribution of our crystallite size or microstrain through the XRD analysis, our study shows that these small changes impact the electrocatalyst's activity for the probed hydrogen reactions. Our electrochemical characterization elucidates that relaxed microstrain and large crystallites can lead to increased activities for the hydrogen reactions in alkaline. Although the exchange current densities of the investigated electrocatalysts are relatively similar, we observed fluctuations in the specific activities for the analyzed samples for both HER and HER at low (±10 mV) overpotentials attributed to the variations in crystal properties. These results show promise that this CVD method can be used to further increase activities for other heterogeneous reactions by manipulating the electrocatalysts microstructure, ultimately enhancing performance in electrochemical devices.

CHAPTER IV

SYNTHESIS AND CHARACTERIZATION OF BIMETALLIC PLATINUM-RUTHENIUM AND PLATINUM-NICKEL ELECTROCATALYSTS FOR HYDROGEN REACTIONS IN ALKALINE MEDIA

Abstract

The development of highly active electrocatalysts for AEM devices is paramount to these devices' commercialization. Bimetallic Platinum-based catalysts have sown the highest electrochemical activity for the sluggish hydrogen reactions. These catalysts are typically synthesized in a solution using reduction or precipitation methods, which often require several steps to produce an active catalyst. This study used a modified chemical vapor deposition process to synthesize bimetallic PtNi and PtRu electrocatalysts. These electrocatalysts were characterized through diffraction to show the modified deposition method's ability to alloy these metals and electrochemically to show these metals' activities for the hydrogen oxidation and evolution reactions in alkaline media as a function of the oxyphilic metals loading. In both cases, the measured activities showed an increase compared to monometallic Pt, where the ascribed trends were more closely related to the metal additive's nobility.

Introduction

Lowering the system cost while increasing performance and durability is one leading line of effort in developing proton exchange membrane (PEM) fuel cells. An essential fraction of the cost is closely associated with the high cost of the electrode material needed to catalyze the hydrogen oxidation reaction (HOR) and oxygen reduction reaction (ORR) on the anodes and cathodes, respectfully. In these acidic PEMFCs, the ORR is the slower reaction of the two, requiring more catalysts to increase efficiency. In terms of monometallic electrocatalysts, platinum supported on carbon (Pt/C) has

exhibited the highest activities for both reactions; however, its high cost has driven research efforts towards lowering the overall Pt loadings[14,121].

These efforts center around the study of Pt-M alloys[75, 122-126]. Currently, the state-of-the-art bimetallic electrocatalysts for PEMFCs are variations of PtCo alloys supported on carbon[48, 124, 125, 127]. These alloys have shown an increase in activity and stability over conventional Pt catalysts while lowering the electrode's overall Pt. In alkaline environments, oxyphilic PGM-free electrodes have shown high activities comparable to platinum, ultimately eliminating the need for Pt on the cathode[18-21]. However, in alkaline media, the hydrogen reactions, namely the HOR and hydrogen evolution reaction (HER), are two orders of magnitude slower[23-26].

Several rationales have been developed to explain the sluggish hydrogen reaction in basic environments. The most accepted is the hydrogen binding energy (HBE) theory. Previous studies have shown that through DFT calculations coupled with experimentation, the HBE increases as a function of pH. Monometallic Pt has shown the best relationship between activities relative to the HBE, making them the ideal hydrogen catalyst in alkaline conditions. This over-binding of hydrogen lowers the rate of H^+ desorption in each of the accepted elementary steps for HOR/HER. These steps are known as the Tafel reaction, which is primarily ad/desorption driven, and the Heyrovsky and Volmer reactions are electron-transfer steps. It is accepted that the vomer step is the rds for the HOR/HER reactions through Tafel slope analysis. Monometallic Pt has shown the best relationship between activities relative to the HBE making the metal the ideal hydrogen catalyst in base.

Another theory of merit is known as the bifunctional mechanism theory. This theory suggests that the alloying of an oxyphilic metal with Pt aids the HOR by promoting H^+ desorption and the HER by promoting water dissociation[35]. In each case, this lowers the Volmer step's energy barrier. H+ and OH- ions must compete for the limited reactant sites in monometallic systems. Mukherjee et al. suggest more specifically that the addition of an oxyphilic metal provides a secondary site for either H^+ or OH^- adsorption based on the nobility of the metal used[37, 128]. In the case of noble metals such as Ru, the formation of a quasi-adsorbed hydroxide species is enabled[128]. Similarly, when a transition metal is alloyed to Pt, a hydroxide species is fully adsorbed through a pacifying oxide/hydroxide layer forms on the PGM-free metal surface at high pH[128].

The use of PtNi/C and PtRu/C electrocatalysts has greatly increased the performance of alkaline exchange membrane fuel cells (AEMFCs) when used as an anode electrode[49, 125-127, 129]. These electrocatalysts are typically developed through solution-based synthesis methods, requiring post-treatment to reduce the metal particles fully[129-131]. A more facile and controlled process for developing these electrocatalysts can aid in the overall system cost, leading to the potential commercialization of AEM devices. In this study, we synthesize PtNi/C and PtRu/C electrocatalysts with varied mass ratios via a modified CVD process that has been shown to produce reduced metallic nanoparticles in a single-step process[49, 93-98]. We characterize these electrocatalysts' electrochemical activities for the hydrogen reaction in alkaline to provide evidence of the synthesis method's versatility.

Experimental

Electrocatalyst Synthesis. All catalysts were synthesized using a single-vat modified chemical vapor deposition process. Vulcan Carbon XC-72R (Cabot) was used as the support. $Pt_{(1-x)}Ni_x$ and $Pt_{(1-x)}Ru_x$ and samples were developed to have a metal weight percent (wt.%) of 30% supported on Vulcan XC-72R carbon (70 wt.%). Of that 30% metal, samples were prepared to contain 10, 20, and 30 wt.% Ni or Ru balanced with Pt. For the synthesis method, metal-organic salt precursors of Platinum(II) Acetylacetonate; $Pt(acac)_2$, Nickel(II) Acetylacetonate; $Ni(acac)_2$, Ruthenium(III) Acetylacetonate; $Ru(acac)_3$ (Alfa Aesar) were mechanically mixed with the carbon support in glass vials. The vials were then placed into a vacuum oven along with a separate vial of deionized water (Milli-Q, Millpore). The oven was then sealed and purged with ultra-high purity (UHP) N_2, then set to 240 ^oC and 260 ^oC for the $Pt_{(1-x)}Ni_x$ and $Pt_{(1-x)}Ru_x$ samples, respectively. The oven was evacuated to 17.65 kPa for all sample sets. More details about the deposition process have been previously described in earlier chapters. A mass balance was used to determine each catalyst post-deposition's metal content. One (1) hour-long heat-treatments were conducted under forming gas (5% H_2 Bal. Ar) at the sample sets' reaction temperatures to ensure the deposited metals were fully reduced. Although not necessary, this step was used to mainly ensure the Ni particles were fully reduced as preliminary studies, Figure A4.1, showed the evolution of oxidized Ni nanoparticles on various carbon supports produced through the modified CVD process.

Materials Characterization. The catalysts were analyzed using x-ray diffraction (XRD) and scanning electron microscopy (SEM). XRD patterns were obtained using a Siemens D5000 diffractometer using Cu radiation (l=0.154184 nm, 30 kV accelerating voltage, 40 mA accelerating current) in a Bragg-Brentano geometry. Aliquots of catalysts suspended in isopropyl alcohol (IPA) were applied to a zero-background quartz sample holder. The samples were left to dry in an ambient environment to ensure the IPA was evaporated before measurements. Peak width analysis of the diffraction profiles was performed using OriginPro peak analysis software using a Gaussian fitting function. SEM micrographs were obtained using a Hitachi FE-SEM S-5200 SEM with an accelerating voltage of 10.0 kV using a mixed backscatter and secondary electron detector to show z-contrast and morphology of the samples. Small aliquots of these catalysts were suspended in acetone and deposited on an aluminum sample holder. Metal content ratios were measured using x-ray fluorescence (XRF) using a Thermo Scientific ARL Quant'x EDXRF Analyzer. The samples were referenced against standards with ≤5% error.

Electrochemical Characterization. Electrocatalysts were characterized at room temperature in a three-electrode, Teflon electrochemical cell (Pine) with a reversible hydrogen reference electrode (eDAQ) and a platinum mesh counter electrode. Electrodes were made by depositing 8 ml of well-dispersed catalysts inks comprising 5 mg of catalysts, four drops of DI water, and 1.0 g of IPA onto a glassy carbon electrode (Pine, A=0.1963 cm^2) rotating at 500 RPM and left to dry in an ambient environment. Total electrode metal loadings were measured using XRF using a Thermo Scientific ARL Quant'x EDXRF Analyzer. Profiles were calibrated to a standard with <5% error.

Electrodes were stabilized using cyclic voltammetry (CV), scanning from 0.01- 1.0 V versus RHE in a 0.1 M solution of potassium hydroxide. Positive-going polarization curves were then measured from -0.25- 0.25 V versus RHE at 900 RPM. Potential electrochemical impedance spectroscopy (PEIS) spectra were collected from 1 kHz to 1 Hz at -0.1, 0.0, and 0.1 V with a 10mV sine perturbation amplitude. The measured high-frequency intercepts were taken as the electrolyte's ohmic resistance to produce iR-free plots.

Results and Discussion

Material characterization began with microscopy of the $Pt_{(1-x)}Ru_x$/ XC-72 electrocatalysts. We analyzed the particle size distribution and particle distribution found in each sample using scanning electron microscopy. The size of the deposited $Pt_{(1-x)}Ru_x$ nanoparticles is 4 nm, averaged over each sample set, calculated through manually measuring the diameters of over 100 particles through ImageJ. The micrographs in Figure 4.1 show the high dispersion of the bimetallic nanoparticles achieved through the modified CVD process. We do observe evidence of agglomeration in each sample, with more agglomerates observed in the $Pt_{0.7}Ru_{0.3}$/ XC-72 sample. This high nanoparticle density allows us to assume a homogeneous distribution of metallic nanoparticles decorated on the entire carbon support. Furthermore, due to the carbon support morphology, the nanoparticles are decorated on the carbon support surface. We observe that the nanoparticles deposit on the carbon support folds where the carbon particles join as mentioned in previous studies Found in chapters 2 and 3. Images of $Pt_{(1-x)}Ni_x$ samples were not taken.

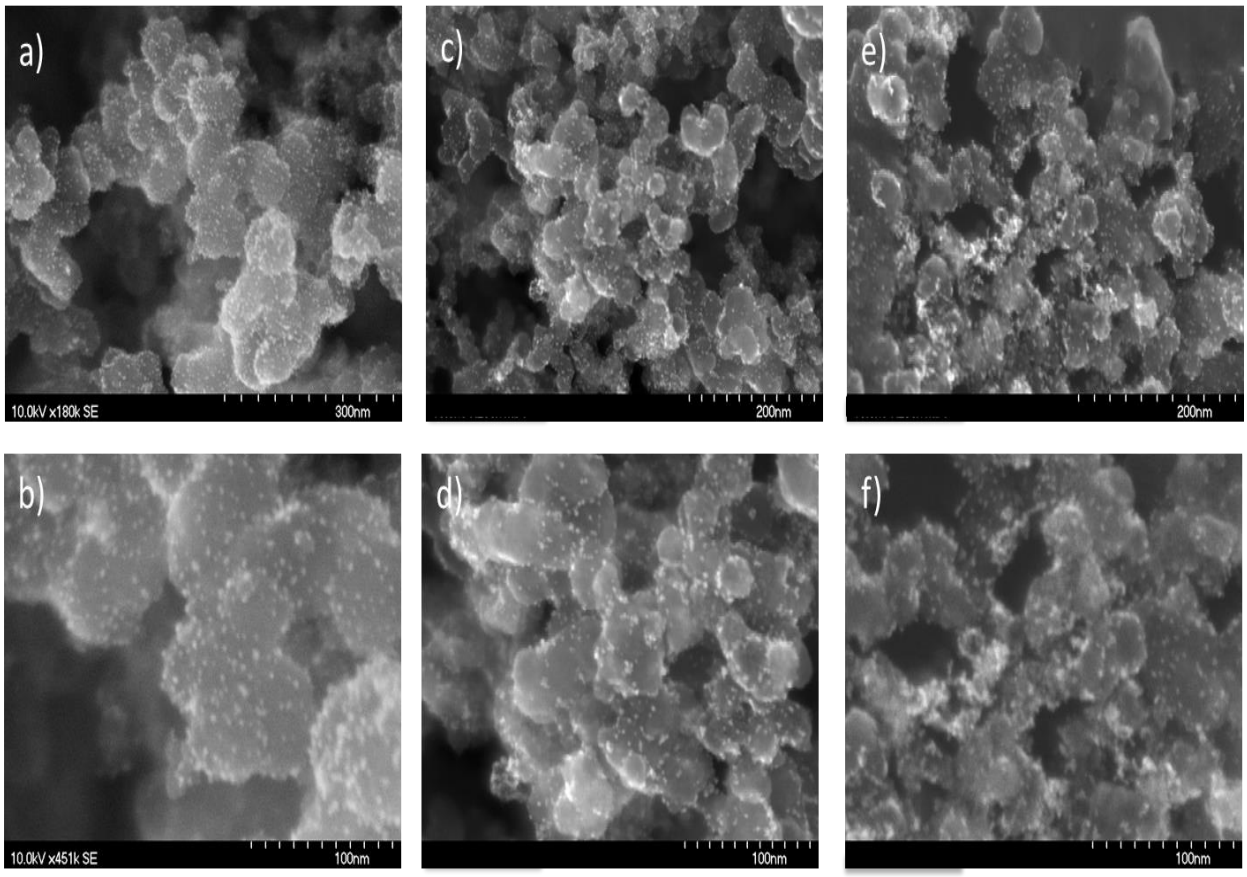

Figure 4.1: SEM micrographs of CVD synthesized samples with weight fractions of a,b) $Pt_{0.9}Ru_{0.1}$/ XC-72; c,d) $Pt_{0.8}Ru_{0.2}$/ XC-72; e,f) $Pt_{0.7}Ru_{0.3}$/ XC-72. The sale bar on the images in the top row are 300nm and the bottom, 100 nm, edge to edge.

X-ray diffraction was used to determine the phases of the deposited nanoparticles. Figure 4.2 shows the diffraction profiles for each of the prepared samples. At the bottom of the image, we have included the reference profiles for the relative scan range of 15-75° 2θ. Each sample shows a peak at ~25° 2θ, indicating the amorphous XC-72 carbon supports (002) crystal facet peak. Furthermore, in the $Pt_{(1-x)}Ni_x$ / XC-72 samples, we see the increased Ni content through the shift in the peak position of the Pt (111) facet to higher °2θ. This shift is attributed to the Pt and Ni's alloying within the sample, leading to smaller lattice parameters. We determined the degree of alloying through Vargard's Law, Equation 4.1, as Pt and Ni both have an FCC crystal structure. Here, a_A and a_B represent the measured lattice parameters for pure Pt (3.192 Å) and Ni (3.524 Å), respectively, x is the mass fraction of Ni in the deposited nanoparticles, and $\boldsymbol{a_{A_{(1-x)}B_x}}$ is the calculated lattice parameter of the mixed metals from XRD.

$$\boldsymbol{a_{A_{(1-x)}B_x} = (1-x)a_A + xa_B} \qquad (\boldsymbol{4.1})$$

However, the PtNi samples show evidence of deposited HCP Ni, highlighted by the asymmetric high-intensity peak found in the $Pt_{0.7}Ni_{0.3}$/XC-72 sample. Due to this evidence, the challenge of delineating the sample's exact phase proportions increases. Superficially, we measured the lattice parameters calculated from each sample's high-intensity peak in a similar fashion done in Chapter 2, and observed a decrease in the lattice parameter as we increased the Ni content. This decrease in lattice parameter provides evidence of alloying in the deposited nanoparticles.

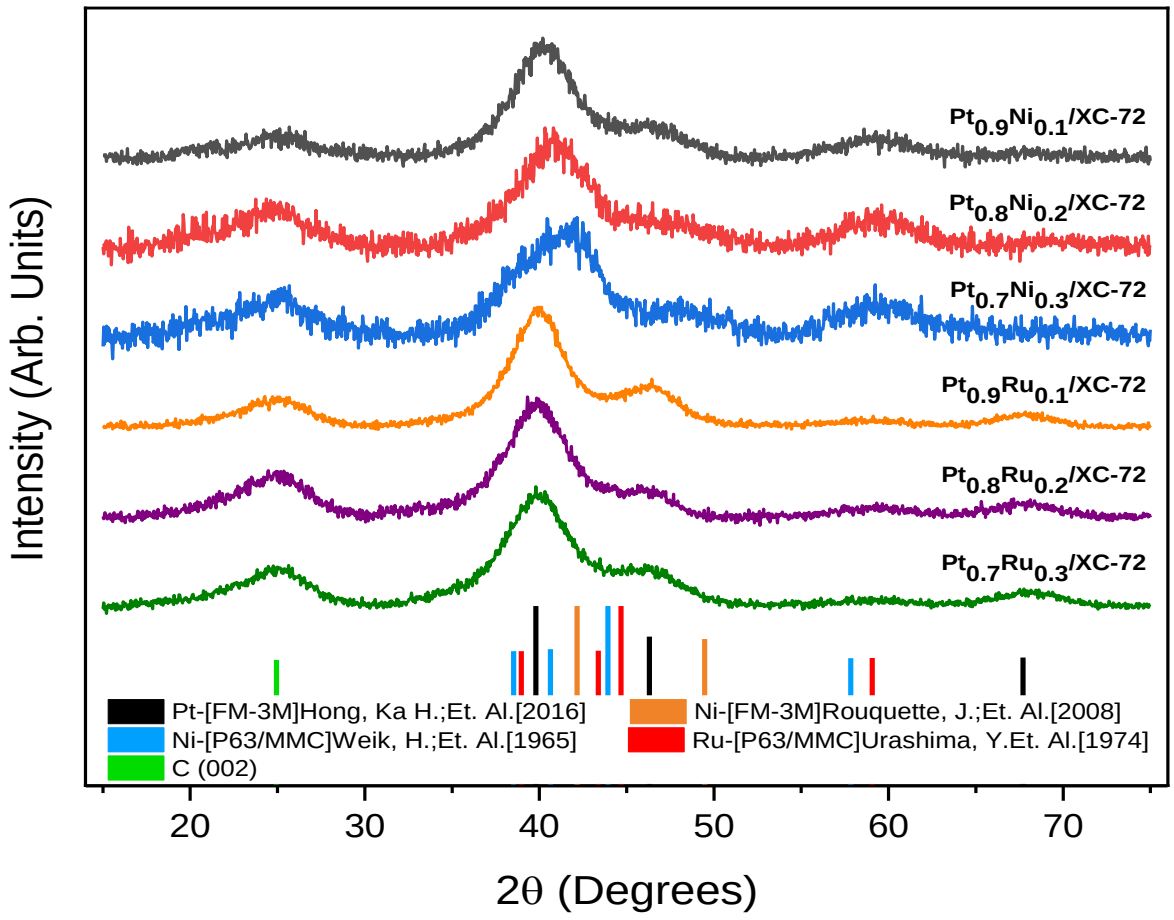

Figure 4.2: Cu K_α X-ray diffraction patterns of $Pt_{(1-x)}Ni_x$ / XC-72 and $Pt_{(1-x)}Ru_x$/ XC-72 catalysts synthesized via CVD. Bragg peaks for Pt, FCC Ni, HCP Ni, Ru, and C are shown at the lower portion of the figure.

.

Similar findings are observed in the $Pt_{(1-x)}Ru_x$/ XC-72 sample. In these diffraction profiles, the lattice parameter decreases from the expected Pt lattice parameter (3.924 Å), with an increase in Ru content. These results indicate partial alloying of the FCC Pt with HCP Ru. Because of the difference in crystal structures, we must use a variant of Vagrad's Law by comparing the similar crystal facets of the (111) in the FCC Pt structure to the (0001) in the HCP Ru[132]. This calculation is achieved through Equation 4.2, where l_m is the measured lattice parameter for the PtRu sample, l_s is the lattice parameter of pure Pt supported on XC-72, k_{Ru} is the lattice dependence constant for Ru to attribute its (0001) facet to the Pt (111) facet, and x is the mass fraction of Ru in the mixed sample.

$$\boldsymbol{l_m = l_s - k_{Ru}x} \qquad (\mathbf{4.2})$$

One outlier regarding the change in lattice parameter was found in the $Pt_{0.8}Ru_{0.2}$/XC-72 sample. We measured an unexpected higher lattice parameter concerning the other Ru-containing samples, indicating less alloying of the Pt and Ru. This result could be due to sample surface displacement. The sample may be misaligned within the focusing circle, resulting in the x-rays not converging at the correct position for the detector, skewing the measured angle of diffraction[115, 116]. This could be resolved by adding a reference material to our electrocatalyst, allowing us to observe any shifts in our peaks due to sampling surface displacement. This process was not conducted due to the small quantity of catalyst synthesized and the need to conduct further analysis of the samples. Additionally, the degree of alloying measured may be accurate. In the modified CVD method, alloying will occur if the Pt and Ru metal-organic salt precursors are in close

proximity to each other prior to the deposition. We can assume some variations in the distribution of these salts as the sample is mechanically mixed. These variations provide the key to enhancing the degree of alloying by mixing the precursors before mixing them with the carbon support. This would help improve the proximity of the salts to one another and potentially improve the amount of alloys produced using the modified deposition method. We show the calculated lattice parameters measured from the high-intensity peak and our calculated alloy percentages through Vegard's Law in Table 2.

We measured the deposited wt% of the various metals in each sample through spot XRF. We see that our measured values are within 90.1 ±5% of our expected values. These wt% were measured against appropriate references that have an error of 5%. The XRF and XRD analysis confirm that our modified vapor deposition process is efficient at depositing the metals used in this study on a carbon support, as long as the reaction conditions are above the vapor conditions for the metal-organic salt precursors. We can compare the relative mass alloyed by comparing the x-value measured through Equations 4.1 and 4.2 to the wt% measured through XRF. Through this comparison, we measure a 74.1% average of Ni alloyed to Pt in the $Pt_{(1-x)}Ni_x$ samples with no trend in % alloyed concerning Ni content. In the $Pt_{(1-x)}Ru_x$ samples, we measured a 23.4% average of Ru alloyed to Pt. Because of the low degrees of alloying in each sample set, even with respect to the 5% error acociated with the XRF results, we assume the residual metal deposits as individual Pt, Ni, or Ru nanoparticles. These comparisons of weight percents allow us to index the various samples to identify the alloying capabilites fo the modified CVD method. Due to the nanoparticle's size, our resolution for diffraction analyis is low, thus we only offer an indexing of the samles to discuss the degree of alloying.

Table 4.2: Lattice parameters of $Pt_{(1-x)}Ni_x$/XC-72 and $Pt_{(1-x)}Ru_x$/XC-72 samples and weight fraction, x, of the non-Pt metal calculated using Vegard's Law and Wt% of the various samples calculated by XRF within a 5% error.

Sample	Pt (111) 2θ	a	Vegard's Law	XRF		
			x	Wt.% Pt	Wt.% Ni	Wt.% Ru
$Pt_{0.9}Ni_{0.1}$/XC-72	40.204	3.88	0.083	87.66	12.34	--
$Pt_{0.8}Ni_{0.2}$/XC-72	40.771	3.83	0.211	75.02	24.98	--
$Pt_{0.7}Ni_{0.3}$/XC-72	41.050	3.81	0.263	62.82	37.18	--
$Pt_{0.9}Ru_{0.1}$/XC-72	39.901	3.911	0.057	88.60	--	11.40
$Pt_{0.8}Ru_{0.2}$/XC-72	39.853	3.916	0.016	76.97	--	23.03
$Pt_{0.7}Ru_{0.3}$/XC-72	39.887	3.913	0.040	69.63	--	30.37

Electrochemical characterization techniques were utilized to determine these electrocatalysts' electrochemical activities for the hydrogen reactions in alkaline. The electrochemical results are shown in Figure 4.3a-d. Figure 4.3a and c depict the initial cyclic voltammograms, and Figure 4.3b and d show the polarization plot and respective Tafel plots utilized to characterize the activates of the $Pt_{(1-x)}Ni_x$ samples and $Pt_{(1-x)}Ru_x$ samples, respectively. In Figure 4.3A, we observe increased oxidation in the anodic scan's higher potential region with the increased amount of Ni in the samples. The scan range was varied to allow for the complete oxidization of the Ni in each sample. The turning voltage for each sample was determined by incrementally increasing the peak voltage until the solvent limit was reached. We also observe a reduction of underpotentially deposited hydrogen relative to the double layer capacitance as the Pt content decreased and the Ni increases.

We compare the $Pt_{(1-x)}Ni_x$/XC-72 electrocatalyst activities through the polarization plots shown in Figure 4.3b. The plot shows a decrease in the HOR/HER activity as we increase the Ni content. Table 4.3 illustrates that at low overpotentials (±10 mV) that the $Pt_{0.9}Ni_{0.1}$/XC-72 sample exhibited the highest specific activity of 0.65 $mA*cm^{-2}_{geo.}$ for the HOR and 1.096 $mA*cm^{-2}_{geo.}$ for the HER. Additionally, through extrapolation of the inserted Tafel plot, we measured the exchange current density of this sample to be 1.09 $mA*cm^{-2}_{geo.}$, which is higher than ~140% of the $Pt_{0.7}Ni_{0.3}$/XC-72. Although studies have shown that the addition of oxyphilic metals will promote increased activities in alkaline media due to the bifunctional mechanism, we find that increasing amount of Ni leads to further oxidation of the metallic catalytic surface, blocking active sites, and ultimately resorting to proposed monometallic phenomena for hydrogen reactions[128].

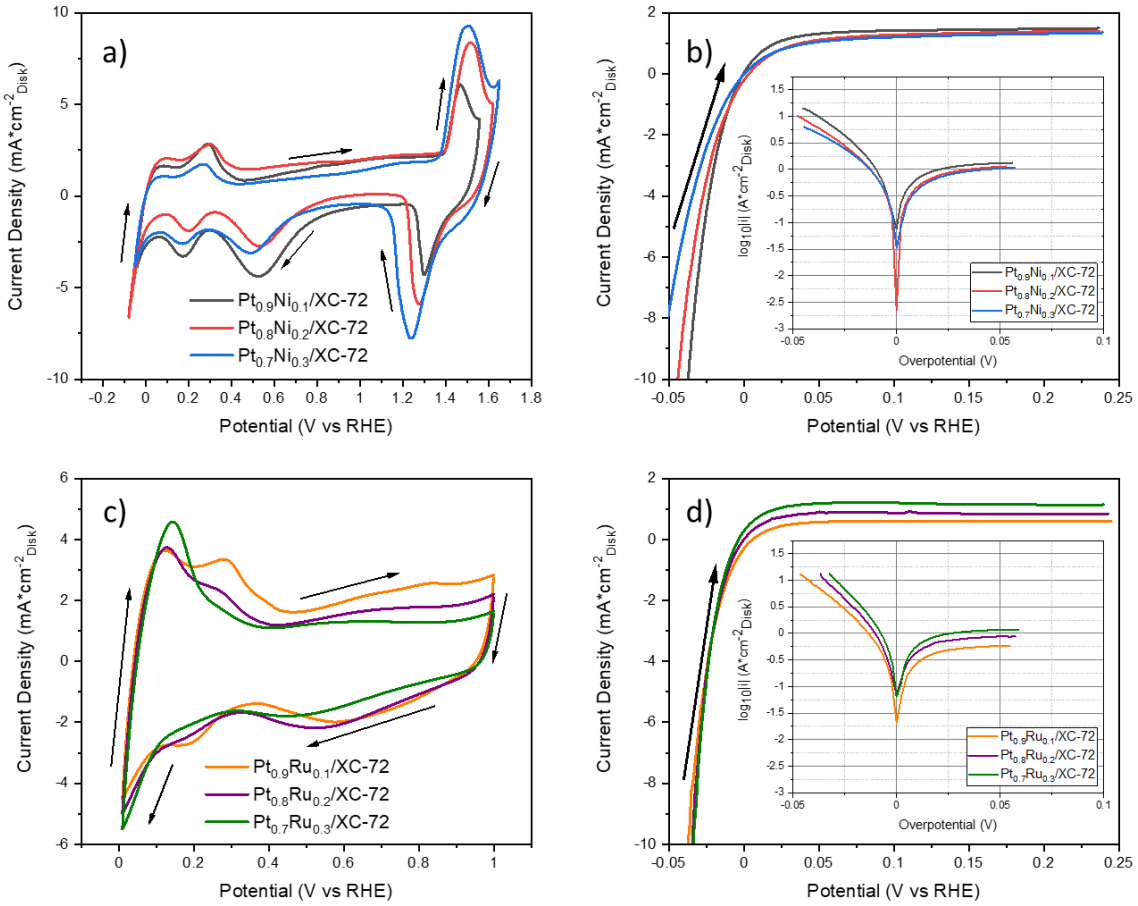

Figure 4.3: Electrochemical characterization of our $Pt_{(1-x)}Ni_x$/XC-72 and $Pt_{(1-x)}Ru_x$/XC-72 samples. (a) Cyclic voltammograms (CVs)of $Pt_{(1-x)}Ni_x$/XC-72 samples in 0.1 M NaOH (pH=13) at a scan rate of 100 $mV*s^{-1}$. (b) iR-corrected polarization plots of $Pt_{(1-x)}Ni_x$/XC-72 samples conducted in 0.1 M NaOH at 2 $mV*s^{-1}$; inset depicts the activities as a Tafel plot. (c) Cyclic voltammograms (CVs)of $Pt_{(1-x)}Ru_x$/XC-72 samples in 0.1 M NaOH at a scan rate of 100 $mV*s^{-1}$. (d) iR-corrected polarization plots of $Pt_{(1-x)}Ru_x$/XC-72 samples conducted in 0.1 M NaOH at 2 $mV*s^{-1}$; inset depicts the activities as a Tafel plot. Currents are all displayed as the measure current density on a glassy carbon electrode (0.1963 cm^2). Arrows are used to indicate the direction of voltage sweeps.

Table 4.3: Electrochemical activities of $Pt_{(1-x)}Ni_x$/XC-72 and $Pt_{(1-x)}Ru_x$/XC-72 samples. The exchange current densities are calculated via Tafel extrapolation. Specific activities are normalized to the geometric surface area of the glassy carbon electrode (0.1963 cm^2).

SAMPLE	Loading $mg_{Metal}*cm^{-2}$	Exchange Current	Activities			
		i_o $mA*cm^{-2}_{geo.}$	$i_{\eta(10\ mV)}$ $mA*cm^{-2}_{geo.}$	$i_{\eta(10\ mV)}$ $A*g_{Metal}^{-1}$	$i_{\eta(-10\ mV)}$ $mA*cm^{-2}_{geo.}$	$i_{\eta(-10\ mV)}$ $A*g_{Metal}^{-1}$
$Pt_{0.9}Ni_{0.1}$	0.025	1.09	0.65	26.0	-1.09578	-43.8312
$Pt_{0.8}Ni_{0.2}$	0.024	0.78	0.34	14.17	-1.08779	-45.3246
$Pt_{0.7}Ni_{0.3}$	0.027	0.76	0.43	15.93	-0.71546	-26.4985
$Pt_{0.9}Ru_{0.1}$	0.024	0.50	0.15	6.25	-1.19105	-49.6271
$Pt_{0.8}Ru_{0.2}$	0.019	0.52	0.45	23.68	-0.94412	-49.6905
$Pt_{0.7}Ru_{0.3}$	0.012	0.81	0.75	62.5	-0.7282	-60.6833

However, in the $Pt_{(1-x)}Ru_x$/XC-72 samples, we measure a continuous increase in activity with the addition of the oxyphilic and noble Ru. In Figure 4.3c, we can see the suppression of the second H_{upd} stripping peak at ~0.25 V vs. RHE, with the increase in Ru content in the samples. We also see an increase in the redox peak found at ~0.1 V vs. RHE with the increase in Ru content. There are several schools of thought as to why this peak grows with increased Ru. One rationale is due to the high oxyphilicity of Ru providing the possibility of Ru-OH_{ad} at potentials less than 0.2 V vs. RHE; another reason that due to the ligand effect of Ru on Pt, the H_{upd} on Pt is weakened, leading to a cathodic shift in the H_{upd} peak[37, 133-134]. A more reasonable rationale for this growth is due to Ru-H_{upd} as the formation of Ru-OH_{ad} has only been observed at potentials <0.2V vs RHE[37]. These results align with the bifunctional mechanism in that the shift of the H_{upd} to lower potentials through the addition of the noble Ru facilitates the HOR/HER by lowering the energy barrier for the Volmer step[35].

The increase in activities with the addition of Ru in our Pt-based catalyst is illustrated in Figure 4.3d. We observe the highest current densities at low overpotentials in the $Pt_{0.7}Ru_{0.3}$ sample. More specifically, we measured the geometric-specific activities at ±10 mV to be 0.75 and 0.73 $mA*cm^{-2}_{geo.}$ for the HOR and HER regions of the polarization plot, respectively. In comparing the $Pt_{0.7}Ru_{0.3}$ catalysts with the $Pt_{0.9}Ru_{0.1}$ sample, we measured an increase in activities of 0.6 $mA*cm^{-2}_{geo.}$ in the anodic branch, and 0.46 $mA*cm^{-2}_{geo.}$ in the cathodic branch. This increase in activity is expected due to the bifunctionality of the Ru in high pH, in that it is capable of underpotential deposition of hydrogen (H_{UPD}), promoting the formation of hydroxide adsorption as aforementioned[35, 37]. This functionality allows for the increased kinetics of both the HOR and HER.

Conclusion

We synthesized carbon-supported bimetallic PtNi and PtRu electrocatalysts via a modified CVD process. Electron microscopy shows the 2-3nm in diameter deposited spherical nanoparticles are well dispersed on the carbon surface. X-ray analysis was utilized to elucidate the nature of the deposited nanoparticles. XRF disclosed the fractional metal content for each sample, which is closely aligned to our expected values via a mass balance. The phase of the electrocatalysts was found to be partial alloyed reduced metallic nanoparticles. The $Pt_{(1-x)}Ni_x$ samples lead to a higher amount of alloyed metal due to the subcomponents' similar FCC crystal structures. The $Pt_{(1-x)}Ru_x$ samples showed a lower degree of alloying per the dissimilar crystal structures inherent to the metals.

Electrochemical characterization of these samples for hydrogen reactions in alkaline showed improved activities through the addition of the oxyphilic metals. In the $Pt_{(1-x)}Ru_x$ samples, we measured an increase in mass and specific activities with an increase in Ru content. This improved performance would eventually decrease with further addition of Ru, as the mechanisms driving the increase in activity imposed by the bifunctionality of the catalyst would diminish as they support the activity on the Pt catalytic surface, not the Ru. Additionally, we found the increased activity is not a function of the degree of alloying for the $Pt_{(1-x)}Ru_x$ samples, as the inclusion of the oxyphilic metal aids in the reduction of the energy barrier needed to drive the Volmer step in the HOR/HER reactions.

The $Pt_{(1-x)}Ni_x$ samples show a decrease in exchange current density with an increase in metal content. We assume this is due to the increased pacified

oxide/hydroxide layer formed on the Ni surface in high pH. In either catalyst set, a thoroughgoing analysis to determine optimal stoichiometric ratios for these Pt-M electrocatalysts has not been conducted using this modified CVD technique, allowing room for further study. Additionally, the modified deposition process can be further explored to understand better mixed crystal-structured metals' alloying capability in this single-step process.

CHAPTER V

THE IMPACT CARBON SUPPORT HAS ON MODIFIED CHEMICAL VAPOR SYNTHESIZED HYDROGEN ELECTROCATALYST FOR ALKALINE MEDIA

Abstract

High surface area carbons have become primary supports for the catalyst of various electrochemical devices. In previous studies of a modified CVD method to synthesize electrocatalysts for fuel cell and electrolyzer devices, we proposed that the rates for nucleation and, in turn, growth of the deposited nanoparticles were a function of the concentration of nucleation sites of the supporting substrate. This study reinforces our initial proposal by studying various carbons as supports for platinum-based electrocatalysts for hydrogen reactions in alkaline media. After depositing 30 wt% Pt on three different supports using the aforementioned modified CVD method, we determine via material characterization that supports with higher surface areas lead to smaller Pt nanoparticles. Agreeably, these smaller particles promote higher electrochemical surface areas measured through hydrogen desorption and CO stripping analysis. Through further electrochemical and materials characterization, we determined the hydrophilicity of the carbon plays a significant role in the activities for the hydrogen reactions in alkaline, showing a 79.5% increase in performance of average exchange current density measured through Tafel and micro-polarization analysis, a 75% increase in specific activity, and a 34% increase in mass activity averaged over both hydrogen oxidation and hydrogen evolution when a hydrophobic support was used.

Introduction

Electrochemical devices are becoming essential components for the transition to sustainable energy. Polymer electrolyte fuel cells (PEMFCs) are one of the leading electrochemical devices that are being utilized in automotive and stationary power grids.

Fuel cells convert hydrogen and oxygen into electricity via a galvanic process. Furthermore, electrolyzers, which operate via an electrolytic process, offer a clean and efficient way to produce hydrogen suitable for its increasing demand, particularly to facilitate the use of FC devices. Platinum or platinum alloys are the most active catalysts to promote these reactions. However, the high cost of platinum has driven research to probe alternatives in order to reduce the cost of the catalyst.

Anion Exchange Membrane devices can employ platinum group metal-free (PGM-Free) catalysts for the oxygen reactions. However, the hydrogen reactions, namely the hydrogen oxidation and evolution reactions found in FC and electrolyzers, become sluggish due to increased hydrogen binding energy with increased pH. This overbending of H_2 decreases the activity of these reactions catalyzed on Pt by two orders of magnitude. Platinum is still the premier monometallic electrocatalysts, although the H_2 kinetics are slower in these devices.

Traditionally, particle size and distribution have led to an increased electrochemical surface area (ECSA)[112-114]. Theoretically, the increased ECSA leads to higher utilization in the catalyst layer in FC and electrolyzers increasing their performance[48, 135]. As such, variations in the synthesis process to develop platinum-based electrocatalysts have led to changes in catalytic activities[75, 136, 137]. To lower cost and increase ECSA, Pt-based electrodes have transitioned from Pt Black decorated on gas diffusion layers or carbon cloths through atomic layer deposition (ALD) or chemical vapor deposition (CVD) to Pt nanoparticles decorated on high surface area (HSA) carbon supports[43-45, 138]. HSA carbons are prized for their excellent electrical conductivity and low corrosion, enabling low ohmic resistances and increase durability when used in

the devices[139,140]. Traditionally the increased wettability allows for higher concentrations of electrolyte available to the catalytic layer resulting in high catalyst utilization through the electrolytes' uptake in half-cell reactions[141, 142].

Variations in the carbon's chemical and physical properties, e.g., functionality and surface topography, directly correlates to changes in the density of nucleation sites, regardless of the method used for catalysts synthesis[143,144]. In Chapter 2, we suggest that the rate law associated with nucleation for the modified CVD process is a function of the concentration of nucleation sites on the support material. Additionally, we discovered the deposition sites of the nanoparticles were at the interfaces of the carbon microparticles, where there are increased amounts of variations or defects in the carbon support's structure. The study conducted in Chapter 2 utilized the same support, Vulcan XC-72 (Cabot), for each sample to elucidate the impact varying the metal-organic salt precursor has on the modified CVD method. However, this leaves a gap in understanding the impact that the structure of the supporting material has on the PMCVD method.

In an effort to close this gap, we chose three different carbon supports: Vulcan XC-72, Acetylene Black (A.B.), and Graphitized Nanoplatelets (GNP). Literature provides insight into the variations of their surface areas which range from 45-600 m^2/g, where A.B. has the smallest surface area and GNP the highest[145-149]. Additionally, reports on the degree of graphitization measured through I_d/I_g ratios assessed with Raman spectroscopy varied across the field but agree with A.B. being more amorphous than the others and GNP having the highest order[145-149]. We selected these carbon supports because the trends for both surface area and graphitization concur, allowing us to assume

the concentration of nucleation sites would vary similarly, with an assumed trend as follows: A.B. < Vulcan XC-72 < GNP.

This assumption would enable us to validate our proposed rate laws for nucleation and growth by measuring the particle size distribution of the Pt nanoparticles deposited on these various supports through our modified CVD method. This study analyzes the synthesized electrocatalysts for both material properties and electrochemical activity for the hydrogen reactions in an alkaline environment. We provide information regarding the variations in activities due to the properties of the support material as a means to provide information on additional ways to tune particle size and potentially increase hydrogen reaction kinetics in AEM fuel cells and electrolyzers through carbon support material selection.

Experimental

Nanoparticle Synthesis. Catalysts were synthesized using a single-step chemical vapor deposition process. In this study, we utilized three different carbon supports: Vulcan Carbon XC-72R (Cabot), Acetylene Black (A.B) (Alfa Aesar), and unfunctionalized graphitized nanoplatelets (GNP) (cheaptubes). A powdered Platinum (II)(2,4)-pentanedionate [$Pt(acac)_2$] (Alfa Aesar) precursor was mechanically mixed with the various carbon support in glass vials to achieve the appropriate final metal loading of 30 wt% Pt; total mass was 50mg for each sample. The vials were then placed into a vacuum oven and a separate vial of deionized water (Milli-Q, Millpore). The oven was then sealed, evacuated with ultra-high purity N_2 to 28.37 kPa, and the temperature was set to 210 ^oC. After 15 hours, the vacuum oven was evacuated, purged again with UHP N_2, and cooled

to room temperature. The samples were then removed from the oven and weighed to confirm the metal content via a mass balance.

Materials Characterization: The various Pt/ XC-72 catalysts were analyzed using x-ray diffraction (XRD), scanning electron microscopy (SEM), transmission electron microscopy (TEM); surface areas and pore size distribution were measured by employing BET/BJH theories of physisorption isotherms. XRD patterns were obtained using a Siemens D5000 diffractometer using Cu radiation (l=0.154184 nm, 30kV 40mA, 0.05^{o} step, 1.0 ^{o}/min) in a Bragg-Brentano geometry. Aliquots of catalysts suspended in isopropyl alcohol (IPA) were smeared onto a zero-background quartz sample holder. Peak width analysis was performed using OriginPro using a Gaussian wave-fitting function after correcting the baseline. SEM images of the various carbons were taken using an FEI Quant'a TA 400F scanning electron microscope at an accelerating voltage of 20 kV and a working distance of 9.8 mm. Samples were placed on a carbon tape-covered aluminum sample holder. TEM micrographs were taken using an FEI Titan ETEM with Image Cs corrector operating at 300 keV, equipped with a Gatan K2-IS direct detection camera and a Gatan single-tilt holder. The electron flux to the sample was limited to 10 e^{-}/px/s to minimize beam damage. Surface area and pore size distribution measurements were performed using a 3Flex Micromeritics analyzer at 77 K with nitrogen as the absorbent. The apparent surface area covered by nitrogen was calculated using the BET for a pressure range of p/p^{o} 10^{-6} to 0.9995.

Electrochemical Characterization. The electrocatalysts were characterized at room temperature in a Teflon three-electrode electrochemical cell set-up (Pine) with a Mercury/ Mercury oxide (Hg/HgO) reference electrode (ALS) and a Platinum mesh counter electrode. Electrodes were made by depositing 8 µl of well-dispersed catalysts inks comprising of 5 mg of catalysts, four drops of DI water, and 1.0 g of IPA onto rotating glassy carbon electrodes (Pine, A=0.1963 cm^2) until dry. Electrode Loadings were measured using XRF (Thermo Scientific ARL Quant' x EDXRF Analyzer) referenced against a <5% error standard. An SP-50 potentiostat (BioLogic) was used throughout the electrochemical characterization process. Electrodes were stabilized by performing cyclic voltammetry (CV), sweeping voltages from 0.01- 1.0 V versus RHE in a 1.0 M solution of potassium hydroxide at 100 $mV*s^{-1}$ until stable. Polarization curves were then measured from -0.25- 0.25 V versus RHE at 2500 RPM in the positive direction. Potential electrochemical impedance spectroscopy (PEIS) spectra were collected at frequencies from 1 kHz to 1 Hz at -0.1, 0.0, and 0.1 V with a 10mV sinusoidal amplitude modulation. The averaged intercept of the spectrums along the real axis, at the high frequencies, was taken as the ohmic resistance of the electrolyte and used to produce iR-free plots. Electrochemical active surface area (ECSA) measurements were calculated from CO stripping using a 1000 ppm UHP CO bal. N_2 source and H_{UPD} region in a 0.1 M solution of perchloric acid at a scan rate of 2 $mV*s^{-1}$. Voltage was cycled from 0.05-0.25 V vs. RHE for 1 hour. Stripping was conducted by scanning from 0.0-1.4 V vs. RHE in the positive direction. Both areas of the hydrogen desorption region and CO oxidation peak were obtained using OrginPro integration software.

Results and Discussion

Figure 5.1 (Top) depicts XRD profiles of 30 wt% Pt/ varied carbon supports. These profiles were collected to determine the phase and crystallite size of the deposited nanoparticles. Scans were taken to show the Pt (111) and Pt (200) peaks by scanning from 15-60^{o} 2θ as previous investigations showed that the phase of the deposited nanoparticles is fully reduced Pt/C when synthesized using the PMCVD process. Within this scanning range, we also observe the C (002) peak at ~26^{o} 2θ. We measured the crystallite size (L) in each sample using the Scherrer equation, Equation 5.1, by measuring the Full Width at Half Maximum (FWHM), b_L, of the Pt (111) peak using OrginPro software. In this equation, λ is the wavelength of the incident x-ray beam (1.54 Å), and θ is the Bragg angle of diffraction for the Pt (111).

$$\boldsymbol{\beta_L = \frac{0.9 * \lambda}{L * \cos\theta}} \qquad (\mathbf{5.1})$$

The measured average crystallite size for each sample was 2.39, 2.81, and 2.00 nm for 30% Pt/ XC-72, 30% Pt/ Acetylene black, and 30% Pt/ Graphitized nanoplatelets, respectively. The calculated lattice parameters are in close agreement (±0.009 Å) with metallic Pt (3.92 Å). The measured crystallite size of the 30% Pt/ XC-72 sample is in close agreement with those calculated in Chapters 2 (2.48 nm) and 3 (2.314 nm) synthesized at the same conditions (±0.08 nm), showing repeatability of the PMCVD method.

BET surface area analysis, Figure 5.1 (Bottom), depicts N_2 adsorption and desorption isotherms of the various samples post-deposition.

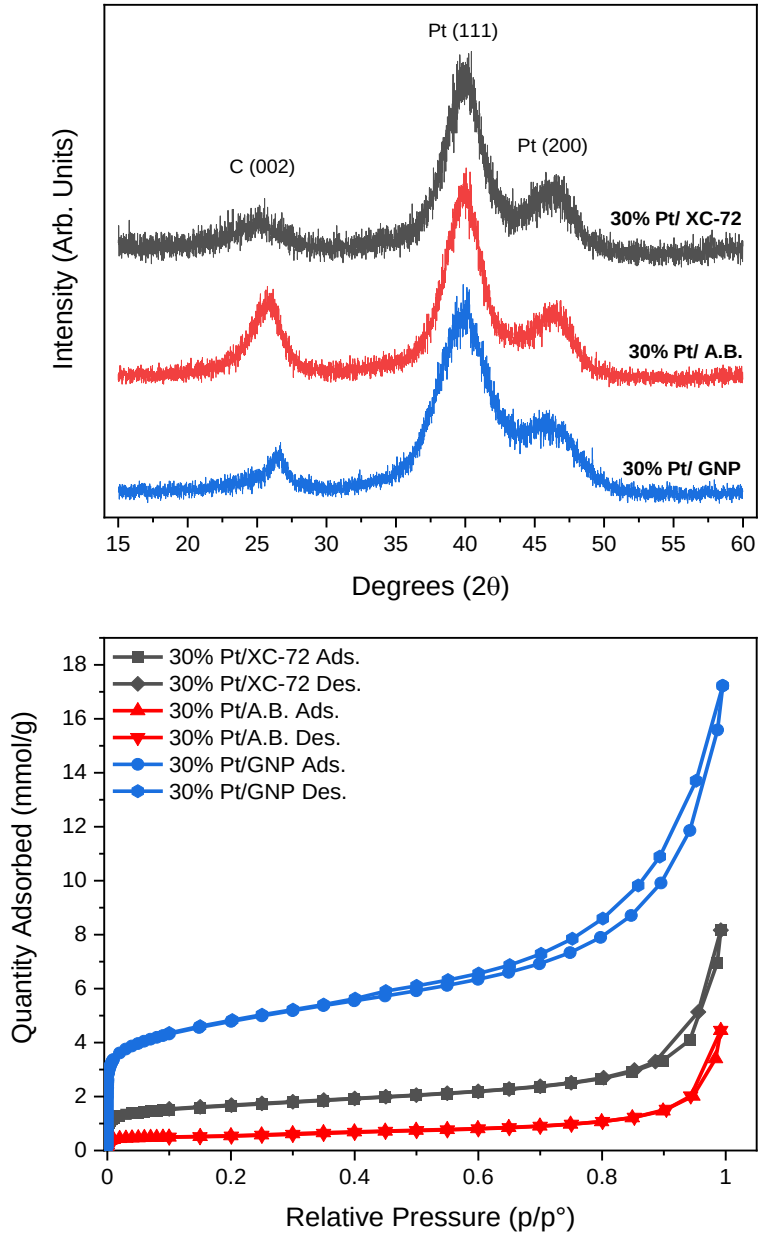

Figure 5.1: (Top) Cu Kα X-ray diffraction patterns of 30% Pt/ XC-72, 30% Pt/ Acetylene Black (A.B.) and 30% Pt/ Graphitized Nanoplatelets (GNP) vapor synthesized catalysts. (Bottom) BET surface area of N2 adsorption and desorption Isotherms of 30% Pt/ Various Carbon Supports.

The measured surface areas agree with the literature in that the surface area of A.B<XC-72<GNP. We see this trend supports the variations in crystallite sizes of the deposited nanoparticles, indicating an increase in support surface area results in a decrease in crystallite size. Table 5.21 shows the measured crystallite size and surface areas. We attribute this trend to the increase in nucleation sites available in higher surface area materials per our proposed rate laws in Chapter 2. Because the concentration of Pt is the same, the supports with lower surface area and less assumed nucleation sites will cause the crystallites to continue to grow once all nucleation sites are occupied, e.g. $[N_s]=0$. This result provides evidence of the tuneability of the crystallite size via changing the surface area of the supporting material.

Without any surface chemical analysis to identify any moieties on the carbons studied, it is challenging to assume the species of the nucleation sites outside of voids or defects intrinsic to carbon structures. Thus, the identified deposition sites at the interfaces of the carbon supports provide insight into the nucleation sites for the PMVCD method. This directly ties the supporting materials' physical properties (e.g., topography, surface areas, roughness, particle size, porosity, and graphitization) to the concentration of nucleation sites available.

Table 5.1: Lattice parameter (a), crystallite size, and BET analysis of 30%Pt/ XC-72, 30% Pt/ Acetylene Black (A.B.) and 30% Pt/ Graphatized Nanoplatelets (GNP). Included in parentheses are the standard deviations for the measured particle sizes.

Sample Name	2q (°)	a (Å)	FWHM (°)	Crystallite Size (nm)	Particle Size (nm)	Surface Area (m^2*g^{-1})
30% Pt/ XC-72	39.907	3.929	3.699	2.39	3.02 (.12)	255.81
30% Pt/ A.B.	39.874	3.932	3.143	2.81	4.43 (.06)	79.75
30% Pt/ GNP	39.819	3.937	4.417	2.00	2.14 (.01)	356.12

Figure 5.2a-c provides SEM micrographs of each sample. We can observe the various morphologies of each support; a) XC-72, b) Acetylene Black, c) Graphitized Nanoplatelets. XC-72 and A.B. are shown to be continuous mounds of carbon microparticles. We perceive the microparticles found in A.B. are larger than in XC-72, owing to A.B.'s reduced surface area. Figure 5.2c shows the conformation of the graphitized carbon nanoplatelets as stacks of nanosheets varying in size. Unlike the other supports, GNP shows defined edges in its microstructure because of its increased graphitization.

TEM micrographs of the platinum nanoparticles deposited on the following carbon supports: Pt/ XC-72 (d,g), Pt/ A.B. (e,h), and Pt/ GNP(f,i) with two variations in magnification are shown in Figure 5.2d-i. These micrographs show the high distribution of the Pt nanoparticle deposited on each of the various carbons. We observe an increase in particle agglomeration with a decrease in support surface area. This agglomeration is seen in Figure 5.2e&h, where the nanoparticles deposited on the A.B. support have coalesced in high concentrations of previously defined low energy sites on the unions of the carbon microparticles. This is in comparison to the nanoparticles that are supported on GNP, Figure 5.2f&I, which are highly uniform in size and well distributed on the carbon surface, where even particles in proximity to each other can be easily distinguished. These findings further corroborate our proposed rate laws associating nucleation with the concentration of nucleation sites available.

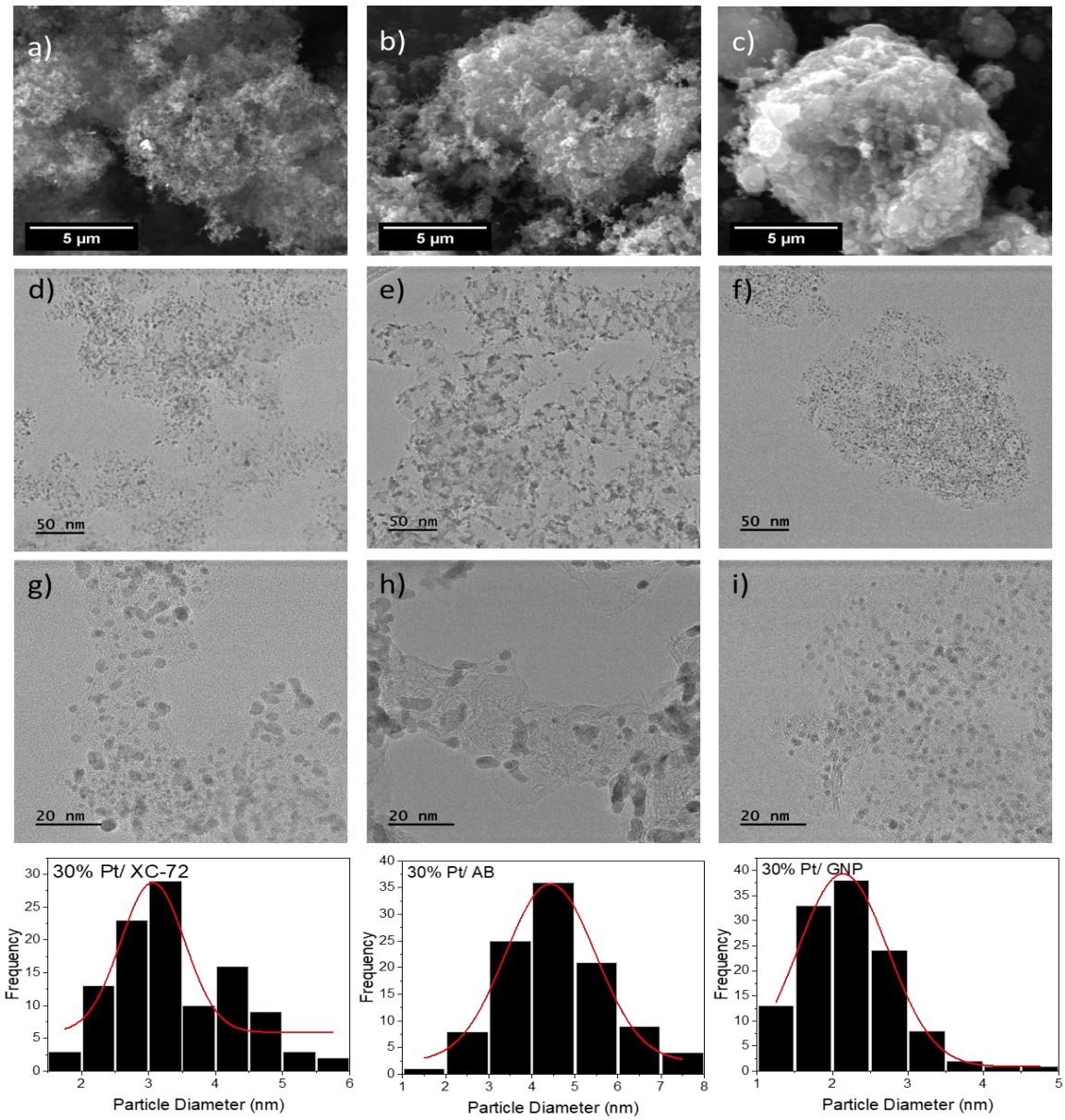

Figure 5.2: Microscopy analysis of Pt nanoparticles deposited on various carbon support. (a-c) SEM micrographs taken at an accelerating voltage of 20 kV and a working distance of 9.8 mm to show carbon morphology of Pt/XC-72, Pt/AB, and Pt/ GNP, respectively. TEM micrographs of Pt/ XC-72 (d,g), Pt/ A.B. (e,h), and Pt/ GNP(f,i) with varying magnification to show particle size and particle distribution. Histograms are shown in the bottom line of the figures for the respective analysis of 100 nanoparticles.

With an increase in nucleation sites through an increase in surface area, we expect smaller nanoparticles per our proposed rate laws. We validated this assumption through particle size analysis by examining the diameters of +100 particles in various locations of the sample. The average diameters were calculated through Gaussian fits of the histograms produced from our particle size analysis in OriginPro software and were measured to be 3.02, 4.42. and 2.14 nm on average for Pt/ XC-72, Pt/ A.B., and Pt/ GNP respectively. Included in Table 5.1 are the measured particle sizes mentioned, with the standard deviation included in paratheses. These variations in size of the highly dispersed particle corroborates our proposed rate law for nucleation. The larger surface area GNP support enabled the smallest particles to deposit, thus implying that the concentration of nucleation sites is proportional to the surface area. This increase in nucleation sites would allow for faster Pt deposition, lowering Pt concentrations, ultimately lowering particle growth. The shape of the deposited Pt nanoparticles varies from spheres in the XC-72 and GNP supported sample to "bean-like" structures on the A.B. supported sample. A rationale for the variations in shape is included in the conclusion of this chapter.

We measured electrochemical surface areas (ECSA) by calculating the charge produced through both H_{upd} and CO stripping through the voltammograms produced in 0.1 M $HClO_4$ found in Figure 5.3 (Left). We conducted ECSA calculations from the H_{upd} region in the same method found in Chapter 3. To calculate the ECSA of the CO oxidation region produced through CO stripping, we use equation 5.2 after measuring the charge, Q_{CO}, though integrating the areas under the dashed lines in Figure 5.3 (left) from 0.6-0.14 V vs. RHE using the solid lines as the baseline for integration.

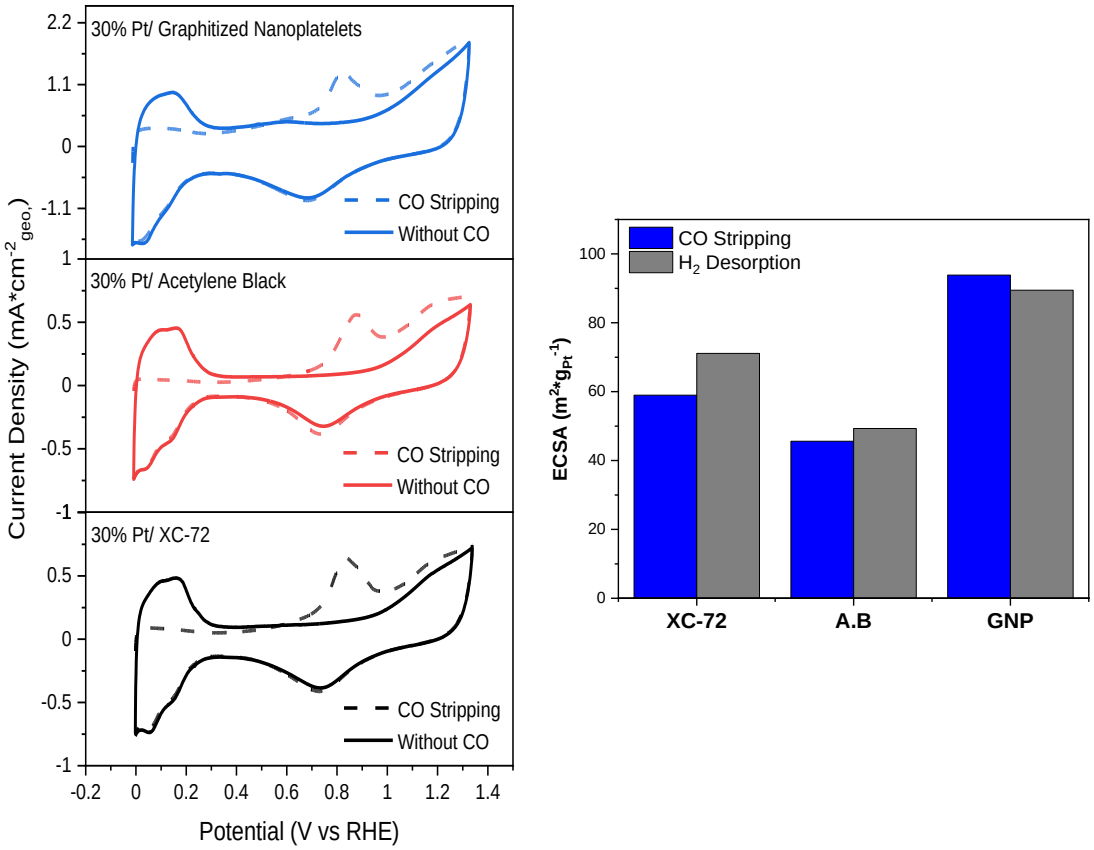

Figure 5.3: Electrochemical active area calculated from both Hupd desorption regions as well as CO Stripping. (Left) voltammograms of CO stripping depicting the Pt's saturation with CO thought the depressed hydrogen desorption region between 0.0-0.3 V vs. RHE and CO oxidation at potentials <0.6 V vs. RHE. The dashed line profile shows the initial stripping scan. Solid line profiles depict the second scan post-CO oxidation showing a restoration to the Hupd region. (Right) A bar chart of ECSA for both CO stripping (blue) and H_2 desorption region (gray) for the various carbon supports.

$$ECSA_{Pt}(m^2 g_{Pt}^{-1}) = \frac{Q_{CO}(C)}{420 \mu C cm_{Pt}^{-2} L_{Pt}(mg_{Pt} cm^{-2}) A_{disk}(cm^2)} \quad (5.2)$$

Similar to variables found in Chapter 3, L_{Pt} is the Pt loading measured through XRF, and A_{Disk} is the geometric surface area of the glassy carbon electrode. The charge density to oxidize a monolayer of CO from the Pt's surface is 420 $\mu C*cm^{-2}$[150]. Electrodes were saturated with ultrahigh purity 1000 ppm, CO Bal. N_2 while the voltage was cycled within the H_{upd} region from 0-0.3 V vs. RHE for one hour. We determined the saturation time by calculating the average current difference between three separate scans. Once the change in current for hydrogen desorption reached <0.000005 mA, the electrolyte was purged with UHP N_2 for 30 minutes then the scan range was extended to 1.4 V vs. RHE to strip the CO from the surface. Two additional scans were taken after the monolayer of CO was stripped to ensure no redeposition of CO occurred. Table 5.2 (Right) includes the calculated ECSA values measured from both H_{upd} and CO stripping.

Although the chosen threshold regarding the change in current is stringent, we still measure currents associated with H_{upd}, providing evidence that not all Pt surfaces were covered by CO within the hours-time. The average standard deviation between the ECSAs calculated is 3.37 $m^{2}*g_{Pt}^{-1}$. This deviation can be associated with the different chemistry that occurs on the surface of the electrode for the two adsorbents.

H_{upd} on Pt and Hydrogen evolution readily occurs at low overpotentials in acid and thus increasing the relative concentration of hydrogen near the electrode's surface impacting calculations[28]. However, in CO stripping, the concentration of CO in the bulk electrolyte is assumed to be zero after the 30 min purge of N_2. This variation in concentration impacts the charge associated with hydrogen desorption, resulting in a

higher calculated ECSA though H_{upd} on average. This can be compensated for by scanning in a potential region starting >0 V vs. RHE, driving the HOR over the HER. ECSA calculations measured through integration are estimates; thus, our standard deviation between methods is acceptable[151].

Electrochemical characterization, displayed in Figure 5.4, was conducted to probe the activities of the various Pt supported on carbon samples for the HOR/HER in alkaline media. Figure 5.4a shows the initial voltammograms for each of the samples. Cycles were scanned anodically from 0.05-1.0 V vs. RHE at 100 $mv*s^{-1}$. Each sample was cycled until scans overlapped three times sequentially. We observed expected variations in the associated double-layer regions, ~0.4-0.6 V vs. RHE, corresponding to the carbon surface areas where 30% Pt/ GNP has the most significant double-layer capacitance per its high surface area.

Figure 5.4b shows the measured performance for the HOR/HER though iR-corrected polarization plots scanning from -0.075-0.25 V vs. RHE in the positive direction. The inset shows the current densities at low overpotentials for the hydrogen reactions. Through these plots, we observe the highest performance with 30% Pt/ A.B. with 30% Pt/ GNP exhibiting the lowest activity at small overpotentials for both HOR and HER. To better present the kinetics of each sample, the exchange current densities for the hydrogen reactions through Tafel, Figure 5.4c, and micropolarization, Figure 5.4d plots. The exchange current densities were calculated through linear extrapolation, as similarly done in Chapter 3.

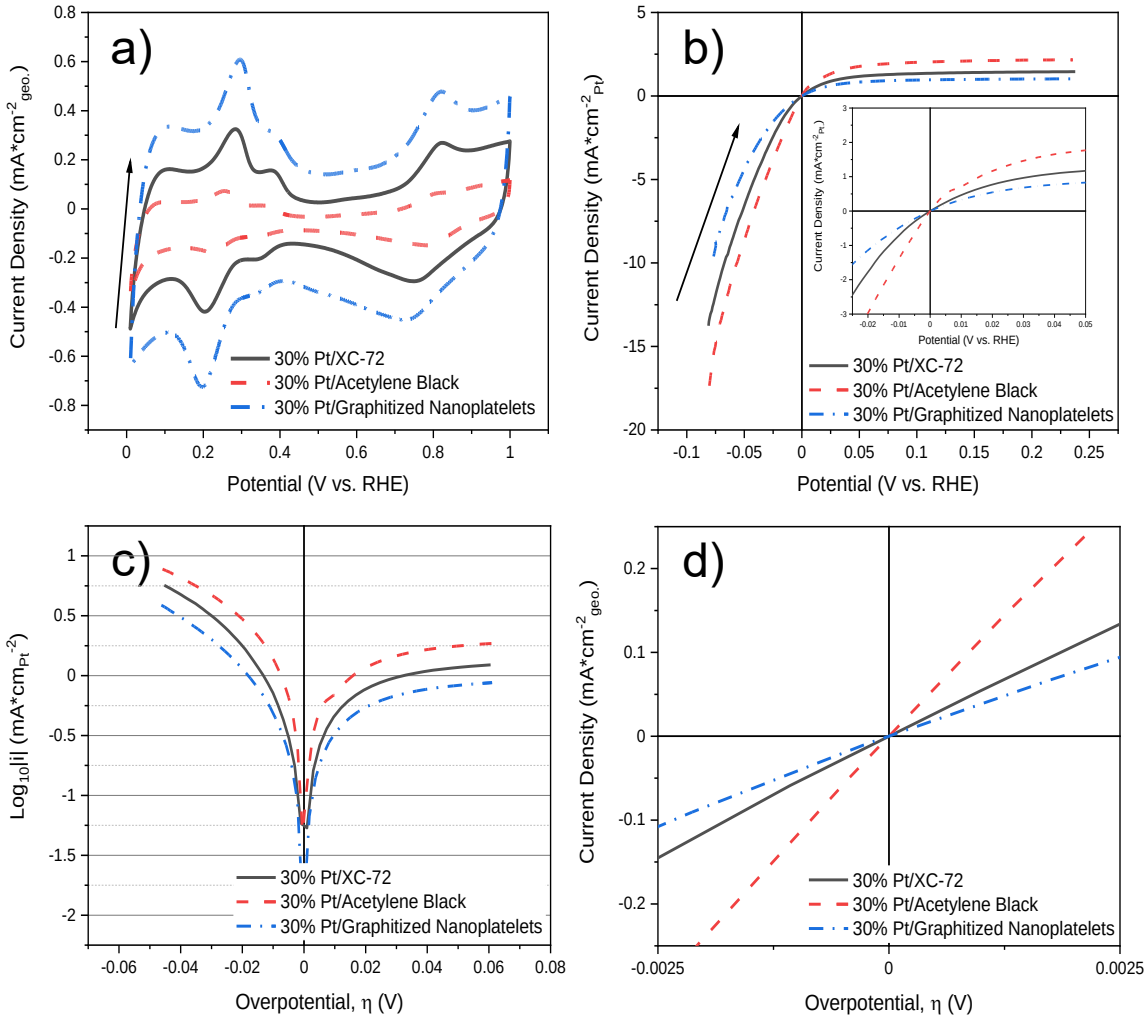

Figure 5.4: Electrochemical characterization of 30% Pt/ XC-72, 30% Pt/ Acetylene Black (A.B.) and 30% Pt/ Graphitized Nanoplatelets (GNP) vapor synthesized electrocatalysts. (a) Cyclic voltammograms (CVs)of each sample in 0.1 M NaOH at a scan rate of 100 mV*s-1. (b) iR-corrected polarization plots were taken at 2 mV*s-1 in 0.1 M NaOH at 2500 RPM. (c) Tafel plots and (d) micropolarization plots of each sample.

Additionally, exchange current densities of the three samples were calculated through slope analysis of the micropolarization plot using equation 3.

$$\boldsymbol{i_o = \frac{j}{\eta} * \frac{RT}{nF}} \qquad (\mathbf{3})$$

In this equation, the exchange current density, i_o, is equal to the slope of the micropolarization plot, j/η, multiplied by the ideal gas constant, R, and temperature in Kelvin, T, divided by the number of electrons, n, transferred for the hydrogen reactions, which in this case is 2, times Faraday's constant, F[153]. This equation is a rearrangement of the linearized Butler-Volmer equation, where the at low overpotentials, the exponentials of the Butler-Volmer equation, equation 4, where α is the transfer coefficient, can be expanded through a Taylor series, resulting in the abridged form found in equation 3[152-154].

$$\boldsymbol{i = i_o\left[e^{(1-\alpha)nF\eta/RT} - e^{-\alpha nF\eta/RT}\right]} \qquad (\mathbf{4})$$

Additionally, mass and specific activities were measured at overpotentials of ±10 mV vs. RHE through linear interpolation of the polarization plot. The measured activities as well as the calculated exchange current densities for each sample are given in Table 5.2. The current densities shown were normalized to the ECSA calculated through the integration of the H_{upd} region.

Table 5.2: Pt loadings measured by XRF, ECSA calculated from CVs using both Hupd and CO stripping, as well as hydrogen reaction activities of 30% Pt/ XC-72, 30% Pt/ Acetylene Black (A.B.), and 30% Pt/ Graphitized Nanoplatelets (GNP)samples. Micro polarization results were calculated from linear fitting of the polarization plots at low overpotentials. Mass and specific activates were calculated through linear interpolation of the polarization plots at ±10 mV.

Sample Name	Loading ($mg_{pt}*cm^{-2}$)	ECSA ($m^2*g_{Pt}^{-1}$)		Exchange Current Density		Activities			
				Micro Polarization	Tafel Extrapolation	$i_{h(10\ mV)}$	$i_{h(10\ mV)}$	$i_{h(-10\ mV)}$	$i_{h(-10\ mV)}$
		H_{UPD}	CO Stripping	($mA*cm^{-2}_{Pt}$)	($mA*cm^{-2}_{Pt}$)	($mA*cm_{Pt}^{-2}$)	($A*g_{Pt}^{-1}$)	($mA*cm_{Pt}^{-2}$)	($A*g_{Pt}^{-1}$)
Pt/XC-72	26.34	71.11	58.98	0.66	0.89	0.46	27.41	0.71	41.98
Pt/A.B.	26.85	49.32	45.61	1.42	1.28	0.71	32.34	1.39	63.23
Pt/GNP	24.36	89.45	93.84	0.485	0.66	0.33	30.87	0.49	45.64

The catalytic activity for the HOR and HER increases accordingly: 30% Pt/ Graphitized Nanoplatelets < XC-72 < Acetylene Black. As mentioned earlier in this section, the wettability of the carbon support can lead to an increase in activities. We conducted contact angle measurements on each sample by depositing a thick layer of non-decorated carbon samples on a glass slide until an opaque film of carbon was produced. A small bead of water (~3µl) was then deposited on each sample, and the contact angle was measured through ImageJ software. Both XC-72 and GNP samples exhibited hydrophilicity, adsorbing the water droplet before an image could be rendered. The A.B. sample shows hydrophobic behavior with an average contact angle of 42.95º. A depiction of these findings is given in Figure A5.1.

We attribute the higher kinetics in the AB sample to its support's wettability. In the hydrophobic AB supported catalyst, channels are available for gas to escape leading to higher hydrogen removal rates as the product of the reaction for the HER. This postulate is supported by Le Chatelier Principle. This explanation holds for the HOR as well in that the water produced through this reaction is easily removed from the surface of the electrode per the material properties of the A.B. support. We can evidence the increase in gas production at slower rotations given in Figure A5.2. Here we see that at 100 RPM, a gas bubble indicated by the sizeable oxidative peak appears as we produce H_2 at low overpotentials for the hydrogen evolution reaction. This peak decreases as we increase rotation, enabling faster removal rates for H_2 gas from the catalytic surface. This

phenomenon is not seen in the other two samples, attributing this formation to the hydrophobicity of the A.B. sample. Additionally, because of the voltage scan direction, we increase the local H_2 concentration per this theory, aiding to the additional increase in activity for the HOR.

A study on the impact that electrode wettability has on the HER in acid suggested that hydrophilic surfaces increase reaction kinetics[141]. In this study, they utilized light-sensitive TiO_2 nanotubes as the support to vary wettability. These nanotubes still have capillary effects impacting the true wettability of the material surface through the uptake of water in the nanotubes, making them more hydrophilic. Our measurement for wettability is more realistic than what would be expected in a device as we eliminate capillary impacts by using carbon supports. Thus, our rationale for the increase in reaction kinetics of the hydrophobic AB supported catalyst is valid, although it contradicts prior similar studies.

The high rate of H_2 removal in alkaline devices has been a challenge for electrolysis as a build-up of the gas at the surface due to the increase HBE in high pH leads to slower removal rated to the desired product. Therefore, the AB sample's hydrophobicity shows excellent promise as a catalyst for HER in an AEM electrolyzer device. Additionally, the material property of A.B. can aid in water management in both PEM and AEM to prevent flooding at high current densities, allowing for higher efficacies and power outputs. This implies the need to tests these catalysts in a device to verify our assumptions of the material's properties leading to variations in activities.

Conclusion

Platinum nanoparticles of ~ 2-4 nm in diameter were deposited on XC-72, Acetylene Black, and Graphitized Nanoplatelets support. The particle size variations aligned with the differences in the support surface areas, where smaller particles were achieved on higher surface area supports. Additionally, we see the same trend concerning crystallite size. This provides another way to tune particle size outside of the parameters mentioned in chapters 2 (concentration) and 3 (temperature and pressure). The electrochemical surface area follows an expected trend where smaller particles lead to higher electrochemical surface areas. The activities normalized to the ECSA, calculated through H_{upd} stripping, follow the trend of Pt/ AB>XC-72> GNP. Although this trend is inverse of the rank order based on the ECSA, we attribute the increased performance to the hydrophobicity of the carbon supports where AB exhibits high hydrophobicity promoting gas removal promoting the HER, and water removal for the HOR. Additionally, because of the scanning direction for these polarization plots, the hydrophobic A.B. sample promotes high concentrations of H_2 near the catalyst surface aiding in the HOR performance. It is challenging to predict the performance of these electrocatalysts in a device. The materials' characteristics afford the AB sample promise as the material properties will help with water management in both acid and alkaline FC and electrolyzer devices.

Interestingly, the “bean-like “shape of the deposited nanoparticles on A.B. are different from those supported on XC-72 and GNPs. Though disclosing the AB

support's hydrophobicity, the water vapor produced through the synthesis process may develop an envelope for these nanoparticles. The "bean" shapes produced have their concave portions towards the outside of the carbon structure. Through the water vapor interactions with the carbon supports during the deposition process, there is a possibility of controlling particle shape using the PMCVD method. This is challenging to verify without using more structured hydrophobic supports. Because A.B. is amorphous, we found variations in the shapes produced when it was used as support. By identifying variations in the size of the highly dispersed nanoparticles on the various carbon supports, we provide additional evidence that the rate of nucleation is a function of nucleation site concentrations, and the rate of growth and agglomeration is a function of Pt loading. However, the nature of nucleation sites on these amorphous carbons remains undefined. These findings provide an additional area of investigation to better understand the capabilities of the PMCVD method.

CHAPTER VI

SYNTHESIS AND CHARACTERIZATION OF CHEMICAL VAPOR SYNTHESIZED PRECIOUS GROUP METAL FREE ELECTROCATALYST FOR HYDROGEN EVOLUTION IN ALKALINE MEDIA

Abstract

The deposition of Ni and Co's in both mono and bimetallic conformations using a modified chemical vapor deposition (CVD) mechanism was studied. This modified CVD method utilizes acetylacetonate organometallic salt precursors sublimed in a vacuum oven to produce crystallites ranging from 3.5-23.8 nm based on the deposited phase. The phase of these samples, determined through diffraction, varied from reduced metals to bimetallic oxide compounds. Herein, we show a novel way to synthesize nanoparticles with metastable Ni and Co hexagonal structures without using solution-based methods. The mono and bimetallic samples were characterized for hydrogen evolution reaction activity in alkaline environments. The activities were measured through polarization curves allowing us to compare the various electrocatalysts. The most active phase was hexagonal close-packed (HCP) structured Ni.

Additionally, we uncover the role water plays in the modified CVD process regarding the deposition of these transition metals. This study was facilitated by phase analysis of the various samples after post-deposition heat treatments. This study began the necessary investigation on water vapor interaction with the acetylacetonate ligand during the deposition process.

Introduction

Clean and efficient production of hydrogen is essential to reverse the effects of reliance on nonrenewable resources. The most common ways to produce

hydrogen are stem-methane reforming and electrolysis or water splitting[155, 156]. Steam-methane reformation involves the reaction between high temperature and pressure steam with methane to produce hydrogen with byproducts still including CO_x species. However, electrolysis offers a CO_x-free scheme for H_2 production. Electrolysis involves the splitting of water over a catalyst under electrical potentials. Commercial electrolyzers are catalyzed on the cathode, where the hydrogen is produced, by Platinum. The activity of Pt as a catalyst increases as pH decreases per the Hydrogen binding energy theory[23,24,30-32]. As such, proton exchange membranes (PEM) are uses as an ion-permeable separator for the anode and cathode electrodes in these devices.

Ir typically catalyzes the anode process in these PEM devices. The use of these two precious group metals (PGMs), Pt and Ir, leads to a more expensive device due to their rarity and associated cost[175]. As such, PGM-Free electrodes have been studied as electrocatalysts for both the anode and cathode in electrolyzers. Similar activities to that of PGM electrocatalysts have been met by utilizing PGM-free metals, mainly metal oxides, on the anode to catalyze the oxygen reduction reaction (ORR) in alkaline media[18-22]. The use of single and bimetallic transition metals such as cobalt, manganese, nickel, iron, and their oxides has closed the performance gap between PGM and PGM-free electrocatalysts, potentially driving down costs of the device[158]. However, regardless of the metal type, the kinetics of the hydrogen evolution reaction (HER) on the cathode decrease by two orders of magnitude because of increased

hydrogen binding energies in higher pH. In higher pH, platinum still exhibits superior HER kinetics to other metals, producing 1 $mA*cm^{-2}$ at overpotentials of 30 mV for unsupported and 50 mV for carbon-supported Pt[159].

This study investigates mono and bimetallic Ni and Co electrocatalysts for the HER in alkaline to reduce device cost through synthesizing these PGM-free electrocatalysts using a low-cost modified chemical vapor deposition (CVD) method. These earth-abundant metals were chosen for their low cost and promise as a substitute for Pt. Notably, Ni offers excellent corrosion resistance even in highly concentrated alkaline media, and Co offers good durability and electrical conductivity[158,159]. This study's modified CVD method involves the thermal decomposition of acetylacetonate organometallic salt precursors to produce various phased nanoparticles supported on carbon. We study the deposited phase as a function of individual Ni and Co metal content in each sample and adjust the reaction process to uncover the influence water has on the deposition method when using transition metal-based precursors such as $Ni(acac)_2$. We further investigate the activities of these various phases for the HER in 0.1 M NaOH via half-cell reactions.

Experimental

Nanoparticle Synthesis. The electrocatalysts were synthesized using a single-step chemical vapor deposition process using a Vulcan XC-72R Carbon (Cabot) support and various combinations of acetylacetonate precursors. The

metal-organic salt precursors used in this study were Nickle (II) Acetylacetonate, $Ni(acac)_2$, and Cobalt (III) Acetylacetonate; $Co(acac)_3$, (Alfa Aesar). The Ni, Co, and Ni_xCo_y, where x and y denote the partial fraction of the total metal weight, samples were prepared to have a metal weight percent (wt.%) of 30% supported on the XC-72R carbon (70 wt.%). The total mass of each electrocatalyst was 50 mg. In the $Ni_xCo_{(1-x)}$ samples, the precursors were mixed to achieve Ni:Co ratios of 80:20, 50:50, and 20:80. Once the precursor mixtures were prepared, the salts were then mechanically mixed with the carbon supports in glass vials. The vials were then placed into a vacuum oven along with a separate vial of deionized water (Milli-Q, Millpore). An exception to the addition of the water was in the synthesis of the Ni no H_2O sample. The oven was then purged with ultra-high purity (UHP) N_2, evacuated to 13.27 kPa, and the oven was set to 260 ^oC. After 15 hours, the vacuum oven was evacuated, purged again with UHP N_2, and cooled to room temperature. A mass balance was used to determine the total metal content of each catalyst post-deposition. Portions of the as-synthesized samples were then heat-treated in a tube furnace with UHP O_2 and saturated N2 at 260 ^oC for 1 hour.

Materials Characterization: The electrocatalysts were analyzed using x-ray diffraction (XRD) and transmission electron microscopy (TEM). XRD patterns were obtained using a Siemens D5000 diffractometer using Cu radiation (l=0.154184 nm, 30kV 40mA, 0.05^o step, 1.0 ^{o}/min) in a Bragg-Brentano geometry. The scan range was 15-60 $^o2\theta$. Aliquots of catalysts suspended in isopropyl alcohol (IPA)

were smeared onto a zero-background quartz sample holder. The IPA was evaporated before measurements. Each sample's phase was determined through a search and match process enabled by the PDF-4 database included in the utilized Jade software (MDI). Additionally, the phases were confirmed by comparing the diffraction patterns to those found in the literature by searching the inorganic crystal structure database (ICSD). TEM images were taken on an FEI Titan ETEM with an Image Cs corrector, operating at 300 keV. The microscope was equipped with a Gatan K2-IS direct detection camera and a Gatan single-tilt holder. To minimize beam damage, the electron flux to the sample was limited to 10 e-/px/s.

Electrochemical Characterization. Electrocatalysts were characterized at room temperature in a Teflon three-electrode electrochemical cell (Pine) with a Mercury/Mercury Oxide, Hg/HgO reference electrode (ALS), and a Platinum mesh counter electrode (Pine). Electrodes were made by depositing 8 µl of well-dispersed catalysts inks, comprising 5 mg of catalysts, four drops of DI water, and 1.0 g of IPA, onto glassy carbon electrodes (Pine, A=0.1963 cm^2) and left rotating at 500 RPM until dry. Electrode Loadings were measured using XRF (Thermo Scientific ARL Quant' x EDXRF Analyzer) referenced against a <5% error standard. An SP-50 potentiostat (BioLogic) was used throughout the electrochemical characterization process. Electrodes were stabilized using cyclic voltammetry (CV) in a 1.0 M solution of potassium hydroxide at 100 $mV*s^{-1}$ at

potentials within the water window for each sample. Polarization curves were then measured at 900 RPM in the positive direction at 2 $mV*s^{-1}$ at potentials < 0.1 V vs. RHE Potential electrochemical impedance spectroscopy (PEIS) spectra were collected from 1 kHz to 1 Hz at -0.1, 0.0, and 0.1 V. with a 10mV sinusoidal amplitude modulation. The intercept of the spectrum along the real axis at high frequencies was taken as the ohmic resistance of the electrolyte to produce air-free plots.

Results and Discussion

Ni, Co, and bimetallic $Ni_xCo_{(1-x)}$ supported on carbon electrocatalysts were synthesized via a single-step chemical vapor deposition process. XRD was utilized to determine the phase of the mono and bimetallic electrocatalysts. Figure 6.1 displays the as-synthesized diffraction profiles for each sample. The phases were determined by matching the diffraction patterns to powder diffraction files found in the Inorganic Crystal Structure Database (ICSD) through a PDF 4+ plug-in available through Bruker's Jade software as well as in the literature. We determined the phase for the Ni/ XC-72 without H_2O sample to be HCP Ni, Ni/ XC-72 to be NiO, $Ni_{0.8}Co_{0.2}$/ XC-72 and $Ni_{0.5}Co_{0.5}$/ XC-72 to be FCC Ni and $CoNiO_2$, $Ni_{0.2}Co_{0.8}$/ XC-72 to be CoO, FCC Ni and $CoNiO_2$, and the Co/ XC-72 sample to be CoO. The crystallite size for these nanoparticles ranges from 3.5-23.8 nm measured through the Scherer Equation.

Each of the bimetallic catalysts possesses a $CoNiO_2$ phase in their diffraction profiles shown through peaks located at 36.8 (111) and 42.8 (200) $^o2\theta$.

Additionally, we observe a more crystalline Ni (FCC) phase indicated by peaks at 44.5 (111) and 51.8 (200) $^{o}2\theta$in each of the bimetallic samples. As expected, the Ni phase's relative intensity decreases with an increase in Co concentration, apparently promoting increased production of $CoNiO_2$ nanoparticles. We do not observe any other Co phases besides $CoNiO_2$ until the Co concentrations are above 80 wt%, e.g., $Ni_{0.2}Co_{0.8}$ and Co/ XC-72. For the bimetallic $Ni_{0.2}Co_{0.8}$/ XC-72 sample, we see small amounts of NaCl structured CoO peaks appearing at 36.5 (111) and 42.4 (200) $^{o}2\theta$ although the FCC Ni and $CoNiO_2$ phases are more predominate.

In the monometallic Ni/ XC-72 sample, we observe the FCC NiO phase defined by peaks at 37.3 (111) and 43.2 (200) $^{o}2\theta$; this is the only phase found in the monometallic Ni/ XC-72 sample. This, in addition to the results given in Figure A4.1, shows the modified deposition processes propendency to produce oxidized Ni through the deposition process when water is added to the reaction, and $Ni(acac)_2$ is used as the precursor. The NiO crystallites produced appear to be small relative to the other Ni crystals formed in the bimetallic catalysts. This assessment is based on the relative peak breadth associated with crystallite size and microstrain, where broader peaks indicate smaller particle size according to the Scherer Equation.

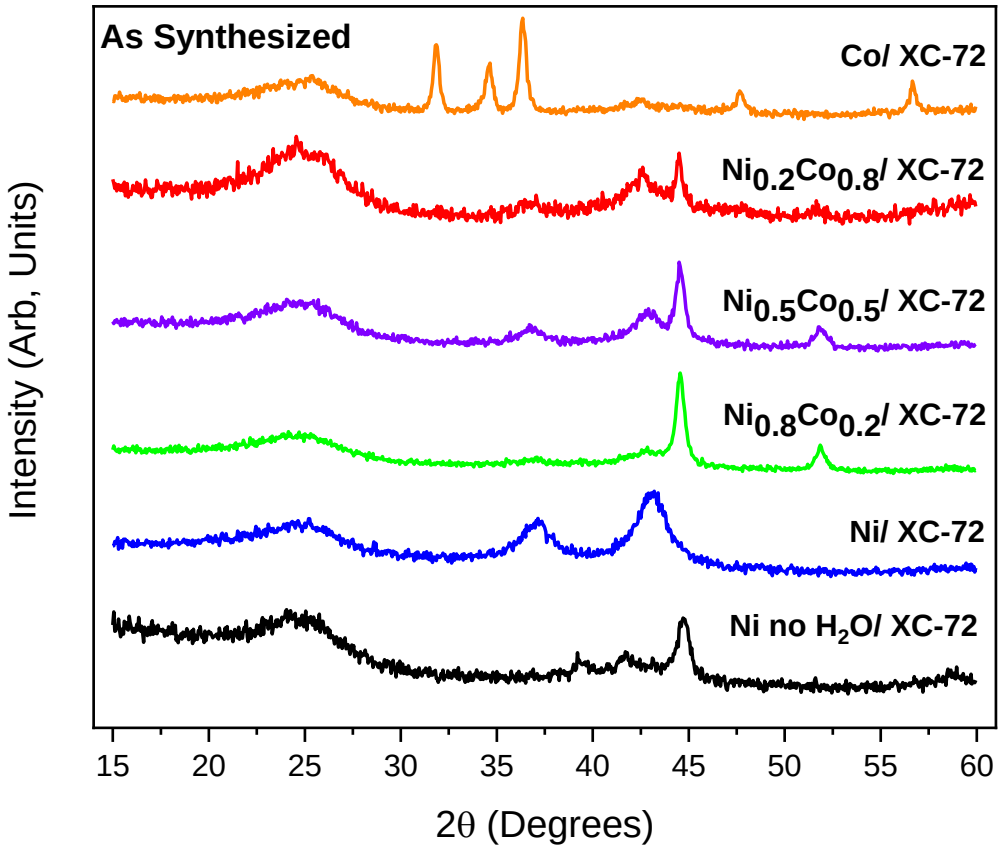

Figure 6.1: Cu K_α X-ray diffraction patterns of various PGM-Free electrocatalyts synthsisized via a single-step modified CVD process. Identified phases in each sample are as follows: (black) Ni/ XC-72 without (w/o) H_2O; HCP Ni, (blue) Ni/ XC-72; NiO, (green) $Ni_{0.8}Co_{0.2}$/ XC-72; FCC Ni, $CoNiO_2$, (purple) $Ni_{0.5}Co_{0.5}$/ XC-72; FCC Ni, $CoNiO_2$, (red) $Ni_{0.2}Co_{0.8}$/ XC-72; CoO, FCC Ni, $CoNiO_2$, and (Orange) Co/ XC-72; CoO. The total weight of the deposted metals are 30% of the total mass of the electrocatalysts.

In the Co/ XC-72 sample, we observe a large amount of hexagonal Wurtzite structured CoO given by peaks at 32.2 (100), 34.2 (002), 36.6 (101), 47.7 (102), and 57.4 (110) $^{o}2\theta$ with small amounts of NaCl Structured CoO[160]. We found a similar crystal structure for the Ni/ XC-72 sample when no water was added to the reaction chamber. Here we find the crystal structure to be HCP Ni with peaks at 39.7 (100), 41.8 (002), 45.1 (101), and 59.0 (102) $^{o}2\theta$. Thermodynamically, both Ni and Co will crystalize in a rock salt (NaCl) structure[161]. However, in the cases where Ni or Co acetate precursors are used, the deposited species can vary based on thermodynamic or kinetic driving forces [161-164].

Golosovsky et al. have well studied this transition in the crystal structure[161]. For $Co(acac)_2$, the decomposition and resultant deposition of the Co nanoparticles can arrange their atoms in a stable rock salt, metastable cubic Zn blend, or hexagonal Wurtzite structure. The rock salt structure is formed when the synthesis method is thermodynamically driven, implying there is a concentration threshold where the synthesis method is more kinetically driven, producing the two metastable conformations. They attribute the change in crystal structure to variations in reaction conditions such as temperature ramp rates, temperature, and time. This rationale holds for the synthesis of HCP Ni via the modified CVD method. In studies using the same $Ni(acac)_2$ sample precursor, HCP Ni was achieved at temperatures of 240-260 ^{o}C under ambient conditions[164].

The temperature ramp rate of the vacuum oven utilized in the modified CVD method varies with respect to the final set temperature. TGA analysis conducted

in a study by Atkinson et al. shows that slow ramp rates lead to a higher onset for various acac precursors' decomposition[98]. Additionally, slower ramp rates may help stabilize the metastable structures in the Ni and CoO nanoparticles. Through slower decomposition rates, the metal concentration increases slower than imposed at high-temperature ramp rates. This can be verified for the PMCVD process by varying and recording the ramp rate of the vacuum oven and analyzing the phase of the the products.

A key observation is that the HCP Ni phase is only achieved without the addition of water to the reaction chamber. The water has been found to help promote the reduction of the metal through the increased oxidation of the acetylacetonate ligand during the deposition process in Pt shown in our studies and Cu-based acetyl precursors in studies by Nasibulin [81, 82]. In this study, we assume that the inclusion of water in the vacuum oven increases the concentration of oxygen in the reaction resulting in the oxidized species found in each sample where water is present due to the highly oxyphilic nature of Ni and Co. A thorough study regarding the role the water plays in the modified CVD process is necessary to disclose its impact on the deposited species.

We begin this study by investigating if we can alter the phase of the samples post-deposition. This was accomplished by conducting thermal treatments to the as-synthesized electrocatalysts at 260 ^{o}C for 1 hour under UHP O_2 and saturated N_2.To saturate the N_2, the gas was sparged into a sealed bottle containing D.I.

water. The rate of gas flow for the two different gases was ~2 sccm. XRD profiles are given in Figure 6.2 for samples treated with O_2 and Saturated N_2, respectively.

In comparing the diffraction patterns of the as-synthesized samples with the samples post-treated with saturated N_2, we do not see any variations in the deposited nanoparticles' phases. However, when the samples are treated under UHP O_2, we do observe changes concerning both the crystallinity and the phase in the samples. One commonality between the three sample sets is found in the Ni/XC-72 sample, where we observe virtually no change to the phase or crystal structure with either heat treatment. In the Bimetallic $Ni_xCo_{(1-x)}$ samples, we see the suppression of the FCC Ni phase due to an increase in the intensity of the $CoNiO_2$ phase. This shift in intensity provides evidence for the role the water plays in the deposition process. As a finite concentration of O_2 is available to produce the $CoNiO_2$ phase is depleted in the as-synthesized bimetallic samples, we see suppression of its associated diffraction peaks. However, when the concentration of O_2 is increased, even post-deposition, we produce more $CoNiO_2$, implying that a higher volume of water in the reaction can drive the product of mixing these organometallic precursors to the $CoNiO_2$ phase.

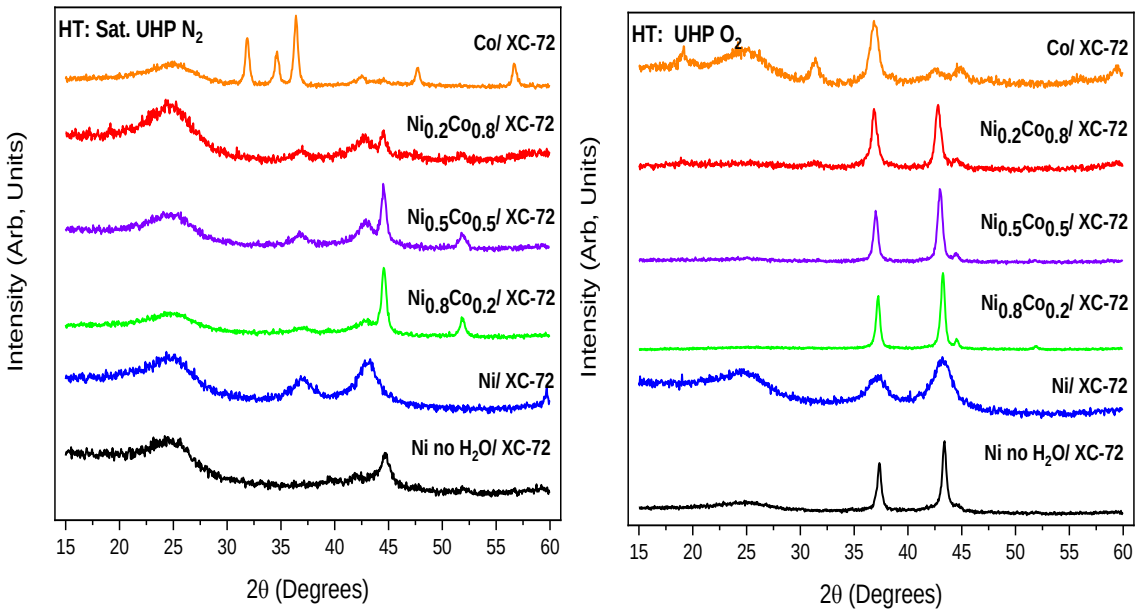

Figure 6.2: Cu Kα X-ray diffraction patterns of various PGM-Free electrocatalyts post-deposition heat treated samples synthesized via a single-step modified CVD process. (Left) Diffraction patterns of post-synthesis heat treatment samples under Saturated UHP N2. Identified phases in each sample are as follows: (black) Ni/ XC-72 without (w/o) H_2O; HCP Ni, (blue) Ni/ XC-72; NiO, (green) $Ni_{0.8}Co_{0.2}$/ XC-72; FCC Ni, $CoNiO_2$, (purple) $Ni_{0.5}Co_{0.5}$/ XC-72; FCC Ni, $CoNiO_2$, (red) $Ni_{0.2}Co_{0.8}$/ XC-72; CoO, FCC Ni, $CoNiO_2$, and (Orange) Co/ XC-72; CoO. (Right) Diffraction patterns of post-synthesis heat treatment samples under UHP O_2. Identified phases in each sample are as follows: (black) Ni/ XC-72 without (w/o) H_2O; NiO, (blue) Ni/ XC-72; NiO, (green) $Ni_{0.8}Co_{0.2}$/ XC-72; FCC Ni, NiO, (purple) $Ni_{0.5}Co_{0.5}$/ XC-72; FCC Ni, $CoNiO_2$, (red) $Ni_{0.2}Co_{0.8}$/ XC-72; Co_3O_4, $CoNiO_2$, and (Orange) Co/ XC-72; Co_3O_4. The total weight of the deposited metals is 30% of the total mass of the electrocatalysts.

This increase in O_2 concentration is also evidenced in the Ni/ XC-72 without water and Co/ XC-72 samples. We now observe crystal structure changes from the metastable hexagonal structures to rock salt NiO with trace amounts of FCC Ni in the Ni/ XC-72 without water sample and Co_3O_4 phase in the Co/ XC-72 sample. This transformation in crystal structure aligns with the aforementioned theories of kinetics or thermodynamics driving the developed structure. The production of the metastable phase is kinetically driven, as mentioned previously. As the concentration of O_2 increased through heat-treatments under UHP O_2, the as-synthisized samples resort to a thermodynamically favorable crystal structure, FCC NiO and Ni in the Ni/ XC-72 without water sample and FCC Co_3O_4 in the Co/ XC-72 sample. The ramp rate of the furnace was set to 2 $^oC*min^{-1}$ to compensate for the low reactant gas flux and prevent any unwanted reduction of the deposited species due to high ramp rates.

The slow ramp rate maintained the phases for the stable crystal structures; however, the metastable crystal structures were able to restructure under the increased temperatures and reactant gases, resulting in the more stable phases observed in Figure 6.2 (Right). Additionally, in the Ni/XC-72 sample, the O_2 aided in increasing the NiO crystallite size defined by the narrow peaks associated with the phase. This shift In crystal structure also provided evidence that the water vapor interacts with the acetylacetonate ligand during decomposition, resulting in variations in oxygen concentrations. We suggest that the oxygen concentration produced from the vaporization of water decreases with its interactions with the acac ligand decomposition byproducts. We assume this because there was no

change in the crystal structure when samples are heat treated with saturated N_2, but consistent changes in each product heat-treated with UHP O_2.

Particle size distributions were investigated using TEM. Figure 6.3 shows the various phased nanoparticles deposited on the XC-72 carbon support. Because of the multitude of phases on the various samples, particle size distributions were omitted for this chapter. The provided diffraction profiles provide a way to decouple the phases based on sizes, such as the difference in the larger FCC Ni nanoparticles' size compared to the smaller $NiCoO_2$ given in Figure 6.3c and d. By measuring the FWHM of the peak associated with the highest atomic density for each phase, we can measure the crystal size by using the Scheerer equation.

Although this method allows us to measure the crystal size for the various phases in the samples, decerning the exact phase of the associated particles within the micrographs is challenging and requiring additional analysis. This process could be done using electron energy loss spectroscopy (EELS) by scanning each particle to identify each nanoparticle's elemental composition. Nonetheless, we are able to observe variations in particle sizes that agree with the range of crystallite sizes for the various phases found in each sample through qualitative analysis.

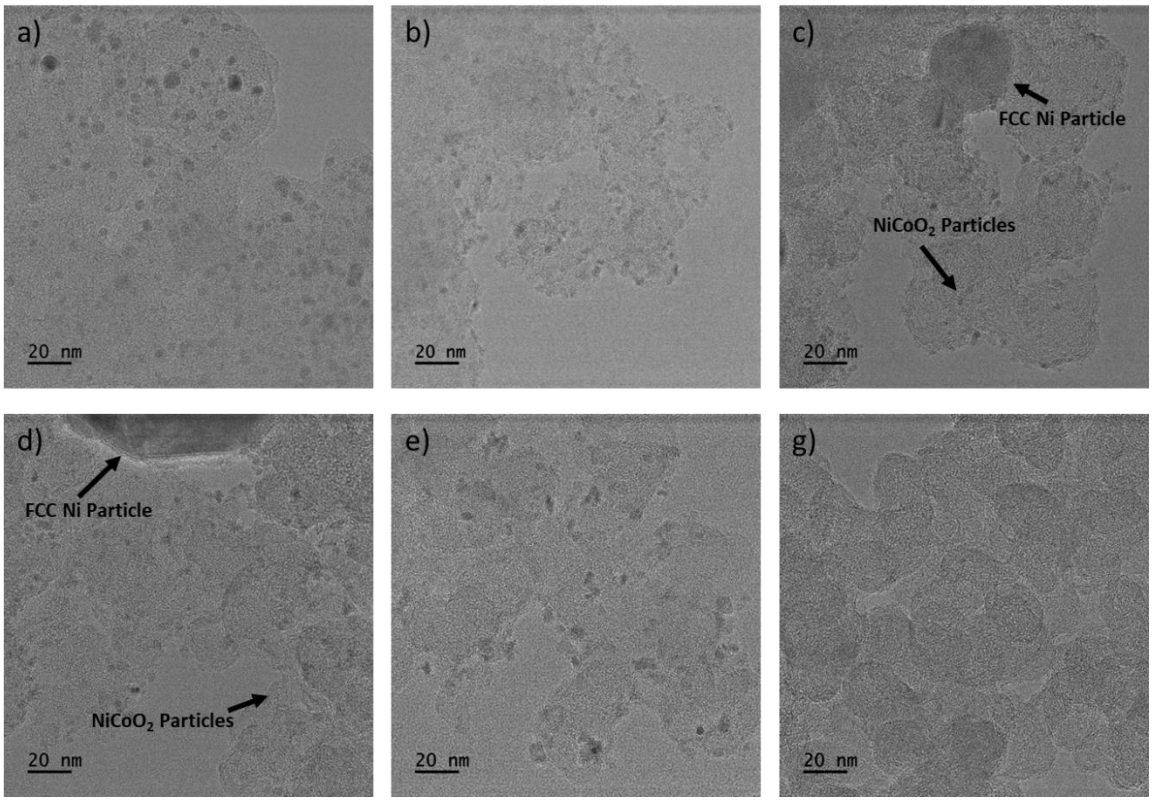

Figure 6.3 TEM Micrographs of a, Ni no H_2O /XC-72; b, Ni/ XC-72; c, $Ni_{0.8}Co_{0.2}$/ XC-72; d, $Ni_{0.5}Co_{0.5}$/ XC-72; e, $Ni_{0.2}Co_{0.8}$/ XC-72; and f, Co/ XC-72. Images show the various particle size distributions with the variations in metal content and reaction conditions. In each sample set, the dark regimes are the metallic nanoparticles deposited on the lighter colored carbon supports. In g, we see large CoO nanoparticles covering the support. If a phase is readily identified based on particle size, it is indicated by arrows in the micrograph.

Electrochemical characterization was conducted on the as-synthesized samples in 0.1 M NaOH. Cyclic voltammetry was employed to stabilize the electrocatalysts. Figure 6.4 (Top) shows the voltammograms for each of the as-synthesized samples. All the samples possessing oxide phases show very low anodic currents. This result is expected as the metallic surfaces are already oxidized. The anodic currents are lowest in the Ni/XC-72 sample and increase with the addition of Co.

Additionally, the water window shifts to lower potentials with the addition of Co. The Ni no H_2O/ XC-72 sample shows features, where oxidation of the Ni surface occurs at the anodic peak found at 0.1-0.5 V vs. RHE, and the reduction of the Ni begins at 0.1 V vs. RHE followed by hydrogen evolution beginning around -0.1 V vs. RHE. These CVs were conducted under N_2, so all oxidation is due to the interactions between the electrolyte and the electrocatalysts. This implies the adsorbate is OH^- resulting in a $Ni(OH)_x$ complex, most likely $Ni(OH)_2$ per Pourbaix diagrams previously published[165].

Polarization plots of the as-synthesized samples were conducted under H_2 to probe the electrocatalytic activity for the hydrogen evolution reaction. Figure 6.3 (Bottom) shows the collected and averaged I vs. V plots over three iterations for each sample. The Co/ XC-72 sample shows the initiation of a reduction peak around -0.3 V vs. RHE where hydrated Co is reduced at these potentials[166]. The Co/XC-72 sample exhibited low currents at higher overpotentials, which prompted only a small portion of the polarization plot for this sample to be presented.

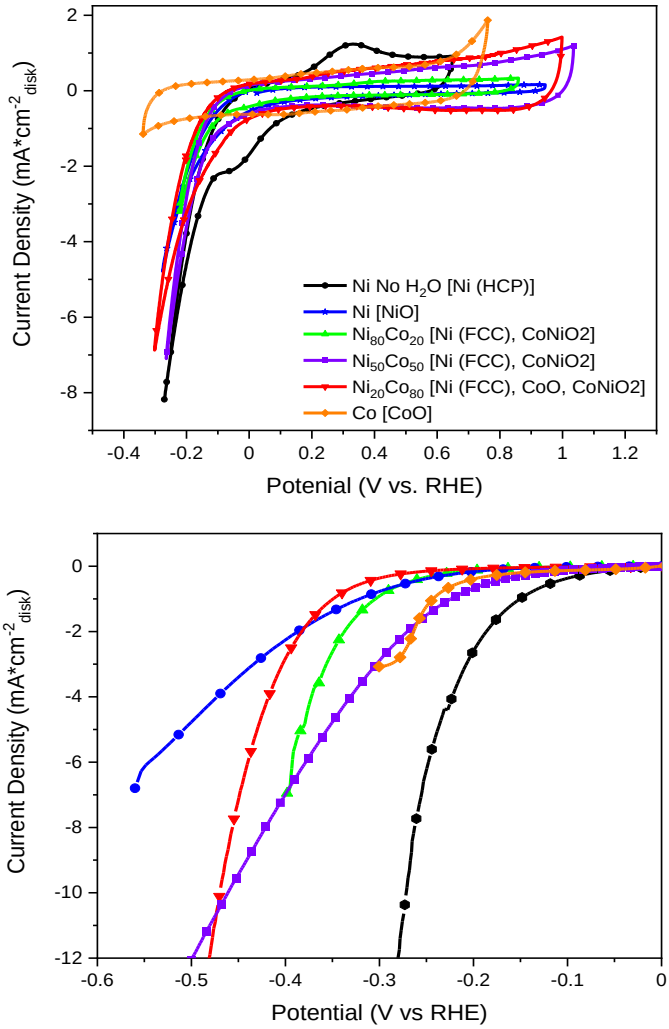

Figure 6.4: Electrochemical characterization of PGM-free electrocatalysts in 0.1M NaOH. (Top) Cyclic voltammograms (CVs)of PGM-free electrocatalysts at a scan rate of 100 $mV*s^{-1}$. (Bottom) iR-corrected polarization plots of PGM-free electrocatalysts conducted at 2 $mV*s^{-1}$. Currents are displayed as the measure current density on a glassy carbon electrode with an active area of 0.1963 cm^2. Scans were swept in the positive voltage direction for each sample. Phases for each sample are included in brackets in the legend.

We calculated the mass activities for each sample at -0.25 V vs. RHE as well as the overpotentials at specific current densities relative to the geometric surface area of the glassy carbon (GC) electrode (0.1963 cm^2) at both 1 and 10 $mA*cm^{-2}$. These results are found in Table 6.1. In comparing the HER activities for these six samples based on both mass activities and achieved currents at measured overpotentials, we find the activities of the electrocatalysts to decrease as follows: Ni no H2O>> $Ni_{0.5}Co_{0.5}$> Co>$Ni_{0.8}Co_{0.2}$>$Ni_{0.2}Co_{0.8}$>Ni. The Ni no H2O/ XC-72 sample exhibited the highest mass activity at 86.58 mA*mg-1 and low overpotentials, generating 1 mA of current normalized by the geometric GC electrode area at an overpotential of 150 mV. This is an increase in activity of over 30% with respect to the current produced by the next highest performing catalyst, $Ni_{0.5}Co_{0.5}$/XC-72.

The Ni no H2O/ XC-72 sample's increased performance is due to the phase of the deposited species. HCP Ni has been extensively studied as a candidate for HER in alkaline by Shao et al., wherein they investigated the increased activities of HCP Ni by characterizing the adsorption energies of H_2O through measuring d band centers on both FCC (111) and HCP Ni (0001) through DFT calculations. Their results indicated a slight increase in d-band centers, increasing the water-binding energy on the HCP Ni surface over the FCP Ni. These results indicate the HCP Ni's proclivity to rapidly adsorbed H_2O initializing the HER. This up-shift in d-band centers results in a lowered energy barrier for the Volmer step enabling the increased kinetics of the HER thermodynamically[167].

Table 6.1: Electrochemical activity of PGM-Free electrocatalysts for the HER. Specific activities were calculated from linear interpolation of the collected polarization plots at 1 and 10 $mA*cm^{-2}$ normalized by the glassy carbon electrode's geometric surface area (0.1963 cm^2).

Catalysts	Loading ($mg*cm^{-2}$)	Overpotentials @Current Density ($mA*cm^{-2}$)	Overpotentials $\underline{\eta}$ (mV)	Mass Activity @ -0.25 V ($mA*mg^{-1}$)
Ni no H_2O	0.072	1	150	-86.58
		10	272	
Ni	0.15	1	321	-2.55
		10	-	
$Ni_{80}Co_{20}$	0.061	1	305	-5.46
		10	-	
$Ni_{50}Co_{50}$	0.103	1	224	-14.54
		10	461	
$Ni_{20}Co_{80}$	0.11	1	350	-1.37
		10	470	
Co	0.15	1	243	-8.21
		10	-	

Although we do not recommend the other deposited phases as promising candidates for HER in alkaline media, these phases have benefits in other areas of research. Nanoparticles of any type possess electrical, magnetic, and optical properties. NiO nanoparticles can be used as a semiconductor with a wide bandgap ranging from 3.6-4.0 eV; studies show that the bandgap increase as particle size decreases[168-170]. $CoNiO_2$ nanoparticles have higher electrical conductivity and specific capacitance than those of the single component nickel or cobalt oxides, making them useful in semiconductors and are also efficient candidates for oxidation of glycerol[171, 172]. HCP CoO possesses paramagnetic properties, unlike its antiferromagnetic counterpart FCC CoO[173]. These mentioned properties are just a brief highlight of the capabilities of these nanoparticles. The described versatility in deposited phase and tunability of crystallinity and phase through various heat treatments mentioned shows the flexibility and utility of the modified CVD method used in this study.

Conclusion

Mono Ni and Co and bimetallic $Ni_xCo_{(1-x)}$ supported on Vulcan XC-72 carbon were synthesized using a single-step modified CVD process. One sample was prepared in the absence of an additional vial of water placed in the reaction chamber. The synthesized samples were characterized using XRD, TEM, and electrochemical characterization techniques. Diffraction analysis provided information on the versatility of the modified CVD method's ability to deposit mixed

phase nanoparticles on carbon supports. When water was included in the system, all samples possessed metal oxide phases, with some entirely reduce rock salt structured Ni nanoparticles in the bimetallic samples. When the water was removed, we produced HCP Ni nanoparticles.

We probed the impact of water through post-synthesis heat treatments under both UHP O_2 and saturated UHP N_2. We observed no change to the phase with saturated N_2 as the reactant gas; however, with the UHP O_2, we saw changes in both phase and crystallinity of the deposited nanoparticle. The two synthesized phases of merit in this study were the hexagonal Wurtzite structured CoO found in the Co/ XC-72 sample, and HCP Ni found in the Ni no H_2O/ XC-72 sample. The generation of these structures is assumed to be kinetically driven, wherein the ramp rate of the vacuum oven, the concentration of metal-organic salt precursor, and deposition time drive the stability of these metastable structures. Additionally, TEM analysis corroborated the variations in crystallite size through qualitative particle size analysis, where we observed variations in the nanoparticles deposited on the carbon support. We further reiterate that a qualitative analysis of the deposited nanoparticles by identifying the phase of each individual particle would require additional characterization techniques outside of this study's specific scope.

Lastly, through electrochemical characterization, we determined the activities of the as-synthesized samples for the HER. We measured the highest activities in the Ni no H_2O/ XC-72 sample, owing to its high mass activity as well

as its ability to generate moderate currents at the lowest overpotentials. Due to the various metal oxides present in the other samples, HER activities are suppressed as active sites are restricted by the addition of oxygen in the catalyst crystal structure. These materials can be advantageous in other fields, such as use in superconductors as well as in applications where tunable optical or magnetic properties are desired. Though findings in previous chapters, where we investigate particle size as a function of reaction conditions, we can assume that these nanoparticles' size can also be tuned, resulting in variations in their phase, band gaps, magnetic and optical properties. These results are the initial steps to developing a better understanding of the deposition of transition metals through this modified CVD method.

CHAPTER VII
CONCLUSION

Controlled synthesis methods to prepare electrocatalysts for fuel cells and electrolyzers are imperative to increase their performance and lower these devices' overall cost. Chemical vapor deposition enables the use of inexpensive organometallic salt precursors. Additionally, the use of these precursors in the low cost PMCVD method provides additional aide to efforts to lower device costs. Furthermore, through this study, we identify methods to tune both the chemical and physical properties of electrocatalysts prepared through the modified CVD process in a controlled manner. Due to this increased control, we show several ways to improve hydrogen kinetics in alkaline media, increasing this method's viability to produce electrocatalyst for the hydrogen oxidation (HOR) and evolution reactions (HER) in alkaline media.

In Chapter 2, we prepared three Pt/ C samples with metal loadings of 10, 30, and 50 wt% Pt using the PMCVD method. We measured this method's metal recovery efficiency through a mass balance, measuring an average metal recovery rate of ~97%. The deposited nanoparticles' average particle size was 2.9 nm, with crystallite sizes varying from 2-3.3 nm. The Pt nanoparticles were fully reduced through the single-step deposition process verifying the reaction temperature and pressure of 210 ^{o}C and 0.28 kPa, respectively, are sufficient to oxidize the acac ligand of the organometallic precursor fully. By analyzing the variations in particle size as a function of metal concentration, we developed rate laws for both the nanoparticles' nucleation and growth. These rates are linear in that an increase in metal content will lead to larger nanoparticles. We provide a mechanism to

describe the deposition mechanism where growth and agglomeration occur after nucleation sites are filled. This is the first study showing the ability to control particle size via the PMCVD method.

Because we achieved metallic nanoparticles at the established reaction temperature and pressure, we were motivated to investigate the impact varying these parameters would have on the deposited nanoparticles. Chapter 3 discusses a parametric study where we varied the temperature from 185- 235 ^{o}C and initial pressure from -.18- 0.38 kPa, utilizing 210 ^{o}C and 0.28 kPa as the center point. We found no variation in phase between the samples and observed no evidence of organics deposited on the metal surface as artifacts of the decomposition process. Variations in physical properties, namely crystallite size, and microstrain were observed. We saw an increase in particle size and minimal strain on the crystal structure at the central temperature and pressure. Most of the other samples exhibited negative microstrain, implying compressed crystallites.

In investigating the electrochemical activities for the HOR/ HER, we studied the samples at the parameter extremes (high and low) and compared the results to the sample prepared at the established temperature and pressure (mid). We found similar activities in the samples at the extremes and increased activity in the mid samples through electrochemical characterization methods. We attribute the higher activities to the minimal strain imposed on the crystallite, aiding in the adsorption and desorption of reactants and product, respectively, for both the HER

and HOR. This study further describes the increased control over both physician and electrochemical properties achieved using the PMCVD method.

In Chapter 4, we extended our study to bimetallic catalyst by synthesizing XC-72 carbon-supported $Pt_xNi_{(1-x)}$ and $Pt_xRu_{(1-x)}$ catalyst where x equaled 0.7, 0.8, and 0.9. The total metal loading in these samples was 30%. The diameters of the deposited nanoparticles ranged from 2-3 nm. We evaluated the degree of alloying for each sample and showed the ability to alloy similarly structured metals in the $Pt_xNi_{(1-x)}$, where each of these metals has an FCC crystal structure. Here we achieve a high degree of alloying across the variations in x. When analyzing the $Pt_xRu_{(1-x)}$ catalyst, we see small amounts of alloying with no trend in the degree of alloying with the addition of the noble metal Ru.

We measured an increase in catalytic activity with the addition of these oxyphilic metals per the bifunctional mechanism through electrochemical characterization. The $Pt_xRu_{(1-x)}$ samples measured a steady increase in both exchange current density and specific activities with an increase in Ru content. In the $Pt_xNi_{(1-x)}$ samples, we measured the highest actives in the sample with the lowest Ni content. The activity decreased with the further addition of Ni. we Attribute these variations in activities between the two sample sets to the difference in the nobility of the added metal. The addition of Ru offers the ability to adsorb hydrogen under low overpotentials, lowering the energy barrier for the Volmer step to proceed. In the Ni samples, we assume the development of a passivation layer

of oxide/ hydroxide that increased with Ni content due to the metals increased oxyphilic nature restricting the access of reactants to the catalytic surface.

After investigating the impacts of metal content, reaction parameters, and alloying capability of similar and mixed crystal structure metals, we investigated the impact of varying the carbon supports' properties on the PMCVD method. We deposited 30 wt% Pt on Vulcan XC-72, Acetylene Black (AB), and Graphitized Nanoplatelets (GNP). The surface areas and degrees of graphitization of these supports differed in AB<XC-72<GNP. The deposited nanoparticles ranged from ~2-4 nm in diameter and grew with a decrease in surface area. These results corroborated our finding in Chapter 2, where the rate law for nucleation is a function of nucleation sites which is closely tied to the materials surface area. This provides a third way to control the particle size and can be employed when support material properties are negligible or when the support's surface area can be affected by thermal treatments.

The three samples' electrochemical surface areas followed the trend regarding nanoparticle size in that Pt/ GNP has the largest ECSA and Pt/ AB the smallest. When we measured these catalysts' electrochemical activity for the HER/HOR, we saw performance increases were activities on Pt/ GNP< XC-72< AB. We determined the increased performance was due to the hydrophobicity of Acetylene Black, promoting the removal of H_2 gas from the electrode surface for the HER resulting in increased H_2 concentrations promoting the HOR. We also observed an irregular "bean-like" shape of the nanoparticles deposited on AB. This

sparked intrigue as to the role water plays in the deposition process. In this case, we assume the water vapor interacts with the carbon support during the deposition process resulting in the unique shape of nanoparticles deposited on AB.

This work concluded with an investigation of Mono Ni and Co and bimetallic $Ni_xCo_{(1-x)}$ supported on Vulcan XC-72. Monometallic samples exhibited single phases, whereas we observed multiple phases in the bimetallic samples with varying degrees of crystallinity between the deposited phases. The deposited nanoparticles ranged from 3.5-23.8 nm in diameter. When water was included in the deposition process, the deposited species were metal oxides. In the one Ni sample where water was not included, the phase produced was metastable hexagonal Ni. We observed a similar hexagonal Wurtzite structured CoO found in the Co/ XC-72 sample. These samples prompt the idea that the PMCVD process is kinetically driven at the given parameters, wherein the ramp rate of the vacuum oven, the concentration of metal-organic salt precursor, and deposition time drive these metastable structures' stability.

We begin investigating the impact water has on the deposition process by conducting heat treatments of the as-synthesized samples under UHP O_2 and saturated UHP N_2. This process simulates the various conditions the reaction chamber could be in during the growth process of the PMCVD method of high oxygen concentrations or high-water vapor concentrations. Under saturated UHP N_2, we observed no change in phase or crystallinity. Under O_2, each sample experienced a change of some type to include the restructuring of the metastable

hexagonal Ni and CoO to FCC crystal structures and a selective increase in crystallinity for the $CoNiO_2$ phase found in the bimetallic samples. This alludes to a way to selectively deposit desired phases during the deposition process. Additionally, the phase change provides evidence that the water vapor plays a pivotal role in the alloying and crystal growth process of the PMCVD method.

Through electrochemical characterization of these transition metal nanoparticles, we identify the HCP structured Ni phase found in the Ni no H_2O/ XC-72 sample showed the highest activity for the HER. This is due to its increased water binding energy achieved through the HCP crystallites' atomic structure. Because the other samples contained metal oxides, similar phenomena of reactant blocking in Chapter 4 lowers their activities. We close this study by presenting other fields of study where these metal oxide nanoparticles can play a role due to their inherent electronic, optical, and magnetic properties, further describing the versatility of the PMCVD to produce highly dispersed nanoparticles useful in a myriad of applications.

REFERENCES

1. LLNL. Energy_US_2019.png (4873×2831) Sankey Plot of U.S. Energy Consumption 2019 https://flowcharts.llnl.gov/ (accessed Mar 21, 2021).
2. Barbir, F.; Gómez, T. Efficiency and Economics of Proton Exchange Membrane (PEM) Fuel Cells. *Int. J. Hydrogen Energy* 1997, *22* (10–11), 1027–1037.
3. Borup, R.; Meyers, J.; Pivovar, B.; Kim, Y. S.; Mukundan, R.; Garland, N.; Myers, D.; Wilson, M.; Garzon, F.; Wood, D.; et al. Scientific Aspects of Polymer Electrolyte Fuel Cell Durability and Degradation. 2007.
4. Weber, A. Z.; Borup, R. L.; Darling, R. M.; Das, P. K.; Dursch, T. J.; Gu, W.; Harvey, D.; Kusoglu, A.; Litster, S.; Mench, M. M.; et al. A Critical Review of Modeling Transport Phenomena in Polymer-Electrolyte Fuel Cells. *J. Electrochem. Soc.* 2014, *161* (12), 1254–1299.
5. Weber, A. Z.; Newman, J. Modeling Transport in Polymer-Electrolyte Fuel Cells. 2004.
6. Billy, E.; Maillard, F.; Morin, A.; Guetaz, L.; Emieux, F.; Thurier, C.; Doppelt, P.; Donet, S.; Mailley, S. Impact of Ultra-Low Pt Loadings on the Performance of Anode/Cathode in a Proton-Exchange Membrane Fuel Cell. *J. Power Sources* 2010, *195* (9), 2737–2746.
7. Holdcroft, S. Fuel Cell Catalyst Layers: A Polymer Science Perspective. *Chemistry of Materials*. 2014, pp 381–393.

8. Wee, J. H. Applications of proton exchange membrane fuel cell systems. *Renewable and Sustainable Energy Reviews* vol. 11 1720–1738 (2007).
9. Millet, P. *et al.* PEM water electrolyzers: From electrocatalysis to stack development. *Int. J. Hydrogen Energy* 35, 5043–5052 (2010).
10. Ulleberg, Ø. Modeling of advanced alkaline electrolyzers: A system simulation approach. *Int. J.*
11. David, M., Ocampo-Martínez, C. & Sánchez-Peña, R. Advances in alkaline water electrolyzers: A
12. Turner, J. *et al.* Renewable hydrogen production. *Int. J. Energy Res.* 32, 379–407 (2008).review.
13. Vol ; Bouallou, & Werkoff, C. Dry reforming of methane-review of feasibility studies. in *Chemical Engineering Transactions* vol. 29 163–168 (2012).*Journal of Energy Storage* vol. 23 392–403 (2019).*Hydrogen Energy* 28, 21–33 (2003).
14. de Frank Bruijn, A. & Janssen, G. J. M. PEM Fuel Cell Materials: Costs, Performance and Durability. in *Fuel Cells* 249–303 (Springer New York, 2013). doi:10.1007/978-1-4614-5785-5_9.
15. Firouzjaie, H. A. & Mustain, W. E. Catalytic Advantages, Challenges, and Priorities in Alkaline Membrane Fuel Cells. *ACS Catalysis* vol. 10 225–234 (2020).
16. Carrette, L., Friedrich, K. A. & Stimming, U. Fuel Cells - Fundamentals and Applications. *Fuel Cells* 1, 5–39 (2001).

17. Ruiz-Camacho, B., Martínez-González, J. H., González-Huerta, R. G. & Tufiño-Velázquez, M. Kinetic study of oxygen reduction reaction and PEM fuel cell performance of Pt/TiO2-C electrocatalyst. in *International Journal of Hydrogen Energy* vol. 39 16731–16739 (Elsevier Ltd, 2014).
18. Strickland, K. *et al.* Highly active oxygen reduction non-platinum group metal electrocatalyst without direct metal-nitrogen coordination. *Nat. Commun.* 6, 1–8 (2015).
19. Piana, M., Catanorchi, S. & Gasteiger, H. A. Kinetics of Non-Platinum Group Metal Catalysts for the Oxygen Reduction Reaction in Alkaline Medium. *ECS Trans.* 16, 2045–2055 (2019).
20. Wu, G., More, K. L., Johnston, C. M. & Zelenay, P. High-performance electrocatalysts for oxygen reduction derived from polyaniline, iron, and cobalt. *Science (80-.).* 332, 443–447 (2011).
21. Wang, B. Recent development of non-platinum catalysts for oxygen reduction reaction. *Journal of Power Sources* vol. 152 1–15 (2005).
22. Chandran, P., Ghosh, A. & Ramaprabhu, S. High-performance Platinum-free oxygen reduction reaction and hydrogen oxidation reaction catalyst in polymer electrolyte membrane fuel cell. *Sci. Rep.* 8, 1–11 (2018).
23. Jai, Q.; Liu, E.; Li, J.; Mukerjee, S. Current Understanding of the Sluggish Kinetics of Hydrogen Evolution and Oxidation in Base. Current Opinions in Electrochemistry 2018, 12:209-217

24. Durst, J.; Siebel, A.; Simon, S.; Hasche, F.; Herranz, J.; Gastiger, H. A. New Insights into the Electrochemical Hydrogen Oxidation And Evolution Reaction Mechanism. *Energy Environ. Sci.*, 2014,7, 2255-2260
25. Davydova, E.; Mukerjee, S.; Jaouen, F.; Dekel, D. Electrocatalysts for Hydrogen Oxidation in Alkaline Electrolytes. ACS Catal. 2018, 8, 6665-6690
26. Gottesfeld, S.; Dekel, D.; Page; M.; Bae, C.; Yan, Y.; Zelenay, P.; Kim, Y. Anion Exchange Membrane Fuel Cells: Current Status and Remaining Challenges; Journal of Power sources 375 (2018) 170-184
27. Mustain, W. & Pivovar, B. catalysts Catalysts for Polymer Membrane Fuel Cells. 10, 86 (2020).
28. Sheng, W.; Gastiger, H.; Shao-Horn, Y. Hydrogen oxidation and evolution reaction kinetics on Platinum: Acid vs Alkaline electrolytes
29. Barbir, F. *PEM Fuel Cells : Theory and Practice*. *PEM Fuel Cells : Theory and Practice* (2012).
30. Zheng, J., Nash, J., Xu, B. & Yan, Y. Perspective—Towards Establishing Apparent Hydrogen Binding Energy as the Descriptor for Hydrogen Oxidation/Evolution Reactions. *J. Electrochem. Soc.* 165, H27–H29 (2018).
31. Zheng, J.; Sheng, W.; Zhuang, Z.; Xu, B.; Yan, Y. Universal Dependence of Hydrogen Oxidation and Evolution Activity of Platinum-Group Metals on pH and Hydrogen Binding Energy Sci. Adv. 2016; 2: e1501602

32. Sheng W , Myint M , Chen JG , Yan Y : Correlating The Hydrogen Evolution Reaction Activity In Alkaline Electrolytes With The Hydrogen Binding Energy On Monometallic Surfaces . Energy Environ Sci 2013, 6 :1509–1512
33. Shinaguwq, T.; Garcia-Esperza, A.; Takanable, K. Insight on Tafel Slopes form a Microkinetic Analysis of Aqueous Electrocatalysts for Energy Conversion. Scientific Reports volume 5, Article number: 13801 (2015)
34. Strmcnik D , Uchimura M , Wang C , Subbaraman R , Danilovic N , van der V , Paulikas AP , Stamenkovic VR , Markovic NM : Improving the Hydrogen Oxidation Reaction Rate by Promotion of Hydroxyl Adsorption . Nat Chem 2013, 5 :300–306 .
35. Li, J,; Goshal, M.; Bates, M.; Miller, V.; Staviski, E.; Attenkofer, K.; Mujerjee, S.; Ma, Z.; Jai, Q. Experimental Proof of the Bifunctional Mechanism for the Hydrogen Oxidation in Alkaline Media. Angew. Chem. Int. Ed. 2017, 26, 15594-15558
36. Subbaraman R , Tripkovic D , Chang K-C , Strmcnik D , Paulikas AP , Hirunsit P , Chan M , Greeley J , Stamenkovic V , Markovic NM : Trends in activity for the water electrolyser reactions on 3d M (Ni, Co, Fe, Mn) hydr(oxy) oxide catalysts . Nat Mater 2012, 11 :550–557.
37. Ramaswamy N , Ghoshal S , Bates MK , Jia Q , Li J , Mukerjee S : Hydrogen oxidation reaction in alkaline media: Relationship between electrocatalysis and electrochemical double-layer structure . Nano Energy 2017, 41:765–771.

38. Ledezma-Yanez I , Wallace WDZ , Sebastián-Pascual P , Climent V , Feliu JM , Koper MTM : Interfacial water reorganization as a pH-dependent descriptor of the hydrogen evolution rate on platinum electrodes . Nat Energy 2017, 2 :17031.

39. Chen X , McCrum IT , Schwarz KA , Janik MJ , Koper MTM : Co-adsorption of Cations as the cause of the apparent ph dependence of hydrogen adsorption on a stepped platinum single-crystal electrode . Angew Chem Int Ed 2017, 56 :15025–15029 .

40. Van der Niet MJ , Garcia-Araez N , Hernández J , Feliu JM , Koper MT : Water dissociation on well-defined platinum surfaces: The electrochemical perspective . Catal Today 2013, 202 :105–113 .

41. L. Ershuai, L. Jingkun, J. Li, D. Huong Thi Thanh, L. Zeyan, Z. Zipeng, H. Yu, A. Kuzhikalail. M., M. Sanjeev, J. Qingying, Unifying the alkaline hydrogen evolution/oxidation reactions kinetics by identifying the roles of hydroxyl-water-cation adducts chemrxiv , 2018.

42. Strmcnik, D.; Kodama, K.; van der Vliet, D.; Greeley, J.; Stamenkovic, VR.; Markovic, N. M. : The role of non-covalent interactions in electrocatalytic fuel-cell reactions on platinum . Nat Chem 2009, 1 :466 .

43. Mehta, V.; Cooper, J. S. Review and Analysis of PEM Fuel Cell Design and Manufacturing. *J. Power Sources* 2003, *114* (1), 32–53.

44. Shao, Y.; Yin, G.; Gao, Y. Understanding and Approaches for the Durability Issues of Pt-Based Catalysts for PEM Fuel Cell. *J. Power Sources* 2007, *171* (2), 558–566.

45. Yu, X.; Ye, S. Recent Advances in Activity and Durability Enhancement of Pt/C Catalytic Cathode in PEMFC: Part I. Physico-Chemical and Electronic Interaction between Pt and Carbon Support, and Activity Enhancement of Pt/C Catalyst. *J. Power Sources* 2007, *172* (1), 133–144.

46. Eftekhari, A. Electrocatalysts for Hydrogen Evolution Reaction. *Int. J. Hydrogen Energy* 2017, *42* (16), 11053–11077.

47. Dekel, D. Review of Cell Performance in Anion Exchange Membrane Fuel Cells. Journals of Power sources 375 (2018) 158-169

48. Gasteiger, H. A.; Kocha, S. S.; Sompalli, B.; Wagner, F. T. Activity Benchmarks and Requirements for Pt, Pt-Alloy, and Non-Pt Oxygen Reduction Catalysts for PEMFCs. *Appl. Catal. B Environ.* 2005, *56* (1–2), 9–35.

49. St. John, S.; Atkinson, R. W.; Unocic, R. R.; Zawodzinski, T. A.; Papandrew, A. B. Ruthenium-Alloy Electrocatalysts with Tunable Hydrogen Oxidation Kinetics in Alkaline Electrolyte. *J. Phys. Chem. C* 2015, *119* (24), 13481–13487.

50. Sheng, W.; Bivens, A. P.; Myint, M.; Zhuang, Z.; Forest, R. V.; Fang, Q.; Chen, J. G.; Yan, Y. Non-Precious Metal Electrocatalysts with High Activity

for Hydrogen Oxidation Reaction in Alkaline Electrolytes. *Energy Environ. Sci.* 2014, *7*, 1719– 1724

51. Zadic, A.; Dubau, L.; Sergent, N.; Berthome, G.; Chatenet, M. huge instability of Pt/C Catalysts in Alkaline Medium. ACS Catal. 2015, 5, 4819-4824
52. Macauley, N. *et al.* Carbon Corrosion in PEM Fuel Cells and the Development of Accelerated Stress Tests. *J. Electrochem. Soc.* 165, F3148–F3160 (2018).
53. Garland, N.; Benjamin, T.; Kopasz, J. DOE Fuel Cell Program: Durability Technical Targets and Testing Protocols. In *ECS Transactions*; ECS, 2007; Vol. 11, pp 923–931.
54. Castanheira, L.; Dubau, L.; Maillard, F. Accelerated Stress Tests of Pt/HSAC Electrocatalysts: An Identical-Location Transmission Electron Microscopy Study on the Influence of Intermediate Characterizations. *Electrocatalysis* 2014, *5* (2), 125–135.
55. Chevallier, L.; Bauer, A.; Cavaliere, S.; Hui, R.; Rozière, J.; Jones, D. J. Mesoporous Nanostructured Nb-Doped Titanium Dioxide Microsphere Catalyst Supports for PEM Fuel Cell Electrodes. *ACS Appl. Mater. Interfaces* 2012, *4* (3), 1752–1759.
56. Huang, S.-Y.; Ganesan, P.; Popov, B. N. Electrocatalytic Activity and Stability of Niobium-Doped Titanium Oxide Supported Platinum Catalyst for Polymer Electrolyte Membrane Fuel Cells. *Appl. Catal. B Environ.* 2010, *96* (1–2), 224–231.

57. Huang, S.-Y.; Ganesan, P.; Park, S.; Popov, B. N. Development of a Titanium Dioxide-Supported Platinum Catalyst with Ultrahigh Stability for Polymer Electrolyte Membrane Fuel Cell Applications. *J. Am. Chem. Soc. 131* (39), 13898–13899, 2009

58. Shao, Y.; Liu, J.; Wang, Y.; Lin, Y. Novel Catalyst Support Materials for PEM fuel cells: Current Status and Future Prospects. *J. Mater. Chem. 19* (1), 46–59, 2009

59. Ho, V. T. T.; Pan, C. J.; Rick, J.; Su, W. N.; Hwang, B. J. Nanostructured Ti0.7Mo0.3O2support Enhances Electron Transfer to Pt: High-Performance Catalyst for Oxygen Reduction Reaction. *J. Am. Chem. Soc.* 2011, *133* (30), 11716–11724.

60. Ritala, M. & Leskela, M. *Handbook of Thin Films*. *Handbook of Thin Films* vol. 1 Chapter 2 (Elsevier, 2002).

61. Yang, H., Chen, Y. & Qin, Y. Application of atomic layer deposition in fabricating high-efficiency electrocatalysts. *Chinese Journal of Catalysis* vol. 41 227–241 (2020).

62. Christensen, S. Feng, H.; Libera, J.; Guo, N.; Miller, J.; Stair, P.; Elam, J. Supported Ru−Pt Bimetallic Nanoparticle Catalysts Prepared by Atomic Layer Deposition Nano Lett. 2010, 10, 8, 3047-3051

63. Cheng, N.; Stambula, S.; Wang, D.; Banis, M.; Liu, J.; Riese, A.; Xaio, B.; Li, R.; Sham, T.; Liu, L.; Botton, G.; Sun, X. Platinum single-atom and cluster catalysis of the hydrogen evolution reaction. Nat Commun 7, 13638 (2016).

64. Wang, C.; Chi, M.; Li, D.; Strmcnik, D.; Van Der Vliet, D.; Wang, G.; Komanicky, V.; Chang, K.-C.; Paulikas, A. P.; Tripkovic, D.; et al. Design and Synthesis of Bimetallic Electrocatalyst with Multilayered Pt-Skin Surfaces. *J. Am. Chem. Soc* 2011, *133*, 14396–14403.

65. Liu, C., Wang, C., Kei, C., Hsueh, Y. & Perng, T. Atomic Layer Deposition of Platinum Nanoparticles on Carbon Nanotubes for Application in Proton-Exchange Membrane Fuel Cells. *Small* 5, 1535–1538

66. Cheng, N., Shao, Y., Liu, J. & Sun, X. Electrocatalysts by atomic layer deposition for cell applications. *Nano Energy* 29

67. Song, Z. *et al.* Origin of achieving the enhanced activity and stability of Pt electrocatalysts with strong metal-support interactions via atomic layer deposition. *Nano Energy* 53, 716–725 (2018)., 220–242 (2016).2009).

68. Ho, T. A. *et al.* Metallic Ni3S2 Films Grown by Atomic Layer Deposition as an Efficient and Stable Electrocatalyst for Overall Water Splitting. *ACS Appl. Mater. Interfaces* 10, 12807–12815 (2018).

69. Dameron, A. A. *et al.* Aligned carbon nanotube array functionalization for enhanced atomic layer deposition of platinum electrocatalysts. *Appl. Surf. Sci.* 258, 5212–5221 (2012).

70. Naidoo, S.; Naidoo, Q.; Musil, E.; Linkov, V.; Vaivars, G. Precipitation and Calcination Synthesis Methods Forming Nano-Sized Platinum Catalytic Particles for Methanol and Hydrogen Oxidation. *Adv. Nat. Sci. Nanosci. Nanotechnol.* 2013, *4* (1).

71. Oh, A.,Jin, Y.; Hwang, H.; Baik, H.; Kim, B.; Hoon Joo, S.; Lee, K. Rational design of Pt–Ni–Co ternary alloy nanoframe crystals as highly efficient catalysts toward the alkaline hydrogen evolution reaction Nanoscale, 2016,8, 16379-16386

72. Abbas, S.A., Kim, S., Iqbal, M.I. et al. Synergistic effect of nano-Pt and Ni spine for HER in alkaline solution: hydrogen spillover from nano-Pt to Ni spine. Sci Rep 8, 2986 (2018) doi:10.1038/s41598-018-21396-9

73. Zhuang, Z., Giles, S., Zheng, J. et al. Nickel supported on nitrogen-doped carbon nanotubes as hydrogen oxidation reaction catalyst in alkaline electrolyte. Nat Commun 7, 10141 (2016) doi:10.1038/ncomms10141

74. Wang, D., Xie, T. & Li, Y. Nanocrystals: Solution-based synthesis and applications as nanocatalysts. *Nano Res.* 2, 30–46 (2009).

75. Porter, N. S., Wu, H., Quan, Z. & Fang, J. Shape-control and electrocatalytic activity-enhancement of pt-based bimetallic nanocrystals. *Acc. Chem. Res.* 46, 1867–1877 (2013).

76. Fu, G. *et al.* One-pot, water-based and high-yield synthesis of tetrahedral palladium nanocrystal decorated graphene. *Nanoscale* 5, 8007–8014 (2013).

77. da Silva, A. G. M. *et al.* Pd-based nanoflowers catalysts: controlling size, composition, and structures for the 4-nitrophenol reduction and BTX oxidation reactions. *J. Mater. Sci.* 51, 603–614 (2015).

78. Guterman, V. E., Pakharev, A. Y. & Tabachkova, N. Y. Microstructure and size effects in Pt/C and Pt3Ni/C electrocatalysts synthesized in solutions based on binary organic solvents. *Appl. Catal. A Gen.* 453, 113–120 (2013).
79. Pinkas, J.; Huffman, J. C.; Baxter, D. V.; Chisholm, M. H.; Caulton, K. G. Mechanistic Role of H2O and the Ligand in the Chemical Vapor Deposition of Cu, Cu2O, CuO, and Cu3N from Bis (1,1,1,5,5,5-Hexafluoropentane-2,4-Dionato) Copper (II). *Chem. Mater.* 1995, *7* (8), 1589–1596.
80. Soofivand, F.; Salavati-Niasari, M. Novel Solvent-Less Synthesis of CuO Nanoparticles by Using Sublimated Precursors. *Mater. Lett.* 2013, *106*, 83–86.
81. Nasibulin, A. G.; Ahonen, P. P.; Richard, O.; Kauppinen, E. I.; Altman, I. S. Copper and Copper Oxide Nanoparticle Formation by Chemical Vapor Nucleation from Copper (II) Acetylacetonate. *J. Nanoparticle Res.* 2001, *3* (Ii), 385–400.
82. Nasibulin, A. G.; Richard, O.; Kauppinen, E. I.; Brown, D. P.; Jokiniemi, J. K.; Altman, I. S. Nanoparticle Synthesis by Copper (II) Acetylacetonate Vapor Decomposition in the Presence of Oxygen. *Aerosol Sci. Technol.* 2002, *36* (8), 899–911.
83. Arndt, J.; Klippe, L.; Stolle, R.; Wahl, G.; Arndt, J.; Klippe, L.; Stolle, R.; Wahl, G. Deposition of Platinum from Bis (Acetylacetonato) Platinum (II). *J. Phys. IV* 1995,

84. Thurier, C.; Doppelt, P. Platinum OMCVD Processes and Precursor Chemistry. *Coord. Chem. Rev.* 2008, *252* (1–2), 155–169.

85. Morozova B., N.; Zharkova I., G.; Semyannikov P., P.; Sysoev V., S.; Igumenov K., I.; Fedotova E., N.; Gelfond V., N. Vapor Pressure of Precursors for CVD on the Base of Platinum Group Metals. *J. Phys. IV France*. j. Phys 2001, pp Pr3-609-Pr3-616.

86. Kim, H.; Moon, S. H. Chemical Vapor Deposition of Highly Dispersed Pt Nanoparticles on Multi-Walled Carbon Nanotubes for Use as Fuel-Cell Electrodes. *Carbon N. Y.* 2011, *49* (4), 1491–1501.

87. Garcia, J. R. V.; Goto, T. Chemical Vapor Deposition of Iridium, Platinum, Rhodium and Palladium. *Mater. Trans.* 2003, *44* (9), 1717–1728.

88. Gomez, C.; Varges Garcia, J.; Antonio , J.; Cortez,Jacome, M. Pt Nanoparticles on Titania Nanotubes Prepared by Vapor-Phase Impregnation–Decomposition Method. Journal of Alloys and Compounds. (2010), 495. 458-461.

89. Papandrew, A. B.; Atkinson, R. W.; Goenaga, G. A.; Kocha, S. S.; Zack, J. W.; Pivovar, B. S.; Zawodzinski Jr., T. A. Oxygen Reduction Activity of Vapor-Grown Platinum Nanotubes. *J. Electrochem. Soc.* 2013, *160* (8), F848–F852.

90. Pierson, H. O. Handbook of Chemical Vapor Deposition (CVD) | ScienceDirect. https://www.sciencedirect.com/book/9780815514329/handbook-of-chemical-vapor-deposition-cvd.

91. Feng, M. & Puddephatt, R. J. Chemical vapor deposition of macroporous platinum and palladium-platinum alloy films by using polystyrene spheres as templates. *Chem. Mater.* 15, 2696–2698 (2003).

92. Dai, B. *et al.* Rational design of a binary metal alloy for chemical vapour deposition growth of uniform single-layer graphene. *Nat. Commun.* 2, 1–6 (2011).

93. Papandrew, A. B.; Chisholm, C. R. I.; Elgammal, R. A.; Özer, M. M.; Zecevic, S. K. Advanced Electrodes for Solid Acid Fuel Cells by Platinum Deposition on CsH2PO4. *Chem. Mater.* 2011, *23* (7), 1659–1667.

94. Papandrew, A. B.; Chisholm, C. R. I.; Zecevic, S. K.; Veith, G. M.; Zawodzinski, T. A. Activity and Evolution of Vapor Deposited Pt-Pd Oxygen Reduction Catalysts for Solid Acid Fuel Cells. *J. Electrochem. Soc.* 2012, *160* (2), F175–F182.

95. Papandrew, A. B.; Atkinson III, R. W.; Unocic, R. R.; Zawodzinski, T. a. Ruthenium as a CO-Tolerant Hydrogen Oxidation Catalyst for Solid Acid Fuel Cells. *J. Mater. Chem. A* 2015, *3* (7), 3984–3987.

96. Papandrew, A. B.; Atkinson, R. W.; Goenaga, G. A.; Kocha, S. S.; Zack, J. W.; Pivovar, B. S.; Zawodzinski Jr., T. A. Oxygen Reduction Activity of Vapor-Grown Platinum Nanotubes. *J. Electrochem. Soc.* 2013, *160* (8), F848–F852.

97. Babu, S. K.; Atkinson, R. W.; Papandrew, A. B.; Litster, S. Vertically Oriented Polymer Electrolyte Nanofiber Catalyst Support for Thin Film Proton-

Exchange Membrane Fuel Cell Electrodes. *ChemElectroChem* 2015, *2* (11), 1752–1759.

98. Atkinson, R. Vapor Synthesis and Thermal Evolution of Supportless, Metal Nanotubes and Application as Electrocatalysts. *Dr. Diss.* 2015.
99. Garcia, J. R. V.; Goto, T. Chemical Vapor Deposition of Iridium, Platinum, Rhodium and Palladium. *Mater. Trans.* 2003, *44* (9), 1717–1728.
100. Morozova B., N.; Zharkova I., G.; Semyannikov P., P.; Sysoev V., S.; Igumenov K., I.; Fedotova E., N.; Gelfond V., N. Vapor Pressure of Precursors for CVD on the Base of Platinum Group Metals. *J. Phys. IV France*. j. Phys 2001, pp Pr3--609--Pr3--616.
101. Alexeeva, O. K. & Fateev, V. N. Application of the magnetron sputtering for nanostructured electrocatalysts synthesis. *International Journal of Hydrogen Energy* vol. 41 3373–3386 (2016).
102. Weber, M. F., Pataki, L., Venter, R. D. & Dignam, M. J. SPUTTERED FUEL CELL ELECTRODES. in *Advances in Hydrogen Energy* vol. 4 1685–1692 (Pergamon Press, 1984).
103. Hussain, S. *et al.* Pt nanoparticles sputter-deposited on TiO2/MWCNT composites prepared by atomic layer deposition: Improved electrocatalytic activity towards the oxygen reduction reaction and durability in acid media. *Int. J. Hydrogen Energy* 43, 4967–4977 (2018).
104. Smentkowski, V. S. Trends in sputtering. *Progress in Surface Science* vol. 64 1–58 (2000).

105. Thurier, C. & Doppelt, P. Platinum OMCVD processes and precursor chemistry. *Coord. Chem. Rev.* 252, 155

106. Szlachetko, J. *et al.* High energy resolution off-resonant spectroscopy at sub-second time resolution: (Pt(acac)2) decomposition. *Chem. Commun.* 48, 10898–10900 (2012).–169 (2008).

107. Arndt, J., Klippe, L., Stolle, R. & Wahl, G. Deposition of Platinum from Bis(Acetylacetonato)Platinum(II). *Le J. Phys. IV* 05, C5-119-C5-126 (1995).

108. Garcia, J. R. V. & Goto, T. Chemical Vapor Deposition of Iridium, Platinum, Rhodium and Palladium. *Mater. Trans.* 44, 1717–1728 (2003).

109. Meier, J. C. *et al.* Design criteria for stable Pt/C fuel cell catalysts. *Beilstein Journal of Nanotechnology* vol. 5 44–67 (2014).

110. Shao-Horn, Y. *et al.* Instability of supported platinum nanoparticles in low-temperature fuel cells. *Top. Catal.* 46, 285–305 (2007).

111. Cheng, T., Wang, L., Merinov, B. V. & Goddard, W. A. Explanation of Dramatic pH-Dependence of Hydrogen Binding on Noble Metal Electrode: Greatly Weakened Water Adsorption at High pH. *J. Am. Chem. Soc.* 140, 7787–7790 (2018).

112. Kinoshita, K. Particle Size Effects for Oxygen Reduction on Highly Dispersed Platinum in Acid Electrolytes. *J. Electrochem. Soc.* 137, 845–848 (1990).

113. Nesselberger, M., Ashton, S., Meier, J. C., Katsounaros, I., Mayrhofer, K. J. J., & Arenz, M. The particle size effect on the oxygen reduction reaction activity of Pt catalysts: Influence of electrolyte and relation to single crystal

models. *Journal of the American Chemical Society*, *133*(43), 17428–17433 (2011).

114. Durst, J., Simon, C., Siebel, A., Rheinlander, P. J., Schuler, T., Hanzlik, M., Herranz, J., Hasche, F., & Gasteiger, H. A. (Invited) Hydrogen Oxidation and Evolution Reaction (HOR/HER) on Pt Electrodes in Acid vs. Alkaline Electrolytes: Mechanism, Activity and Particle Size Effects. *ECS Transactions*, *64*(3), 1069–1080 (2014).
115. Cullity, B. D. (1956). *Elements of X-Ray Diffraction*.
116. Snyder, R. L., Fiala, J., & Bunge, H. J. (2000). *Defect and Microstructure Analysis by Diffraction*.
117. D'Arrigo JS. Screening of membrane surface charges by divalent cations: an atomic representation. Am J Physiol. 235(3):C109-17 (1978)
118. Davey, Wheeler ”Precision Measurement of the Lattice Constants of Twelve Common Metals” Physical Review. 25 753-761 (1925)
119. Lasia, A. (2019). Mechanism and kinetics of the hydrogen evolution reaction. In *International Journal of Hydrogen Energy* (Vol. 44, Issue 36, pp. 19484–19518). Elsevier Ltd.
120. Shinagawa, T., Garcia-Esparza, A. T. & Takanabe, K. Insight on Tafel slopes from a microkinetic analysis of aqueous electrocatalysis for energy conversion OPEN. *Nat. Publ. Gr.* 23955–6900 (2015)
121. Wang, C. *et al.* Proton Exchange Membrane Fuel Cells with Carbon Nanotube Based Electrodes. *Nano Lett.* 4, 345–348 (2004).

122. Huang, R., Wen, Y. H., Zhu, Z. Z. & Sun, S. G. Pt-Pd bimetallic catalysts: Structural and thermal stabilities of core-shell and alloyed nanoparticles. *J. Phys. Chem. C* 116, 8664–8671 (2012).

123. Hsieh, C. T., Lin, J. Y. & Wei, J. L. Deposition and electrochemical activity of Pt-based bimetallic nanocatalysts on carbon nanotube electrodes. *Int. J. Hydrogen Energy* 34, 685–693 (2009).

124. Wang, D. *et al.* Structurally ordered intermetallic platinum--cobalt core--shell nanoparticles with enhanced activity and stability as oxygen reduction electrocatalysts. *Nat. Mater.* (2013)

125. Kadirgan, F. *et al.* Carbon supported nano-sized Pt-Pd and Pt-Co electrocatalysts for proton exchange membrane fuel cells. *Int. J. Hydrogen Energy* 34, 9450–9460 (2009).

126. Glüsen, A. *et al.* Dealloyed PtNi-Core-Shell Nanocatalysts Enable Significant Lowering of Pt Electrode Content in Direct Methanol Fuel Cells. *ACS Catal.* 9, 3764–3772 (2019).

127. Fugier, P. *et al.* PtxCoy Catalysts Degradation in PEFC Environments: Mechanistic Insights II. Preparation and Characterization of Particles with Homogeneous Composition. *J. Electrochem. Soc.* 157, B943–B951 (2010).

128. Ramaswamy, N. & Mukerjee, S. Alkaline Anion-Exchange Membrane Fuel Cells: Challenges in Electrocatalysis and Interfacial Charge Transfer.

129. Yao, Y. *et al.* One-Pot Synthesis of PtNi Alloy Nanoparticle-Supported Multiwalled Carbon Nanotubes in an Ionic Liquid Using a Staircase Heating Process. *ACS Omega* 5, 25687–25694 (2020).
130. Koh, S. & Strasser, P. Electrocatalysis on bimetallic surfaces: Modifying catalytic reactivity for oxygen reduction by voltammetric surface dealloying. *J. Am. Chem. Soc.* 129, 12624–12625 (2007).
131. Yu, P., Pemberton, M. & Plasse, P. PtCo/C cathode catalyst for improved durability in PEMFCs. *J. Power Sources* 144, 11–20 (2005).
132. Antolini, E., Cardellini, F., Giorgi, L., & Passalacqua, E. (2000). Effect of Me (Pt + Ru) content in Me/C catalysts on PtRu alloy formation: An XRD analysis. *Journal of Materials Science Letters*, *19*(23), 2099–2103.
133. Anastasijevic, N. A., Dimitrijevic, Z. M., & Adzic, R. R. (1986). Oxygen Reduction on A Ruthenium Electrode In Alkaline Electrolytes. *J. Electroanal. Chem,* , 351–364.
134. Ohyama, J., Sato, T., Yamamoto, Y., Arai, S., & Satsuma, A. (2013). Size specifically high activity of ru nanoparticles for hydrogen oxidation reaction in alkaline electrolyte. *Journal of the American Chemical Society*, *135*(21), 8016–8021.
135. Li, M., Duanmu, K., Wan, C., & et al. (2019). Single-atom tailoring of platinum nanocatalysts for high performance multifunctional electrocatalysis. *Nature Catalysis, 2(6)*.

136. Wang, C., Daimon, H., Onodera, T., Koda, T. & Sun, S. A General Approach to the Size- and Shape-Controlled Synthesis of Platinum Nanoparticles and Their Catalytic Reduction of Oxygen. *Angew. Chemie Int. Ed.* 47, 3588–3591 (2008).

137. Wang, D., Xie, T. & Li, Y. Nanocrystals: Solution-based synthesis and applications as nanocatalysts. *Nano Res.* 2, 30–46 (2009).

138. Wilson, M. S. & Gottesfeld, S. *High Performance Catalyzed Membranes of Ultra-low Pt Loadings for Polymer Electrolyte Fuel Cells*. *J. Electrochem. Soc* vol. 139 (1992).

139. Pantea, D., Darmstadt, H., Kaliaguine, S. & Roy, C. Electrical conductivity of conductive carbon blacks: Influence of surface chemistry and topology. *Appl. Surf. Sci.* 217, 181–193 (2003).

140. Lázaro, M. J. *et al. STUDY AND APPLICATION OF CARBON BLACK VULCAN XC-72R IN POLYMERIC ELECTROLYTE FUEL CELLS*. (2014).

141. Meng, C. *et al.* Insight into the Role of Surface Wettability in Electrocatalytic Hydrogen Evolution Reactions Using Light-Sensitive Nanotubular TiO 2 Supported Pt Electrodes. *Sci. Rep.* 7, 1–8 (2017).

142. Sakuma, G., Fukunaka, Y. & Matsushima, H. Nucleation and growth of electrolytic gas bubbles under microgravity. *Int. J. Hydrogen Energy* 39, 7638–7645 (2014).

143. Holme, T., Zhou, Y., Pasquarelli, R. & O'hayre, R. First principles study of doped carbon supports for enhanced platinum catalysts. Phys. Chem. Chem. Phys., ,12, 9461-9468 (2010)

144. Sun, C. L. *et al.* Atomistic nucleation sites of Pt nanoparticles on N-doped carbon nanotubes. *Nanoscale* 5, 6812–6818 (2013).

145. 1. Cheng, X., Wei, G., Wang, C., Shen, S. & Zhang, J. Experimental probing of effects of carbon support on bulk and local oxygen transport resistance in ultra-low Pt PEMFCs. *Int. J. Heat Mass Transf.* 164, (2021).

146. 1. Li, Y., Zhang, X., Wang, S. & Sun, G. Durable Platinum-Based Electrocatalyst Supported by Multiwall Carbon Nanotubes Modified with CeO2. *ChemElectroChem* 5, 2442–2448 (2018).

147. Padgett, ELLIOT, E. A. Mitigation of PEM Fuel Cell Catalyst Degradation with Porous Carbon Supports. *J. Electrochem. Soc.* 116, 198–207 (2019).

148. Qin, W., Lu, S., Wang, Z. & Wu, X. Edge-functionalized acetylene black anchoring sulfur for high-performance Li–S batteries. *J. Energy Chem.* 26, 448–453 (2017).

149. CheapTubes.com. *Grade 4 GNPs Technicl Data Sheet*. (2021).

150. Kim, J. H., Cheon, J. Y., Shin, T. J., Park, J. Y. & Joo, S. H. Effect of surface oxygen functionalization of carbon support on the activity and durability of Pt/C catalysts for the oxygen reduction reaction. *Carbon N. Y.* 101, 449–457 (2016).

151. Shao, M., Odell, J. H., Choi, S. Il & Xia, Y. Electrochemical surface area measurements of platinum- and palladium-based nanoparticles. *Electrochem. commun.* 31, 46–48 (2013).
152. Sokirko, A. V. & Bark, F. H. Diffusion-migration transport in a system with butler-volmer kinetics, an exact solution. *Electrochim. Acta* 40, 1983–1996 (1995).
153. Bard, A. & Faulkner, L. *Electrochemical Methods: Fundamentals and Applications - Allen J. Bard, Larry R. Faulkner - Google Books*. (2000).
154. Dubouis, N. & Grimaud, A. The hydrogen evolution reaction: From material to interfacial descriptors. *Chem. Sci.* 10, 9165–9181 (2019).
155. Turner, J. A. Sustainable hydrogen production. *Science* vol. 305 972–974 (2004).
156. Holladay, J. D., Hu, J., King, D. L. & Wang, Y. An overview of hydrogen production technologies. *Catalysis Today* vol. 139 244–260 (2009).
157. Glaister, B. J. & Mudd, G. M. The environmental costs of platinum-PGM mining and sustainability: Is the glass half-full or half-empty? *Miner. Eng.* 23, 438–450 (2010).
158. Osgood, H., Devaguptapu, S. V., Xu, H., Cho, J. & Wu, G. Transition metal (Fe, Co, Ni, and Mn) oxides for oxygen reduction and evolution bifunctional catalysts in alkaline media. *Nano Today* vol. 11 601–625 (2016).

159. Mahmood, N. *et al.* Electrocatalysts for Hydrogen Evolution in Alkaline Electrolytes: Mechanisms, Challenges, and Prospective Solutions. *Adv. Sci.* 5, 1700464 (2018).

160. REDMAN, M. J. & STEWARD, E. G. Cobaltous Oxide with the Zinc Blende/ Wurtzite-type Crystal Structure. *Nature* 867 (1962).

161. Golosovsky, I. V *et al.* Zinc blende and wurtzite CoO polymorph nanoparticles: rational synthesis and commensurate and incommensurate magnetic order.

162. Grimes, R. W. & Lagerlof, K. P. D. Polymorphs of Cobalt Oxide. *J. Am. Ceram. Soc.* 74, 270–273 (1991).

163. DiCarlo, J. & Navrotsky, A. Energetics of Cobalt(II) Oxide with the Zinc-Blende Structure. *J. Am. Ceram. Soc.* 76, 2465–2467 (1993).

164. Chen, Y., Peng, D. L., Lin, D. & Luo, X. Preparation and magnetic properties of nickel nanoparticles via the thermal decomposition of nickel organometallic precursor in alkylamines. *Nanotechnology* 18, (2007).

165. Beverskog, B. & Puigdomenech, I. Revised Pourbaix diagrams for nickel at 25-300°c. *Corros. Sci.* 39, 969–980 (1997).

166. Chivot, J., Mendoza, L., Mansour, C., Pauporté, T. & Cassir, M. New insight in the behaviour of Co-H2O system at 25-150 °C, based on revised Pourbaix diagrams. *Corros. Sci.* 50, 62–69 (2008).

167. Shao, Q. *et al.* Stabilizing and Activating Metastable Nickel Nanocrystals for Highly Efficient Hydrogen Evolution Electrocatalysis Article. *ACS Nano* 12, (2018).

168. Anandan, K. & Rajendran, V. Morphological and size effects of NiO nanoparticles via solvothermal process and their optical properties. *Mater. Sci. Semicond. Process.* 14, 43–47 (2011).

169. Beach, E. R., Shqau, K., Brown, S. E., Rozeveld, S. J. & Morris, P. A. Solvothermal synthesis of crystalline nickel oxide nanoparticles. *Mater. Chem. Phys.* 115, 371–377 (2009).

170. Anandan, K. & Rajendran, V. Morphological and size effects of NiO nanoparticles via solvothermal process and their optical properties. *Mater. Sci. Semicond. Process.* 14, 43–47 (2011).

171. Wang, X. *et al.* Electrochemical properties of NiCoO 2 synthesized by hydrothermal method. (2017) doi:10.1039/c7ra10232a.

172. Ashok, A., Kumar, A., Ponraj, J., Mansour, S. A. & Tarlochan, F. Single Step Synthesis of Porous NiCoO 2 for Effective Electrooxidation of Glycerol in Alkaline Medium . *J. Electrochem. Soc.* 165, J3301–J3309 (2018).

173. He, X. *et al.* Phase-and Size-Dependent Optical and Magnetic Properties of CoO Nanoparticles. (2015)

APPENDIX

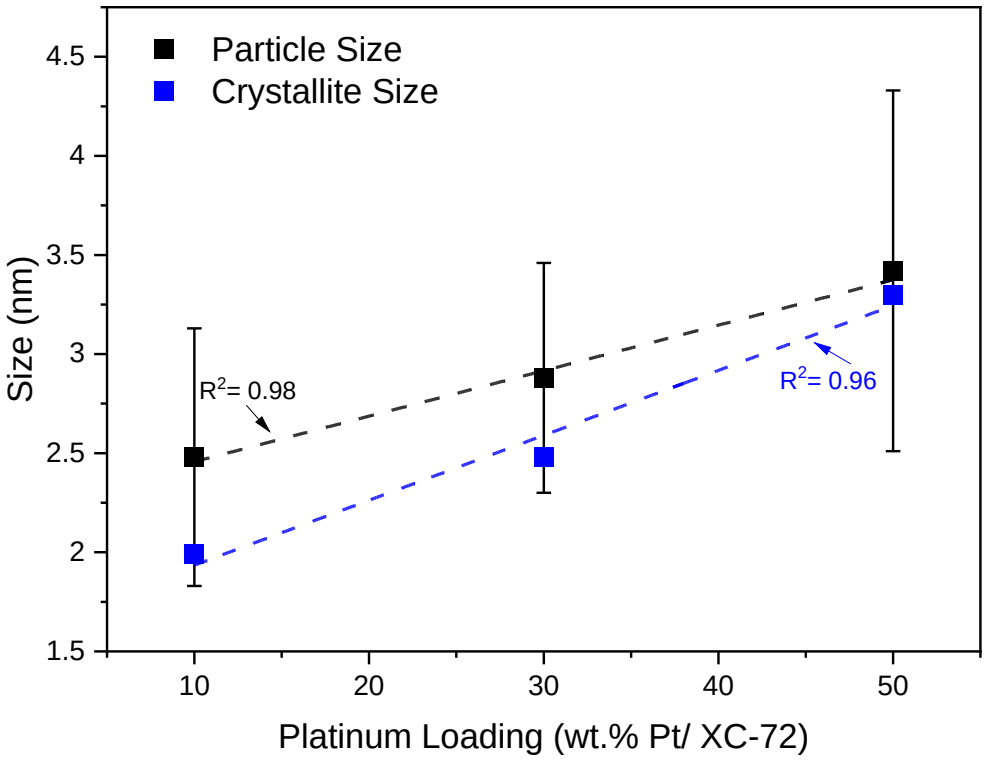

Figure A2.1: Scatter plot depicting the relationship of particle size, measured through manual diameter measurements of +100 particles via ImageJ, and crystallite size, measured through Scherrer analysis as a function of expected platinum loading. Average linear fit correlation (R^2 = 0.97).

Table A3.1: Quantitative analysis of Williamson-Hall plots for samples prepared using a modified CVD method at various temperatures and pressures. The crystallite size and microstrain were calculated from the y-intercept and slope of Williamson-Hall plots, respectively.

Sample Name	Initial Pressure (kPa)	Final Pressure (kPa)	Final Temperature (°C)	Crystallite Size (nm)	Relative Strain (unitless)
Low T and P	18.24	83.55	185	1.858	-0.00625
185 MP	28.37	65.77	185	1.931	-0.00652
185 HP	38.5	50.53	185	2.366	0.0017
200 LP	18.24	84.39	200	1.991	-0.00541
200 MP	28.37	65.77	200	2.149	-0.00324
200 HP	38.5	53.92	200	2.214	-0.00202
210 LP	18.24	86.63	210	2.057	-0.00334
Mid T and P	28.37	74.23	210	2.314	-9.51E-05
210 HP	38.5	51.55	210	1.995	-0.00677
220 LP	18.24	88.63	220	2.098	-0.00274
220 MP	28.37	75.93	220	1.956	-0.00706
220 HP	38.5	54.76	220	2.501	0.00157
235 LP	18.24	100.48	235	1.913	-0.00749
235 MP	28.37	74.23	235	1.914	-0.00865
High T and P	38.5	55.61	235	1.855	-0.01271

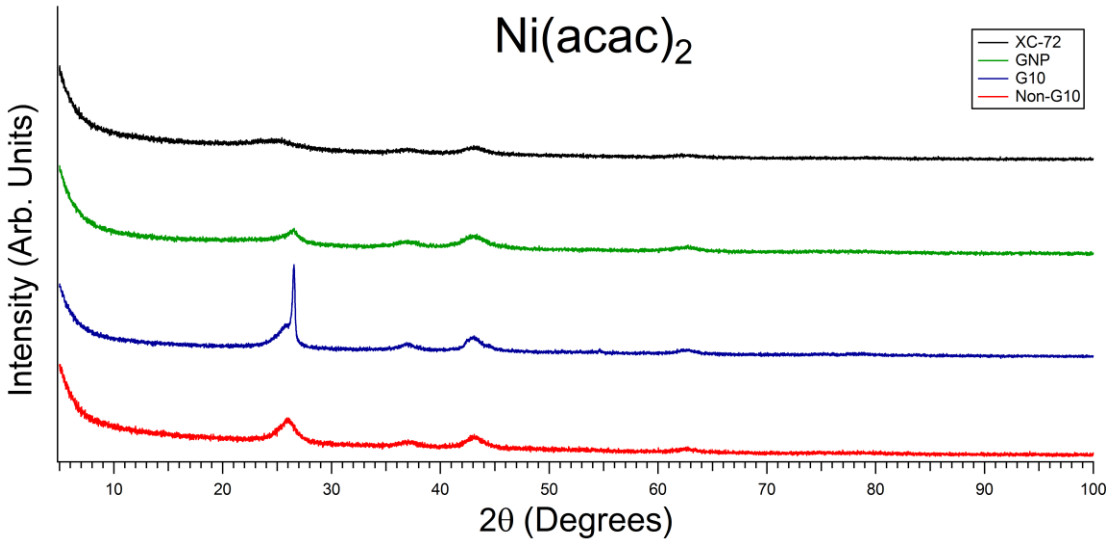

Figure A4.1: Cu K_α X-ray diffraction patterns of NiO nanoparticles deposited on various carbon supports synthesized through the modified CVD method utilizing $Ni(acac)_2$ as the organometallic precursor. Peaks at ~25 o2θ are formed by the C (200) facet. Additional peaks at 37.3 (111) and 43.2 (200) ^{o}2θ correspond to the NiO phase.

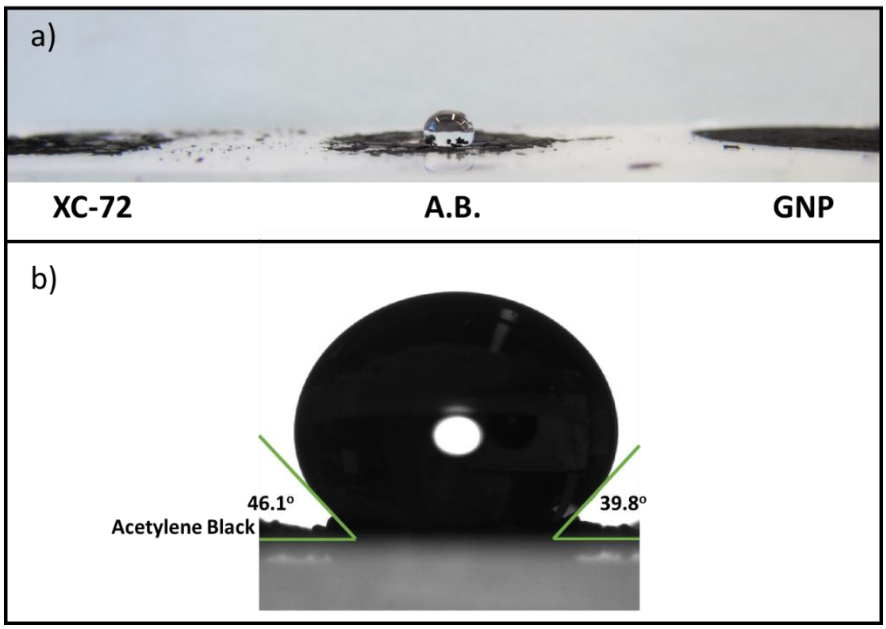

Figure A5.1: Contact angle measurements of XC-72, Acetylene Black, and Graphitized nanoplatelets. The XC-72 and GNP carbons adsorbed the aliquot of water immediately due to their hydrophilicity.

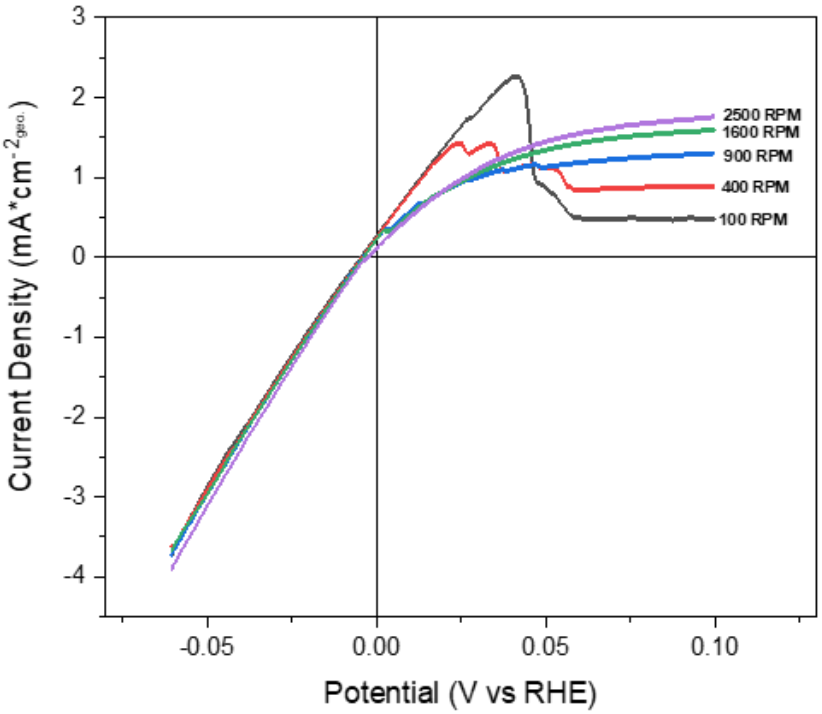

Figure A5.2: Polarization plot of 30% Pt/ A.B. in 0.1M NaOH at 2 mV/s at various rotations. The oxidative peak found around 0.025 V vs. RHE indicates the formation of a hydrogen bubble that is removed through higher rotation rates. The increased currents found in this region are due to higher concentrations of H_2 near the surface of the electrode due to the inability to remove the gas bubble at slower rotations.

VITA

Stefan T. D. Williams was born in Ft Benning, Ga. His academic journey began in 2015 when he earned his Bachelor of Science Degree in Physics from Morehouse College in Atlanta, Ga. Upon graduation, Stefan received his commission as an Infantry Officer in the U.S. Army National Guard. Concurrently, he began his research career at Los Alamos National Laboratory (LANL) in Los Alamos, NM as an intern in May of 2015, then a post-bachelor student in early 2016. His initial work focused on hydrogen fuel quality, cerium migration in PEMFCs, and fuel cell performance and durability. In 2017, Stefan was admitted into the African American Partnership Program, reviving a Director's Fellowship at LANL, and began his graduate education in the Chemical and Biomolecular Engineering Department at The University of Tennessee, Knoxville (UTK). He was advised by Governors Chair Professor Dr. Thomas A. Zawodzinski Jr. at UTK and Mr. Tommy Q. T. Rockward at LANL.